

# Damage Mechanisms in Shock Wave Lithotripsy (SWL)

Thesis by

Murtuza Lokhandwalla

In Partial Fulfillment of the Requirements  
for the Degree of  
Doctor of Philosophy



California Institute of Technology  
Pasadena, California

2001

(Submitted February 2, 2001)



© 2001

Murtuza Lokhandwalla

All Rights Reserved

# Acknowledgments

I thank my advisor, the late Prof. Bradford Sturtevant, for his invaluable guidance. It is a pity that he is no longer with us today. He was genuinely concerned with both my academic career and my personal well-being. Brad shared my excitement in all the problems we worked on and coupled with this was his in-depth knowledge in diverse fields. I sorely miss the opportunity of being able to discuss my ideas with him. He has left an indelible impression on me and probably many other students and colleagues. I dedicate my thesis to my late advisor.

I would like to take this opportunity to thank Caltech faculty members, including Profs. G Ravichandran, Hans Hornung, Tim Colonius and Joe Shepherd for their constant support and valuable comments on my work. Also, many thanks to the GALCIT staff, especially the Aeroshop staff (Joe, Larry and Ali), for their direct contribution to my work. My collaboration with the PPG investigators, particularly Profs. Jim Williams, Jim McAteer, Robin Cleveland and Mike Bailey, afforded me a unique learning opportunity. Their suggestions have played an important role in determining the course taken by this dissertation, and I acknowledge their contributions to this work.

On a personal level I would like to thank all my friends at Caltech who have helped me in my work, and made my stay here pleasant and enjoyable. I am indebted to my family members: my parents, Yusuf and Fatema, my brother, Mustufa, and my wife, Arwa, who have always supported me in my good and bad times, and motivated me to take up this venture.

This research was sponsored by National Institutes of Health (NIH) Grant P01 DK43881.

# Abstract

Shock wave lithotripsy is a ‘non-invasive’ therapy for treating kidney stones. Focused shock waves fragment stones to a size that can be passed naturally. There is, however, considerable tissue injury associated with this treatment, and the mechanisms of stone fragmentation and tissue injury are not well understood. This work investigates potential tissue damage mechanisms, with an aim towards modifying the wave-field parameters, so as to enhance stone fragmentation and minimize tissue damage.

Lysis of red blood cells (RBC’s) due to *in vitro* exposure to shock waves was considered as a model of cellular level damage. Fluid flow-fields induced by a non-uniform shock wave, as well as radial expansion/implosion of a bubble was hypothesized to cause lysis of cells. Both the above flow-fields constitute an *unsteady*, extensional flow exerting inertial as well as viscous forces on the RBC membrane. The resultant membrane tension and the membrane areal strain ( $\Delta A/A$ ) due to the above flow-fields were estimated. Both were found to exert a significantly higher inertial force (50 – 100 mN/m) than the critical membrane tension (10 mN/m). Bubble-induced flow-field was estimated to last for a longer duration ( $\sim 1 \mu\text{s}$ ) compared to the shock-induced flow ( $\sim 1 \text{ ns}$ ) and hence, was predicted to be lytically more effective, in typical *in vitro* experimental conditions. However, *in vivo* conditions severely constrain bubble growth, and cell lysis due to shock-induced shear could be dominant.

Hemolysis due to shock-induced shear, in absence of cavitation, was experimentally investigated. The lithotripter-generated shock wave was refocused by a parabolic reflector. This refocused wave-field had a tighter focus (smaller beam-width and a higher amplitude) than the lithotripter wave-field. Cavitation was eliminated by applying overpressure to the fluid. A novel passive cavitation detector (HP-PCD) operating at high overpressure (upto 7 MPa) was used to measure acoustic emission due to bubble activity. Aluminum foils were also used to differentiate cavitation from non-cavitation mode of damage. RBC’s suspended in phosphate-buffered saline

(PBS) were exposed to the reflected wave-field from the parabolic reflector and also from a flat reflector, the latter serving as a control experiment. Exposure to the wave-field from the parabolic reflector increased hemolysis four-fold compared to untreated controls and was twice that of cell lysis with the flat reflector. This result corroborated the hypothesis of shock-induced shear as a cell damage mechanism in the absence of cavitation.

# Contents

<b>Acknowledgments</b>	<b>iv</b>
<b>Abstract</b>	<b>v</b>
<b>1 Introduction</b>	<b>1</b>
1.1 Overview . . . . .	1
1.2 Tissue damage mechanisms . . . . .	2
1.3 Experiments . . . . .	4
1.3.1 Experimental lithotripter . . . . .	4
1.3.2 Parabolic reflector and HP-PCD . . . . .	6
1.3.3 Foil damage and cell lysis . . . . .	7
1.4 Analysis . . . . .	8
1.4.1 RBC deformation in a fluid-flow field . . . . .	8
1.4.2 Stone fragmentation . . . . .	8
<b>2 Experimental setup</b>	<b>9</b>
2.1 Experimental lithotripter . . . . .	9
2.1.1 High voltage supply and control circuit . . . . .	9
2.1.2 Hemi-ellipsoidal reflector and test tank . . . . .	14
2.1.3 Water degassing and storage system . . . . .	15
2.1.4 Auxiliary systems . . . . .	17
2.2 Refocused wave-field . . . . .	17
2.3 High pressure passive cavitation detection (HP-PCD)system . . . . .	20
2.3.1 PCD . . . . .	20
2.3.2 Pressure chamber . . . . .	24
2.4 Foil exposure . . . . .	29

2.5	Cell lysis . . . . .	29
<b>3</b>	<b>Experimental results</b>	<b>31</b>
3.1	Lithotripter characteristics . . . . .	31
3.1.1	Lithotripter acoustic field . . . . .	31
3.1.2	Electrical parameters . . . . .	32
3.1.3	Effect of pulse repetition frequency . . . . .	34
3.2	Refocused wavefield . . . . .	36
3.3	Bubble emission measurements . . . . .	40
3.3.1	Free-field emission . . . . .	40
3.3.2	Closed-field emission . . . . .	46
3.4	Foil damage data . . . . .	47
3.5	Cell lysis results . . . . .	50
<b>4</b>	<b>Analysis of cell deformation</b>	<b>52</b>
4.1	Kinematic decomposition of fluid flow-field . . . . .	52
4.2	Cell deformation . . . . .	54
4.3	Membrane properties . . . . .	56
4.4	Inertial forces . . . . .	61
4.5	Viscous forces . . . . .	64
4.6	Transition from $T_{iner}$ to $T_{visc}$ . . . . .	67
4.7	Application . . . . .	70
4.7.1	Shock-induced flow . . . . .	70
4.7.2	Bubble-induced flow . . . . .	75
<b>5</b>	<b>Discussion and conclusions</b>	<b>80</b>
5.1	Analysis . . . . .	80
5.2	Experiments . . . . .	86
5.2.1	Cell lysis . . . . .	86
5.2.2	Cavitation detection and suppression . . . . .	87
5.2.3	Foil damage . . . . .	87



5.3	General . . . . .	88
5.3.1	Optimized wave-field . . . . .	88
5.3.2	Lysis modes . . . . .	90
5.3.3	Summary . . . . .	91
<b>A</b>	<b>List of symbols</b>	<b>93</b>
<b>B</b>	<b>Decomposition of radial flow-field</b>	<b>95</b>
<b>C</b>	<b>Stokes' I<sup>st</sup> problem</b>	<b>98</b>
<b>D</b>	<b>Membrane force balance</b>	<b>101</b>
	<b>Bibliography</b>	<b>103</b>

# Chapter 1 Introduction

## 1.1 Overview

ESWL is a non-invasive method of treating kidney stones. Several thousand focused shock waves are administered to the patient, causing the stone to fragment and subsequently be voided through urine. This treatment has been considered highly effective and favored over surgery by clinicians [38, 62] and patients in a majority of cases. In this treatment, a focused shock wave propagates through about 2 inches of tissue material, before impacting the stone. Besides renal calculi, shock waves have been employed for fragmenting gallstones [60], bile duct stones [32] and even salivary gland stones [76]. Apart from crushing stones, shock waves have also shown promise for certain orthopedic pathologies, such as non-unions, or pseudarthroses [61]. Treatment of tumors by focused waves is also being investigated (Coleman's review paper [15]). Though the primary focus of this work is ESWL, the results of this work are sufficiently general to be applied to other instances of shock wave interaction with a biological medium.

The lithotripter acoustic field is distinct from that used by diagnostic ultrasound devices. A typical lithotripter pulse has a peak positive amplitude of 40 – 100 MPa, is 5  $\mu$ s long, and such transient pulses are clinically delivered at a rate of 1 Hz. On the other hand, diagnostic ultrasound employs continuous waves (CW) (or short bursts of pulses) of center frequencies 5 – 10 MHz and are of low intensity ( $< 0.1$  MPa). For maximizing the therapeutic effect, the lithotripter pulse is focused by a reflector (or a lens) into a tiny cylindrical region, which is usually 1 cm in diameter and a few cm long. Needless to say, the tissue effects of diagnostic ultrasound and the lithotripter pulse are very different. Ultrasound beams of higher pressure intensities have also been used for therapeutic purposes. High intensity focused ultrasound (HIFU) utilizes short exposures (a few seconds to milliseconds) of CW, of about 1 MHz frequency

and focuses these beams to focal regions a few millimeters wide [67]. The therapeutic effect of HIFU has been attributed to thermal effects [28]. However, temperature rise associated with the lithotripter pressure pulse is negligibly small [65], and hence the primary effects of ESWL pulse on all biological media are of a mechanical nature.

Biological effects due to the interaction of a high amplitude lithotripter pulse with tissue have been reported in the literature. A description of these effects and the causative physical properties of the acoustic field is given in a review paper [15]. Studies on animal models have shown that tissue damage in ESWL ranges from damage at cellular level to full thickness tearing of macro-level anatomical structures like arteries and veins [22, 33]. Experiments implicate two distinct mechanisms: a direct shock-induced effect, and an indirect effect due to acoustically-induced bubble activity. Currently there is no agreement amongst the lithotripsy research community as regards the validity and scope of these mechanisms. Figure 1.1 summarizes tissue damage mechanisms, which could potentially exist in an *in vivo* environment.

## 1.2 Tissue damage mechanisms

Cavitation induced by the lithotripter-generated pressure field is considered to be one of the causes for both tissue damage and stone fragmentation. Negative pressure in the trailing part of the lithotripter pulse causes bubbles to grow at nucleation sites. These bubbles eventually collapse. Bubble collapse adjacent to a solid surface is asymmetric, typically leading to a small jet of liquid impinging on the solid surface. These micro-jets are considered to be responsible for stone fragmentation and tissue damage. Several investigators have shown a reduction in lysis of RBC's (e.g., [18, 64]) when they are exposed to lithotripter shock wave under elevated ambient pressures that suppress cavitation. Also stone fragmentation is considerably enhanced in a cavitating medium [18]. Micro-jets from asymmetrical bubble collapse sets up a locally compressive stress field, followed by a tensile stress, propagating spherically into the stone interior.

Most work has focused on cavitation-induced damage, since in an *in vitro* en-

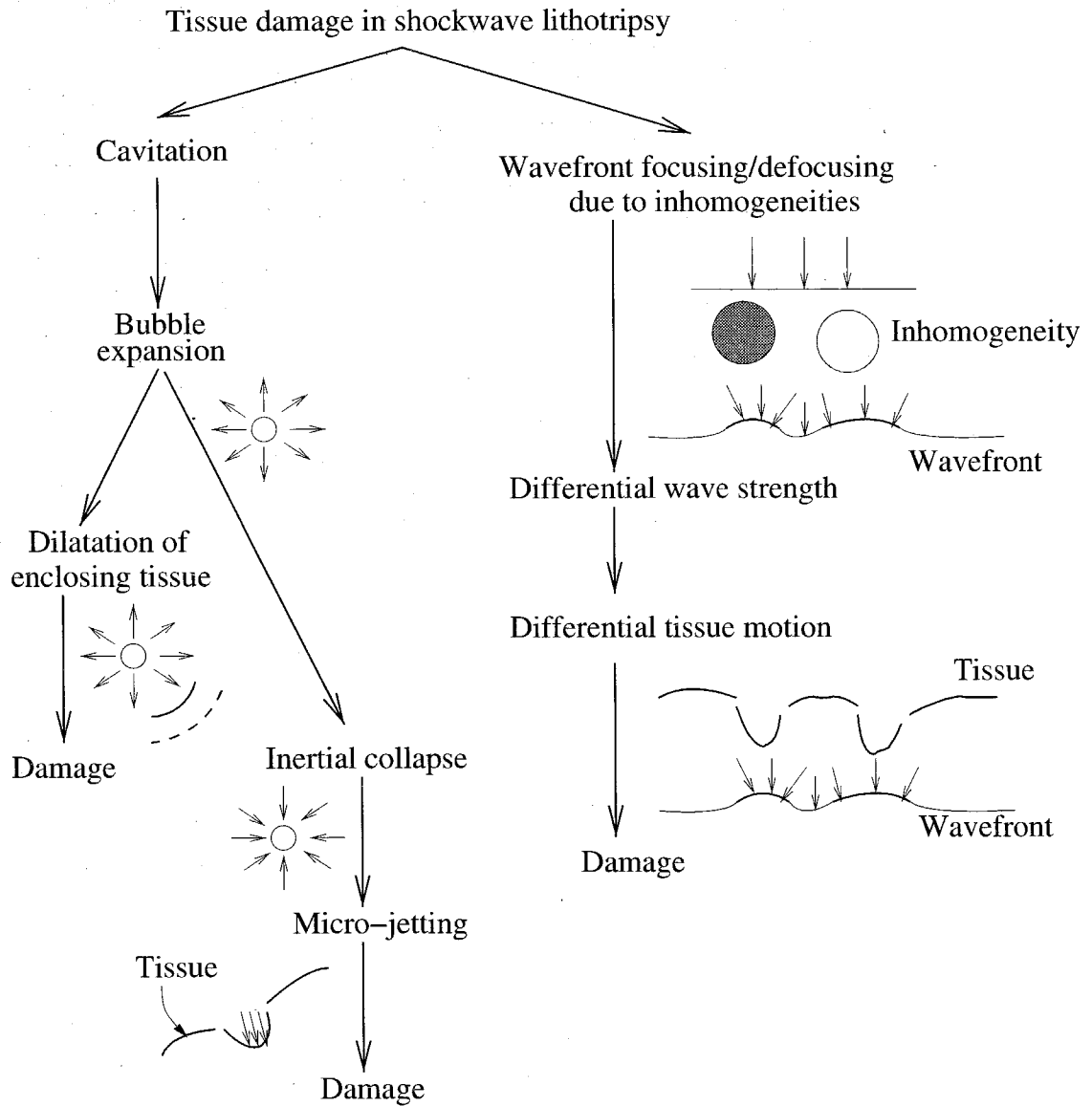


Figure 1.1: Tissue damage mechanisms.

vironment this mode of damage is overwhelming. However, the constraint of the surrounding tissue, in an *in vivo* environment, will limit bubble growth [78] and, in turn, bubble collapse will be less violent. Micro-jet formation is commonly attributed to the presence of a rigid wall in the vicinity of the imploding cavity [6]. But soft tissue and cell membranes, on account of their mechanical properties, cannot be considered as rigid surfaces, and hence micro-jetting may not be a dominant mechanism for tissue damage. On the other hand, the radial flow-field due to an expanding/collapsing

bubble can cause tissue damage. For example, a bubble expanding in a lumen could cause the lumen to dilate and rupture, at least under certain combination of lumen size, strength, and maximum bubble size. This radial flow-field can also deform and lyse isolated cells suspended in the fluid.

An alternative explanation for tissue damage can be formulated in terms of non-uniformity of the shock. Shock waves propagating in a medium which has randomly distributed acoustic inhomogeneities will cause the shock wave to be attenuated and have an increased rise time. However, a more regular tissue structure, as present in the kidney cortex and the medulla, could result into local focusing/defocusing of the wavefront (see [65] for a discussion). A focused wave induces a differential tissue motion, or shear. There is ample evidence to demonstrate that hemolysis occurs due to fluid shearing motion. Specific experimental configurations include microstreaming motion near a single resonant bubble [57], and Couette-flow viscometers [35]. A similar shearing effect due to shock wave focusing in ESWL may also cause cell lysis provided the shearing motion is sufficiently strong. An objective of the present work is to test this hypothesis by enhancing the shearing effect in ESWL and measuring the corresponding change in cell lysis.

## 1.3 Experiments

### 1.3.1 Experimental lithotripter

An electro-hydraulic lithotripter (EHL) was used for experiments reported in this work. It was designed to mimic the performance of Dornier HM3 ESWL because of widespread use of this device in clinical service. Common to all extra-corporeal lithotripters is a source for generating a pressure pulse and a reflector/lens for focusing this pulse. In an EHL the source for this pressure pulse is an explosion generated by a spark gap located at the internal focus (F1) of a hemiellipsoidal reflector. In the case of the research lithotripter used in this study, the hemiellipsoidal reflector sits at the bottom of a water tank filled with a weak electrolyte. When triggered, storage

capacitors apply a high voltage ( $\sim 20$  kV) across the spark gap. The discharge forms a conducting plasma channel and vaporizes the electrolyte. This vapor bubble expands rapidly, generating a spherical wavefront centered at F1. A sector of this spherical wavefront is reflected by the hemiellipsoidal reflector to its external focus (F2).

Figure 1.2 shows the wavefront evolution in an EHL system. Dashed lines in figure 1.2 represent the direct wavefront generated by the explosion at F1. Bold solid lines indicate the wave reflected off the hemiellipsoidal reflector, whereas the dull solid lines represent the diffracted wavefront (see [65] for a discussion on shock wave focusing in lithotripters). A schematic of the typical pressure trace at F2, and at an earlier location along the acoustic axis, is also shown in figure 1.2. A characteristic feature of this ellipsoidal reflector system is that small changes of source geometry causes large aberrations at F2.

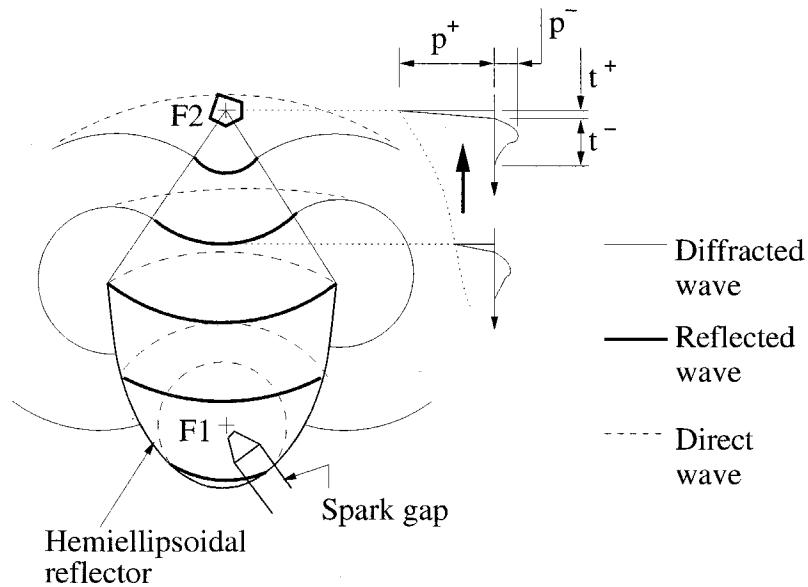


Figure 1.2: Schematic of shock wave focusing in ESWL. Sketch shows wavefront evolution and the pressure trace at two different locations along the acoustic axes.

A prototype research EHL was first constructed (described in [30]). Three replicate instruments that incorporated modifications to the prototype were then built. The prototype and the modified versions were designed by Dr. B Hartenbaum and constructed at the Graduate Aeronautical Laboratory, California Institute of Technol-

ogy, Pasadena (GALCIT). These three machines were installed at the Applied Physics Laboratory of the University of Washington, Seattle (APL-UW), the Department of Anatomy and Cell Biology, Indiana University School of Medicine, Indianapolis (Anat-IU) and at GALCIT. These three machines will be collectively referred to as the ‘Caltech lithotripters’. Design details of these research lithotripters are discussed in section 2.1. The acoustical and electrical parameters of the GALCIT lithotripter were characterized and are reported in section 3.1. (see [12] for a detailed comparison of the above lithotripters). Experiments reported in this work were performed with the GALCIT and the IU research lithotripters.

### 1.3.2 Parabolic reflector and HP-PCD

In order to test our hypothesis of shock-induced shear as a damage mechanism, an experimental setup was devised to enhance the shearing effect, monitor acoustic emission from cavitating bubbles, and suppress cavitation. The localized focusing effect of *in vivo* acoustic inhomogeneities, as discussed earlier, results in an increased wave-gradient. *In vitro*, an acoustically heterogeneous medium can also provide a similar ‘lens’ effect, e.g., a suspension of polystyrene (or a suitable polymeric material) spheres in agar. However, such a medium also attenuates the shock wave, negating the focusing effect. Also, suspending RBC’s in such a medium is a difficult task. Since a reflector can also focus a shock wave, it will have a similar ‘lens’ effect, to that of an acoustically heterogeneous medium. Such a rigid reflector has obvious advantages over a lens, i.e., it is easier to construct, and results in no attenuation of the shock. However, an obvious difference is the presence of diffracted waves from the reflector edge, which are absent in a lens wave-field. Despite this limitation, a parabolic reflector was thought to represent the best compromise between realism and practical issues of experimental design, and was used in this work.

The parabolic reflector was positioned confocally with the external focus (F2) of the hemiellipsoidal reflector of the lithotripter. Figure 2.6a shows a schematic of the reflector configuration. Section 2.2 details the reflector configuration and the acoustic

field of the refocused wave is reported in section 3.2. A similar reflector arrangement has also been reported earlier [20]. Cavitation was controlled by applying overpressure to a region surrounding F2 [64, 75]. The overpressure above which cavitation activity ceases was determined by a novel cavitation detector, which operates at high overpressure (HP-PCD). The HP-PCD monitored emission from cavitation events as overpressure was applied, until no emission was detected beyond an overpressure threshold. Bubble emission measurements in response to various wave-fields and different overpressures is reported in section 3.3.

### 1.3.3 Foil damage and cell lysis

Damage to aluminum foils has been commonly used by the lithotripsy community as a means for quantifying cavitation damage [37]. In this work aluminum foils were exposed to the lithotripter wave-field and the refocused wave-field from the parabolic reflector, at various overpressures. These experiments were designed to serve a dual purpose - to obtain an estimate of the overpressure required for eliminating cavitation damage, and also detect any deformation/damage to the targets in the absence of cavitation. The damage pattern to foils due to shock wave exposure is discussed in section 3.4 and the experimental details are reported in section 2.4.

In order to verify the shear hypothesis of cell lysis, RBC's were exposed to the wave-field reflected from a parabolic and a flat reflector. Experiments were performed under overpressures sufficient to eliminate cavitation. Cell lysis due to the flat reflector served as a control experiment for evaluating damage due to the focused wave-field from the parabolic reflector. These experiments were performed at IU. The experimental details are discussed in section 2.5 and their results are reported in section 3.5.



## 1.4 Analysis

### 1.4.1 RBC deformation in a fluid-flow field

In chapter 4 analysis of RBC deformation, subjected to a general flow-field, is presented. This general analysis is then applied to the particular case of *in vitro* exposure of RBC to ESWL shock waves. Membrane stresses and strains due to a focused shock wave and radial bubble motion are estimated. A flow-field is considered to be lytically effective if it can strain the membrane beyond a threshold strain and exert the critical tension required to induce this deformation. Since only an extensional flow causes the cells to deform, the forces exerted on the cell membrane by an extensional flow, and its consequent deformation, are estimated.

### 1.4.2 Stone fragmentation

The tensile stress induced in a stone, appearing as a result of a reflection of the compressive part of the shock at those locations in the stone that have an impedance mismatch, is known as spalling. As a part of this work, spalling failure of renal calculi was analyzed using a cohesive-zone model [49]. The details of this analytical work is reported in [40] and will be summarized here. The cohesive-zone model is essentially a constitutive law for the material accounting for the presence of microcracks. The results from this analysis relates the stone's physical properties (fracture-toughness, acoustic speed, density and void dimensions) to the shock wave parameters (peak pressure, pulse width, pulse profile, and number of shocks for fragmentation). Then, the number of shocks for spall failure are calculated using typical shock wave parameters and stone properties. A natural outcome of the analysis is that it provides us a common ground for comparing the damage inflicted on tissue and stone material, as the treatment progresses, due to various mechanisms. This analysis thus provides a theoretical framework to exploit the differential response of the tissue and stone, and modify the shock wave parameters, to minimize tissue damage and improve stone comminution.

## Chapter 2 Experimental setup

### 2.1 Experimental lithotripter

In this section the constructional details of the research lithotripter are described. Figure 2.1 shows a picture of the GALCIT research lithotripter. Various mechanical (the geometry of the ellipsoidal reflector, the angle of the acoustical axis, and the conditioning of the water) and electrical parameters (the storage capacitance, the voltage on the capacitors, the electrode, and the impedance of the discharge circuitry) were designed to match with the Dornier HM3. Other considerations driving the design were the pulse repetition rate, accuracy of positioning specimens for testing, and the simplicity and safety of operation. The apparatus consists of the following sub-systems: 1) high voltage system and control circuit; 2) hemiellipsoidal reflector and test tank; 3) water degassing and storage system; and 4) auxiliary systems.

#### 2.1.1 High voltage supply and control circuit

The essential elements of this subsystem are a power supply, a pair of capacitors, a triggering unit and an electrode. A schematic of the circuit is shown in figure 2.2, in which heavy lines designate high-voltage conductors and light lines are either control lines or are at building supply voltage (110 V). The electrical elements of the circuit are listed in table 2.1. The high-voltage power supply is capable of generating voltages in the range 0–25 kV and has an average charging rate of 500 W. The total capacitance of the power pack, C1 and C2, is 80nF. When discharged from full voltage, the capacitors can deliver up to  $0.5CV^2 = 25$  J per pulse; thus the power supply can support a maximum firing rate of 20 Hz. However, other system components limit the maximum pulse rate to 5 Hz. The voltage on the capacitors is monitored by a 10,000:1 voltage divider (R2,R3) and a digital voltmeter (M). A normally-closed

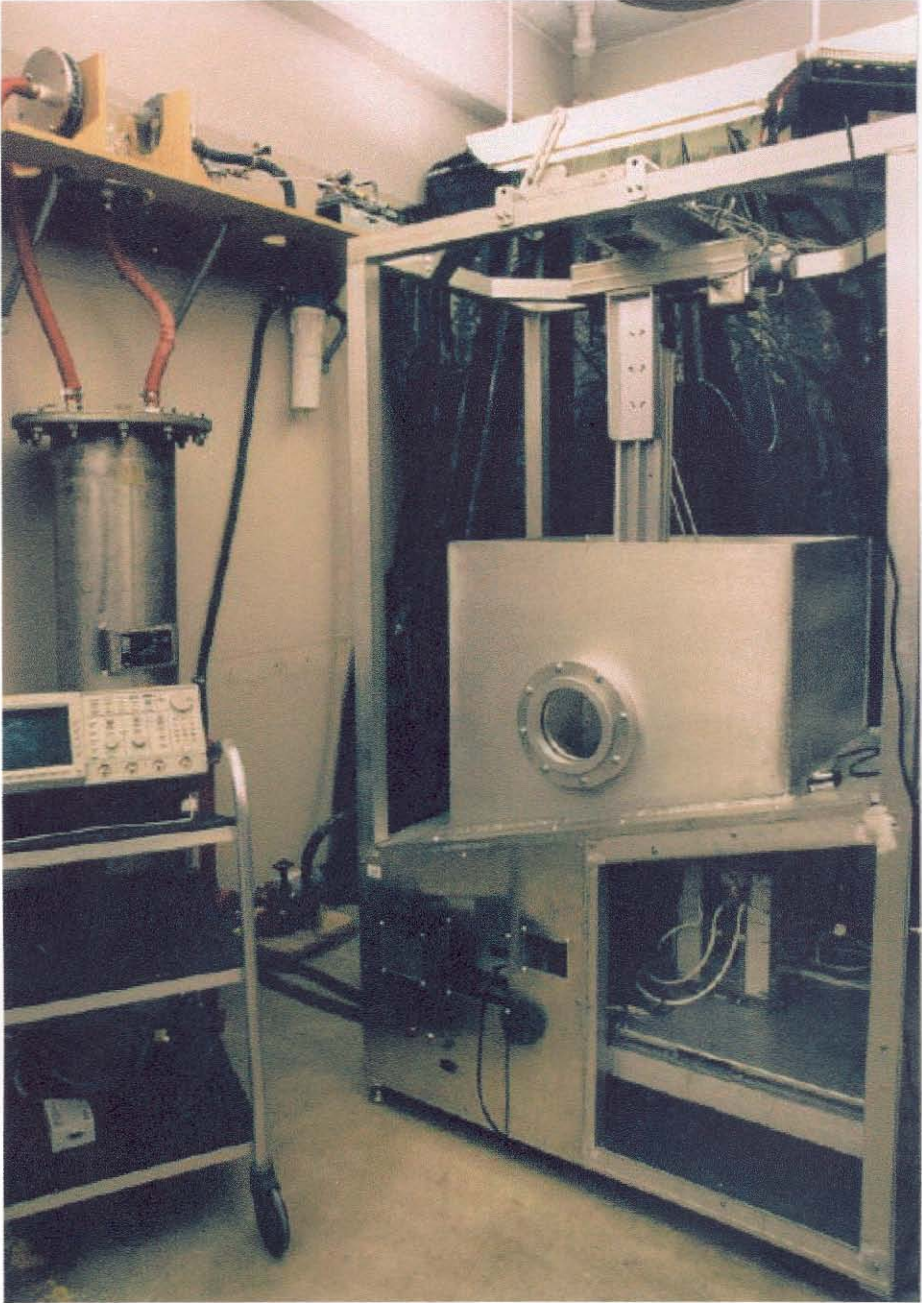


Figure 2.1: GALCIT research lithotripter.

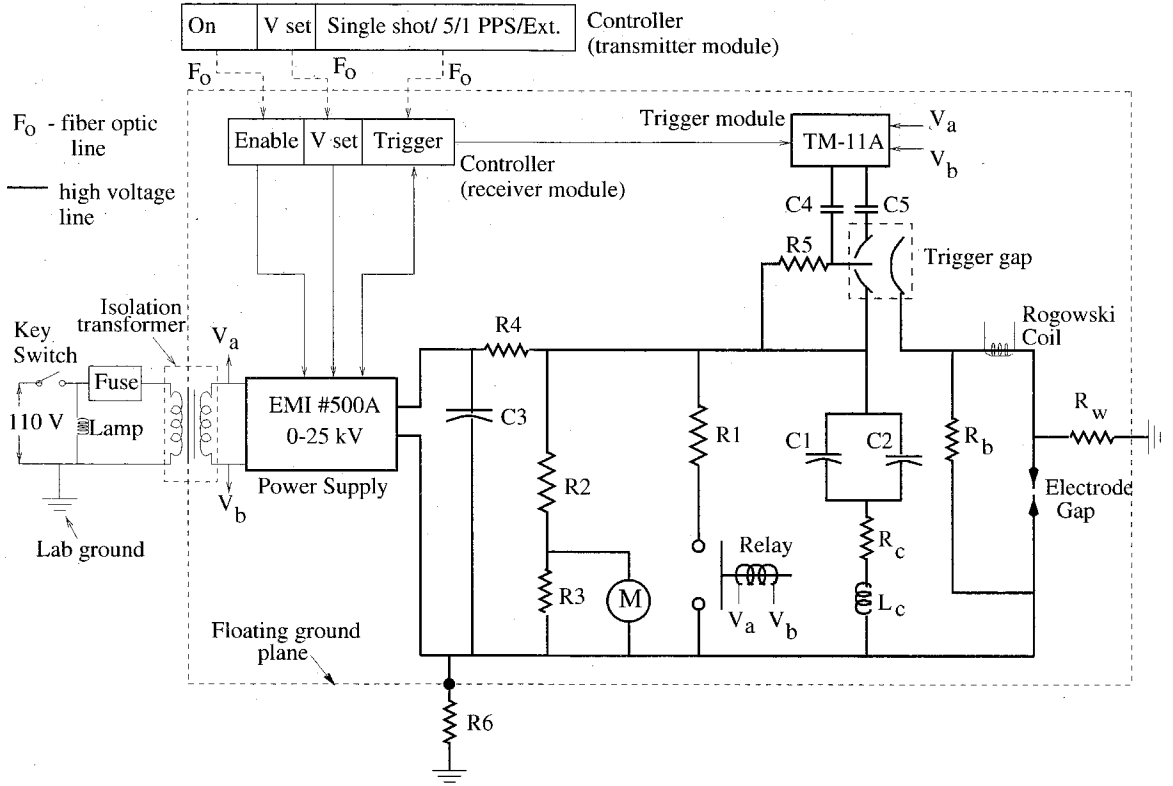


Figure 2.2: High voltage supply and control circuit. Heavy lines designate high-voltage conductors, and light lines are either control lines or are at building supply voltage (110 V).

electromagnetic relay short circuits the terminals of the storage capacitors C1, C2. This relay is activated by a key switch. Hence, in case of an accidental power failure, or when the key switch is turned off, the storage capacitors discharge through R1 in about 0.1 s. The power supply is isolated from building power by an isolation transformer. A safety feature of this design is that all the high voltage circuitry is physically built on a floating ground plane (indicated by a dotted rectangle in figure 2.2), which can be electrically isolated from laboratory ground.

The storage capacitors feed current to a triggered spark gap. The triggered spark gap acts as a rapid switch, which is closed by a trigger module. The triggered spark gap consists of a pair of primary electrodes and a third trigger electrode sealed within a housing. The trigger module applies a high-voltage pulse (15kV–30kV, rise time  $< 2 \mu\text{s}$ , recycle time  $\sim 100 \text{ ms}$ ) between the trigger electrode and one of the primary

<i>Item</i>	<i>Value</i>	<i>Vendor</i>
Resistor R1	$4 \times 0.2 \text{ M}\Omega$ , 10 kV, 1500 J	Cesiwid Inc, Niagara Falls, NY
Resistor R2	$361.4 \text{ M}\Omega$ , 30 kV, 15 W + $3.92 \text{ M}\Omega$ , 4 kV, 2 W	Caddock Electronics Inc, Riverside, CA
Resistor R3	$36.5 \text{ k}\Omega$ ( $4 \times 146 \text{ k}\Omega$ in parallel)	
Resistor R4	$2500 \text{ }\Omega$ , 45 kV	Cesiwid Inc, Niagara Falls, NY
Resistor R5	$1 \text{ M}\Omega$	
Resistor R6	$1 \text{ G}\Omega$ , 32 kV, 10 W	Cesiwid Inc, Niagara Falls, NY
Resistor R <sub>b</sub>	$7.7 \text{ k}\Omega$ ( $28 \times 275 \text{ }\Omega$ )	
Capacitor C1, C2	40 nF, 100 kV, S-type	Maxwell Laboratories, San Diego, CA
Capacitor C3	0.001 mF, 25 kVDC	Newark, Santa Fe Springs, CA
Capacitor C4, C5	500 pF, 30 kVDC	Newark, Santa Fe Springs, CA
High voltage cables	AWM 40 kVDC STYLE 3239 VW-1	Rowe, Toledo, OH
Power Supply	EMI # 500A, 0-25 kV, POS	Electronic Measurements Inc, Neptune, NJ
Trigger Module	Model TM-11A	EG&G Electro-Optics, Salem, MA
Triggered Spark Gap	Model GP-12B	EG&G Electro-Optics, Salem, MA
Isolation Transformer	IT25-5E 115 V, 25 kV	Hipotronics Inc, Brewster, NY
Fiber-optics controller	Custom designed	KVA Engineering, Hollister, CA
Electrode	Refurbished Model SG-80 (HM3 & HM4)	Servicetrends Inc, Marietta, GA
Relay	E-40-NC, 40 kV Single Pole, Normally Closed, 115 V AC coil	Ross Engineering, Campbell, CA
Grounding Rod	30 kV, 25 J, with 10 feet cable	Ross Engineering, Campbell, CA

Table 2.1: Electrical specifications of the high voltage supply and control circuit.

electrodes; the pulse ionises the gas to produce a conduction path between the primary electrodes which, in turn, carries the full discharge current from the storage capacitor. Capacitors C4 and C5 provide DC isolation, preventing a discharge from the power pack to the trigger module. The bleed resistor R<sub>b</sub> provides a bleed path for the current before the gap break-down, and results in a “softer” discharge. The resistor R<sub>c</sub> and inductance L<sub>c</sub> represent parasitic effects in the circuit. The resistor R<sub>w</sub> represents the resistance of the water bath. The Rogowski coil [50] indicated in figures 2.2 and 2.3 is a current transformer which measures the discharge current and provides a trigger for other equipment, e.g., an oscilloscope. This coil was fabricated from a coaxial cable (RG 174/U) with a micro-dot connector at one end. The other end of the cable was modified in the form of a toroid. The inner (central) conductor was bent in the form of a circular loop and the outer conductor was coiled over it (34 turns, radius of

toroid  $\approx 1$  cm). The Rogowski coil measurements are reported in section 3.1.2.

The power-pack assembly is shown in figure 2.3. The capacitors and triggered

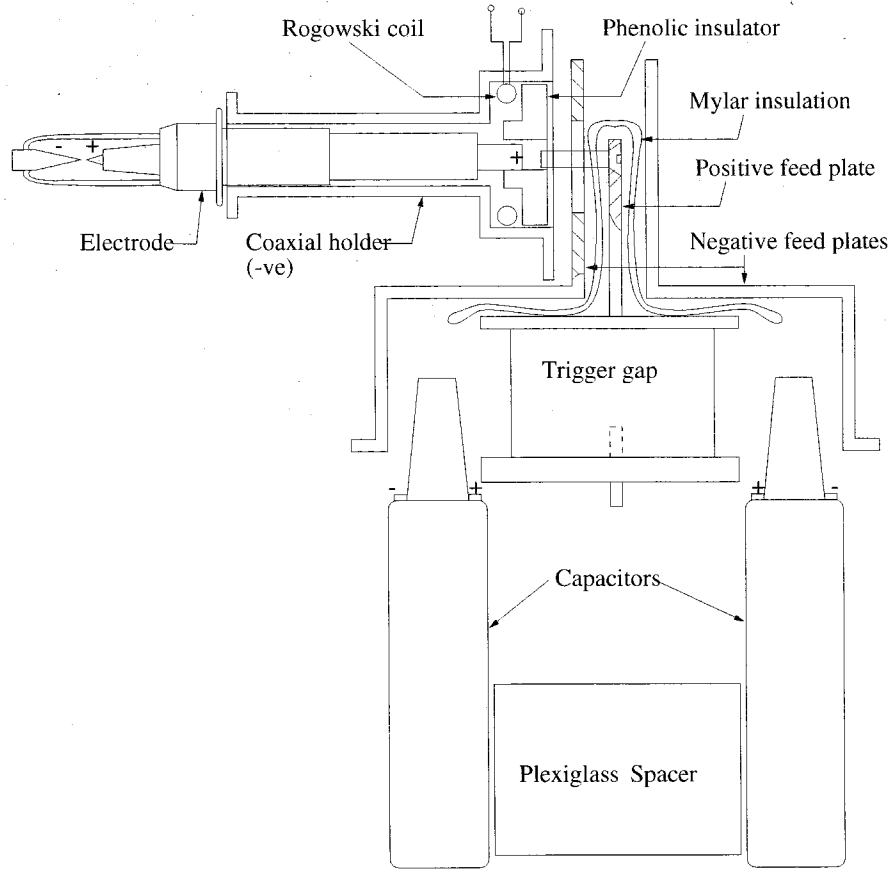


Figure 2.3: Schematic of power pack assembly.

spark gap are enclosed in an acrylic housing. The assembly above the housing converts from the planar geometry of the capacitor system to the coaxial configuration of the Dornier electrode. The hybrid planar/coaxial arrangement of the research lithotripter differs from the Dornier HM3 which is cylindrical throughout, including eight cylindrical capacitors (10 nF each) held between two circular discs (a fact we discovered after the fabrication of the research lithotripters). The arrangement of the capacitors in the research lithotripter matched the capacitance of the HM3 and had an inductance that was just slightly larger (probably induced by the planar/coaxial transition). The triggered spark gap feeds current through the copper positive feed plate to the central conductor of the coaxial holder (not shown in figure). The brass

central conductor (positive) of the coaxial holder is 14.5 mm in diameter and 35 mm long. The outer conductor (negative) has a 24 mm inner diameter and 32 mm outer diameter. The two conductors of the coaxial holder are insulated by a machined cylinder with walls 9.4 mm thick made of phenolic. The end of the coaxial holder was machined to accept the electrode, and electrical connections are made with spring-leaf contacts. Standard Dornier-type electrodes (SG-80) were used. The feedplate and coaxial holder are the principal mechanical support for the spark plug. The end of the coaxial holder is fitted with an aluminium collar so that it can be bolted to the ellipsoidal reflector. An O-ring ensures a water tight seal. The electrode is mated to the ellipsoid by sliding the powerpack into position on a horizontal shelf.

The research lithotripter system is controlled by a pair of modules (transmitter and receiver). The control features include: switching the high voltage on and off, setting the voltage level, and triggering (firing) the lithotripter. The receiver module is housed inside the lithotripter frame and is connected to the transmitter module by fiber optic cables to reduce the risk of electrical shock to the operator. The transmitter can be used to fire the lithotripter manually or in a pulse mode (1 Hz or 5 Hz). It also has an external trigger so that the lithotripter can be fired by another device, e.g., a computer or function generator.

### 2.1.2 Hemi-ellipsoidal reflector and test tank

The ellipsoidal reflector (figure 2.4) has the same dimensions as that of the unmodified Dornier HM3 lithotripter: semi-major axis  $a = 139$  mm; semi-minor axis  $b = 78$  mm ( $b/a = 0.56$ , eccentricity  $\epsilon = \sqrt{1 - (b/a)^2} = 0.8$ ); and the reflector is truncated by 15 mm, that is, it is not a complete hemiellipsoid. The aperture angle of the reflector is  $\alpha = 68^\circ$  and the direct distance between the two foci is  $2f = 2\epsilon a = 228$  mm. The electrode is located at the internal focus (F1) of the hemi-ellipsoid and is oriented at  $76^\circ$  to the major axis. The  $14^\circ$  inclination of the ellipsoid's major axis results in F2 being horizontally offset from F1, ensuring that bubbles generated near F1 do not interfere with specimens at F2. The ellipsoid is bolted to the bottom of the water

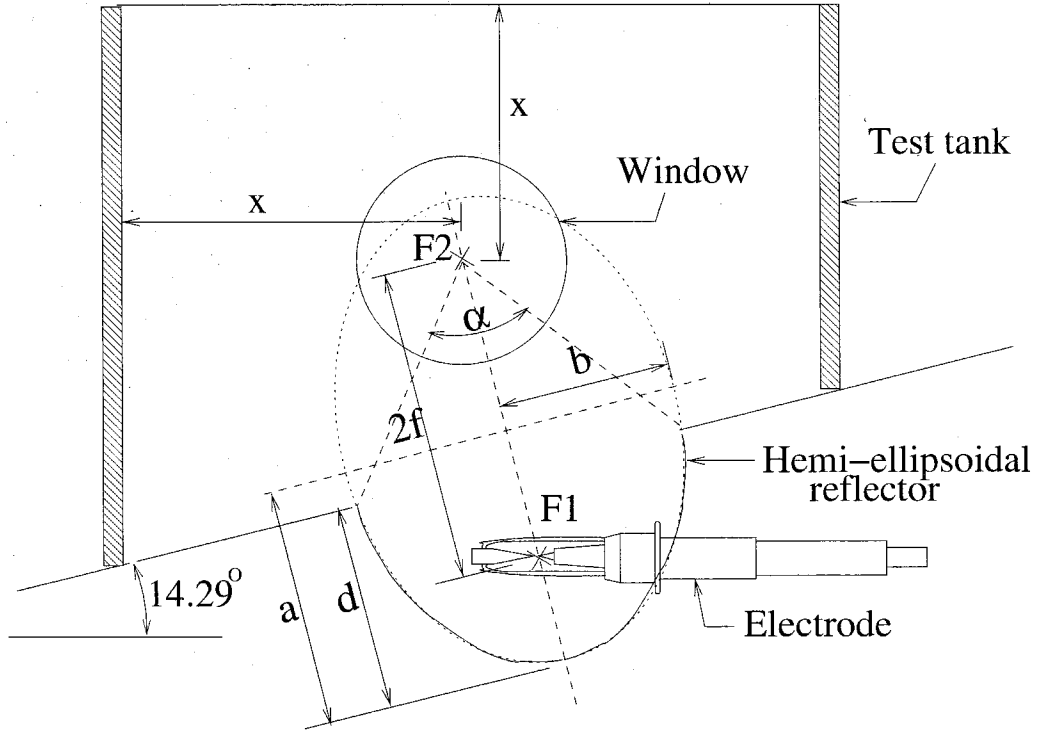


Figure 2.4: Ellipsoidal reflector geometry:  $a = 139$  mm,  $b = 78$  mm,  $d = 124$  mm,  $f = 114$  mm,  $\alpha = 68^\circ$  and  $x \approx 300$  mm.

tank and sealed with RTV silicone gel. A fixed position stylus was used to locate the geometrical focus of the ellipsoid.

The test tank is made of welded aluminum plate 13 mm thick. It has a footprint of 610×610 mm and its height varies from 460 mm to 610 mm due to the inclination of the bottom of the tank. Opposite side walls are fitted with 150 mm diameter optical quality windows centered at F2. The tank dimensions are such that path lengths ( $x$  in figure 2.4) of transmitted or scattered waves from F2 to the free surface or a wall are all approximately equal and sufficiently large that return waves do not intrude on measurements at F2 during experimental times of interest.

### 2.1.3 Water degassing and storage system

It was necessary to design a water processing system for vacuum degassing, filtering, and storing water. The motivation for degassing and filtering the water is to reduce



cavitation nuclei along the axis of the reflector, as excessive bubbles can interfere with propagation of shock waves. Figure 2.5 shows a schematic of the system; the essential

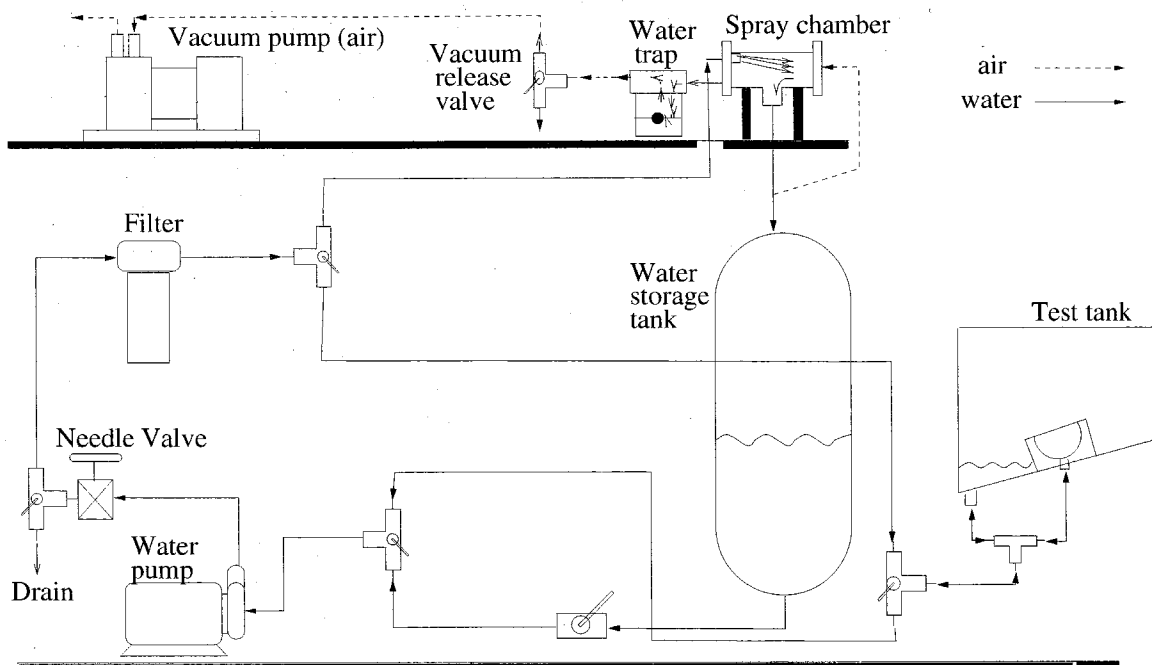


Figure 2.5: Water degassing and storage system.

components are listed in table 2.2.

<i>Item</i>	<i>Model</i>	<i>Vendor</i>
Centrifugal water pump	8249K62	McMaster-Carr, Atlanta, GA
Diaphragm vacuum pump	DAA-V174-EB	Gaast, Benton Harbor, MI
Filter housing	P-01509-00	Cole Parmer, Vernon Hills, IL
Filter cartridge	P-01509-15	
Spray chamber: 4 in $\times$ 4 in Tee	72-4487	Westchem Equipment Inc., Livermore, CA
Water trap (8 oz)	AA672K	Brenner-Fiedler, Cerritos, CA
Stainless steel tank	capacity 0.25 m <sup>3</sup>	Arrow Industries, Maywood, CA

Table 2.2: Description of components in water processing subsystem.

When the system is in degassing mode, water is pumped from the storage tank (0.25 m<sup>3</sup> capacity), passed through the filter (0.5 micron) and into the spray chamber. The spray chamber is evacuated to an absolute pressure of about 20 kPa (0.8 atm vacuum) by the vacuum pump. The water is sprayed into the chamber through a

nozzle with 20 holes each of 1-mm diameter; the spray increases the surface area of the water and thus accelerates the degassing process. The system can reduce the  $O_2$  content of the water in the storage tank to below 5 ppm within one hour. The water can be stored under vacuum to maintain low levels of dissolved gas. Transfer of the degassed water to the lithotripter tank is done at atmospheric pressure through the centrifugal pump. While sitting in the test tank the water regasses at a rate of about 1 ppm/day. The pump takes about 10 minutes to fill the test tank, and delivers 12 liters per minute against a head of 135 kPa. The water is softened by adding either NaCl or  $NaHCO_3$  until a conductivity of  $660 \mu S/cm$  is achieved. The degassing and softening of the water is very similar to the Dornier HM3 water processing system.

#### 2.1.4 Auxiliary systems

Motor driven X-Y-Z slides (Velmex-Unislide, East Bloomfield, NY) were mounted on the lithotripter console which enabled positioning of targets for shock wave exposure or positioning hydrophones for characterizing the lithotripter wave-field. The slides could be controlled by hand-held joystick or computer controlled. The controller communicated with a PC (Pentium 166 MHz) by a general purpose interface bus (GPIB / IEEE 488.2). A commercial software package (National Instruments, Austin, TX - Labview) was used to program the motion of the slides. Figure 2.12 shows a schematic of the entire set-up.

## 2.2 Refocused wave-field

As explained in the introduction (section 1.3.2) the lithotripter wave was refocused to study the effect of lateral variations in shock strength on tissue damage. A parabolic (or flat) reflector was used to obtain this effect. In this section the experimental details of this reflector configuration are described. The lithotripter-generated wave-field that is incident on the parabolic or flat reflector is called the 'lithotripter wave-field'. The term 'reflected wave-field' is used to identify the result of the reflection off the above

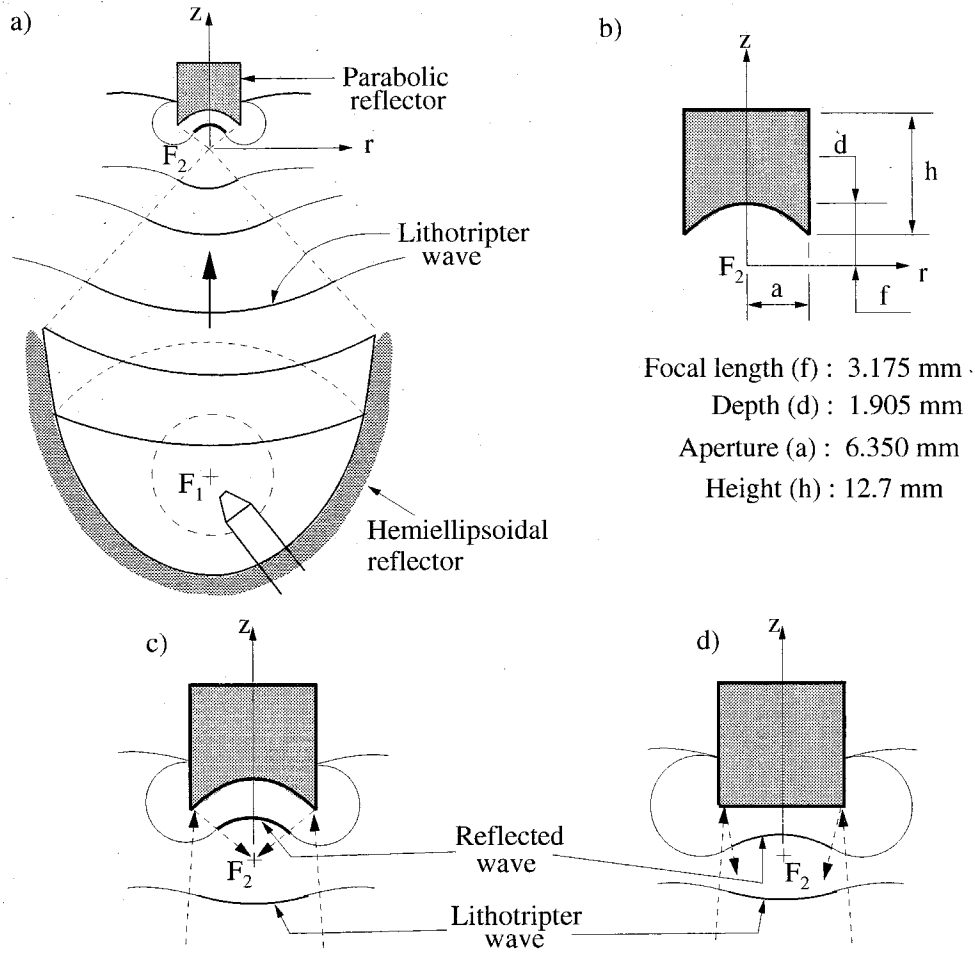


Figure 2.6: a) Reflector configuration and wavefront geometry. b) Parameters of parabolic reflectors. c), d) Reflected wave geometry off the parabolic and flat reflectors. Dotted arrows indicate rays, solid lines are wavefronts.

reflectors. The term 'refocused wave-field' will be used occasionally as a synonym for 'reflected wave-field' in reference to the refocusing effect of the parabolic reflector.

The parabolic reflector was oriented such that its focus coincided with  $F_2$ , the focal point of the hemi-ellipsoidal reflector (figure 2.6a). The reflector surface was a paraboloid of revolution, with the geometrical parameters of the parabola indicated in figure 2.6b. Dimensions were chosen so that the reflector would fit into the vials used to hold RBC's, and also to maximize the portion of the lithotripter wave that would be reflected. Since, in the vicinity of  $F_2$ , the lithotripter shock wave is nearly planar, the parabolic reflector reflected this shock wave back to the focal point of the

paraboloid and, therefore, back to F2, as indicated in figure 2.6c. The flat reflector was aligned coaxially with the symmetry axis of the hemiellipsoidal reflector with the reflecting surface 4 mm above F2. The overall dimensions of the flat reflector ( $a$  and  $h$  in figure 2.6b) were identical to those of the parabolic reflector.

The focusing effect of the parabolic reflector is applicable in the limit of geometrical acoustics, that is, incident waves of the lithotripter wave-field of wavelength ( $\lambda$ ) much smaller than a characteristic reflector dimension ( $f$  or  $a$  in figure 2.6b) will be focused. Since the lithotripter wave has a range of frequency components (shockfront is estimated to be 60 nm thick for a shock strength corresponding to 35 MPa [65], whereas overall pulse length is measured to be about 8 mm long ( $5 \mu\text{s} \times 1500 \text{ m/s}$ )), only the high frequency components ( $\lambda \ll 3 \text{ mm}$ ) get focused, whereas the remaining are merely scattered by the reflector. Similar shock-focusing reflectors have been used in gas-filled shock tubes [66] where plane shocks of various strengths were focused by parabolic reflectors. There is one important difference. In this case the shockfront decays in  $\sim 2 \mu\text{s}$  (3 mm) which is comparable to reflector dimensions, whereas the above mentioned experiments had a constant shock strength for a length scale much larger than any reflector dimension.

The pressure traces reported here were measured using a commercial polyvinylidene fluoride (PVDF) membrane hydrophone (Model 301, Sonic Industries, Hattboro, PA), which utilizes the piezoelectric effect of PVDF. The sensitive element of the hydrophone had a nominal diameter of 0.5 mm and a flat response up to 50 MHz, as quoted by the manufacturer. Other details of this hydrophone, and the supporting apparatus, have been reported elsewhere (refer [12]). All waveform measurements reported in section 3.2 were performed with a lithotripter setting of 18 kV and subsequent shots were fired at greater than 15 s interval. The lithotripter test-tank was filled with water, which had been degassed for one hour at an absolute pressure of 24 kPa. Water conductivity was maintained at  $700 \mu\text{S/cm}$ , by addition of  $\text{NaHCO}_3$ . The membrane hydrophone was immersed in deionized water (conductivity  $< 5 \mu\text{S/cm}$ ) in an acoustically transparent isolation tank.

## 2.3 High pressure passive cavitation detection (HP-PCD) system

In this section the cavitation detection system used for measuring bubble emission under conditions of altered ambient pressure is detailed. A passive cavitation detector (PCD), similar to that used by others [13, 14, 77], was used to measure acoustic emission from bubble activity in the focal region of the lithotripter. Typically, a PCD consists of a focused piezoceramic receiver designed such that it detects acoustic emissions from cavitation activity occurring in the focal region of the receiver. It is also intended that the PCD minimally affects bubble dynamics and hence the name 'passive'. An important design feature of the PCD used here is that it was coupled with a pressure chamber. Thus the fluid in the vicinity of F2 could be pressurized and the acoustic emission due to bubble activity can be simultaneously measured.

### 2.3.1 PCD

The PCD piezoceramic element was a spherical segment (i.e., bowl) 2 mm (0.08") thick, 61.5 mm (2.42") radius of curvature, and an aperture diameter of 38.2 mm. The element was made of lead zirconate titanate (Channel Industries Inc., Santa Barbara, CA - C 5400) with a silver coating on its two faces, which served as electrodes. It had a resonant frequency of 1 MHz in the thickness mode and 54 kHz in the planar/radial mode (i.e., mode in which radial dimension of the element changes). The bowl was held in a stainless-steel water-tight housing designed to sustain 7 MPa ( $\approx$  1000 psi). The element was held in place by a brass ring. The assembled configuration of the housing, the element, and the brass ring, can be seen in figure 2.7. The brass ring was separated from the housing, otherwise it would short-circuit the signal from the element. The brass ring was held in place by a cylindrical guide made of polyphenylene oxide (PPO) (McMaster Carr, Los Angeles, CA - 8561K351). Conductive O-rings (Tecknit, Cranford, NJ - 87-10512) were used between the element faces, the housing and the brass ring (not shown in figure).

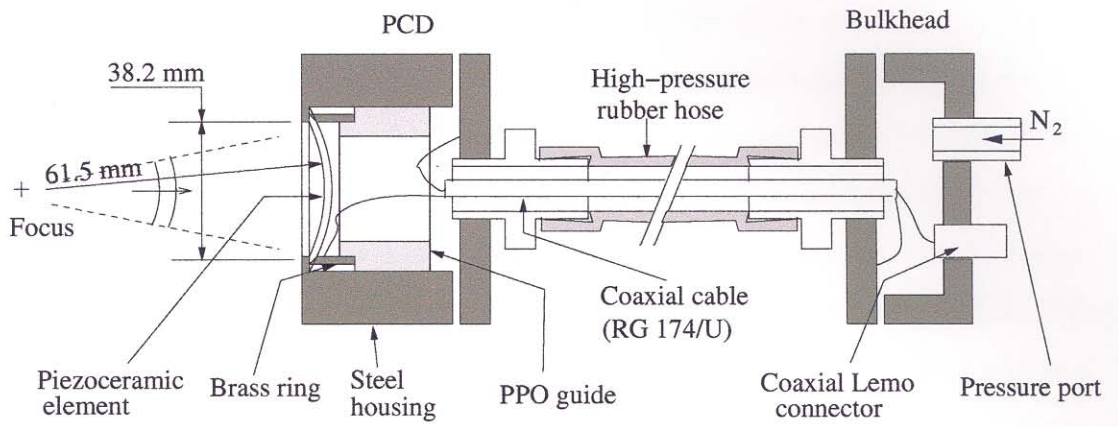


Figure 2.7: Schematic of the PCD and the bulkhead.



Figure 2.8: Picture of the PCD.

The cover of the PCD housing had a port to which was connected a high pressure rubber hose (Swagelok Co., Solon, OH - SS7R4-PM4-PM4-24). A coaxial cable (RG 174/U - 50  $\Omega$  impedance, 0.11" nominal diameter), and compressed nitrogen ( $N_2$ ), both entered the PCD housing through the same port (and the same high-pressure hose). The high-pressure hose was connected to a bulkhead located outside the lithotripter test tank. At the bulkhead the coaxial cable and the  $N_2$  supply were separated. A high-pressure coaxial connector (LemoUSA, Santa Rosa, CA - 0E series coaxial plug and receptacle) was used to lead the signal out of the bulkhead. The bulkhead was connected to a manifold which supplied  $N_2$  at regulated pressure. This design enabled a water-tight electrical connection to the pressurized PCD housing. The transducer could either be air-backed or the housing could be filled with oil (or any other non-conducting fluid). Experiments were performed either with air or oil as backing and there was no significant difference in the results. Results reported here are with an air-backed transducer only.

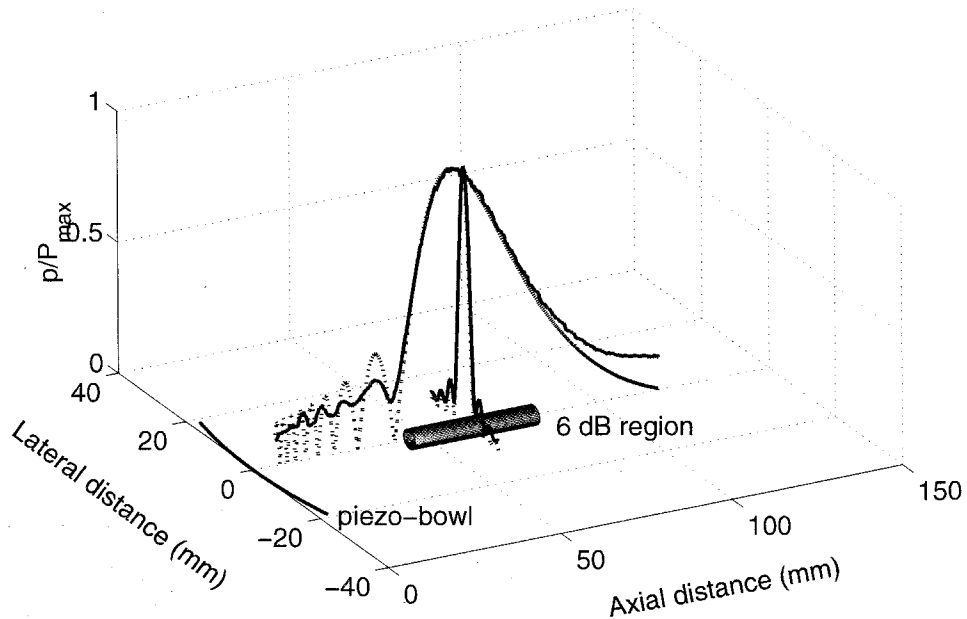


Figure 2.9: PCD acoustic field. Piezo-bowl is located at the origin. – measured, ... calculated from [48].

The acoustic field of the focused receiver was characterized using a PVDF needle-

phone (Imotec Messtechnik, Warendorf - Type 80-0.5-4.0). The needlephone had a sensitive diameter of 0.5 mm and could resolve a rise time of 50 ns. Gated sinusoidal waves of 1 MHz, 20V peak-to-peak amplitude produced by a function generator (Hewlett Packard, Palo Alto, CA - 33120A) were applied to the focused receiver and the acoustic field was scanned by the needlephone. The waves were 10 cycles long, sufficient to achieve a steady acoustic field without causing reverberations from the lithotripter test-tank. The acoustic field attained a maximum at the focus of the receiver. Typically, focused transducers are characterized by the dimensions of a cylindrical 6 dB region near the focus. Figure 2.9 shows the acoustic field of the PCD and 6 dB region. For the PCD used here, this region was measured to have a diameter of 3.7 mm and a length of 36 mm and compared well with the transducer parameters of other investigators (refer [13] for comparison). The dimensions of the 6 dB region of the focused hydrophone were also calculated using O'Niel's approximation [48], and found to be 3.3 mm and 35.8 mm respectively.

Since only the thickness mode signal (1 MHz) is related to bubble activity, the low frequency mode (54 kHz) was filtered out with a combination of passive and active filters. The passive filter was a simple RC high-pass circuit with a 3 dB cut-off point at 300 kHz ( $R = 1 \text{ k}\Omega$ ,  $C = 530 \text{ pF}$ ). The passive filter reduced the radial mode and thickness mode signals to one-third and 85% of their respective original amplitudes. This signal was further processed by an active filter (Krohn-hite, Avon, MA - model 3202) set at a high-pass of 800 kHz. A test signal combination of the two modes (1 MHz, 54 kHz) was produced by the function generator to test the performance of the combined filter. The lower frequency mode was reduced to less than 5% of the thickness mode signal. In the thickness mode the piezoceramic element had a sensitivity of 53.1 V/MPa (sensitivity = voltage/pressure =  $g_{33}t$ , where  $g_{33} = 0.0261 \text{ V m/N}$  was the piezoelectric constant, as cited in the manufacturer's catalogue, and  $t = 2 \text{ mm}$  was the element thickness).

The piezoceramic element combined with the above filter renders it as a narrow band transducer with a resonant frequency of 1 MHz, whereas acoustic emission during inertial collapse of a bubble is reported to be a broadband pulse of very short



duration ( $\ll 1 \mu\text{s}$  - see [71]). Evidently the PCD could not resolve any temporal features of this acoustic emission. A broadband transducer like the membrane hydrophone or the needlephone could resolve more temporal variations, but these do not have sufficient sensitivity to detect these emissions. Corresponding to each bubble emission impinging on the piezoceramic element, the output is an exponentially decaying sinusoid of 1 MHz frequency. Although it is possible to extract the energy of the acoustic impulse from this signal (as done in [13]) the electrical output will be presented without any further processing. These traces (section 3.3) clearly show the timing and relative amplitude of cavitation events.

The filtered signal was digitized by an oscilloscope (Tektronix, Inc., Beaverton, OR - TDS 540A) triggered by the Rogowski coil (section 2.1.1). The oscilloscope was connected to the PC by the GPIB bus through which all communication and data transfer took place. The PC also provided a trigger to a fiber-optic module which in turn triggered the lithotripter (section 2.1.1). Acoustic emissions were measured for single shocks (minimum time interval of 15 s between consecutive shocks) at a lithotripter setting of 18 kV. A Labview program was used to automate these tasks (trigger the lithotripter, initialize the oscilloscope to acquire the PCD signal and store the PCD signal on the PC hard-drive).

### 2.3.2 Pressure chamber

The pressure chamber used for the HP-PCD setup was a hollow aluminum cylinder 63.5 mm (2.5") internal diameter, 12.7 mm (0.5") wall thickness and 152.4 mm (6") long (figure 2.10). PPO end-caps (12.7 mm thick) were used to cover the cylinder ends. The PPO end-caps have been reported to minimally modify the shock wave [64] and at the same time these have sufficient tensile strength to sustain an internal pressure of 10 MPa. The pressure chamber alone could be pressurized to 10 MPa but the HP-PCD could only withstand 7 MPa. Thus, the pressure chamber reported here was similar to that used at IU except for the presence of two circular side-windows 40.6 mm in diameter. Cylindrical aluminum flanges were welded to the pressure chamber

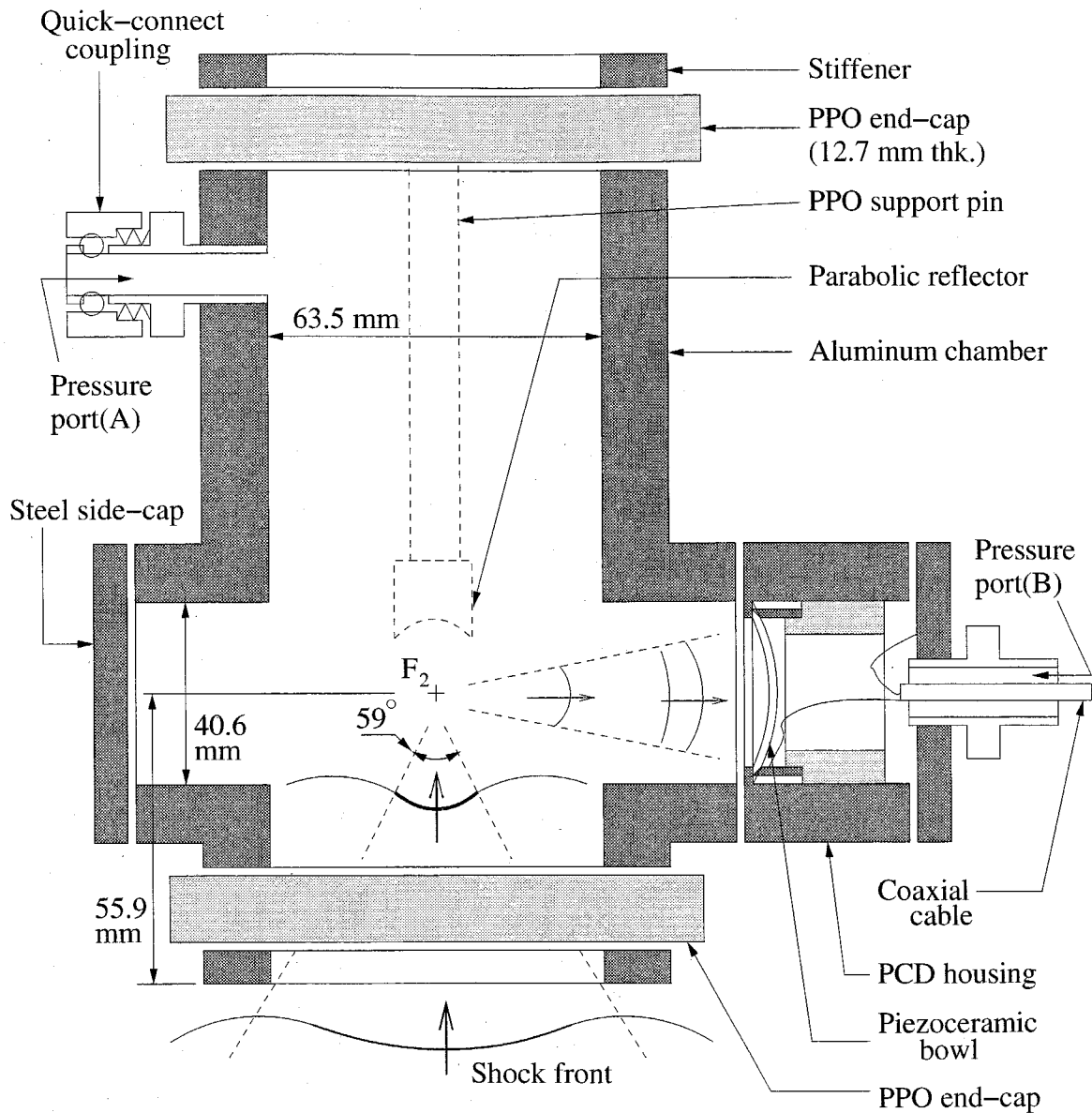


Figure 2.10: Pressure chamber and the PCD (HP-PCD) setup, used for measuring cavitation emission, at static pressures higher than ambient. See text for details.

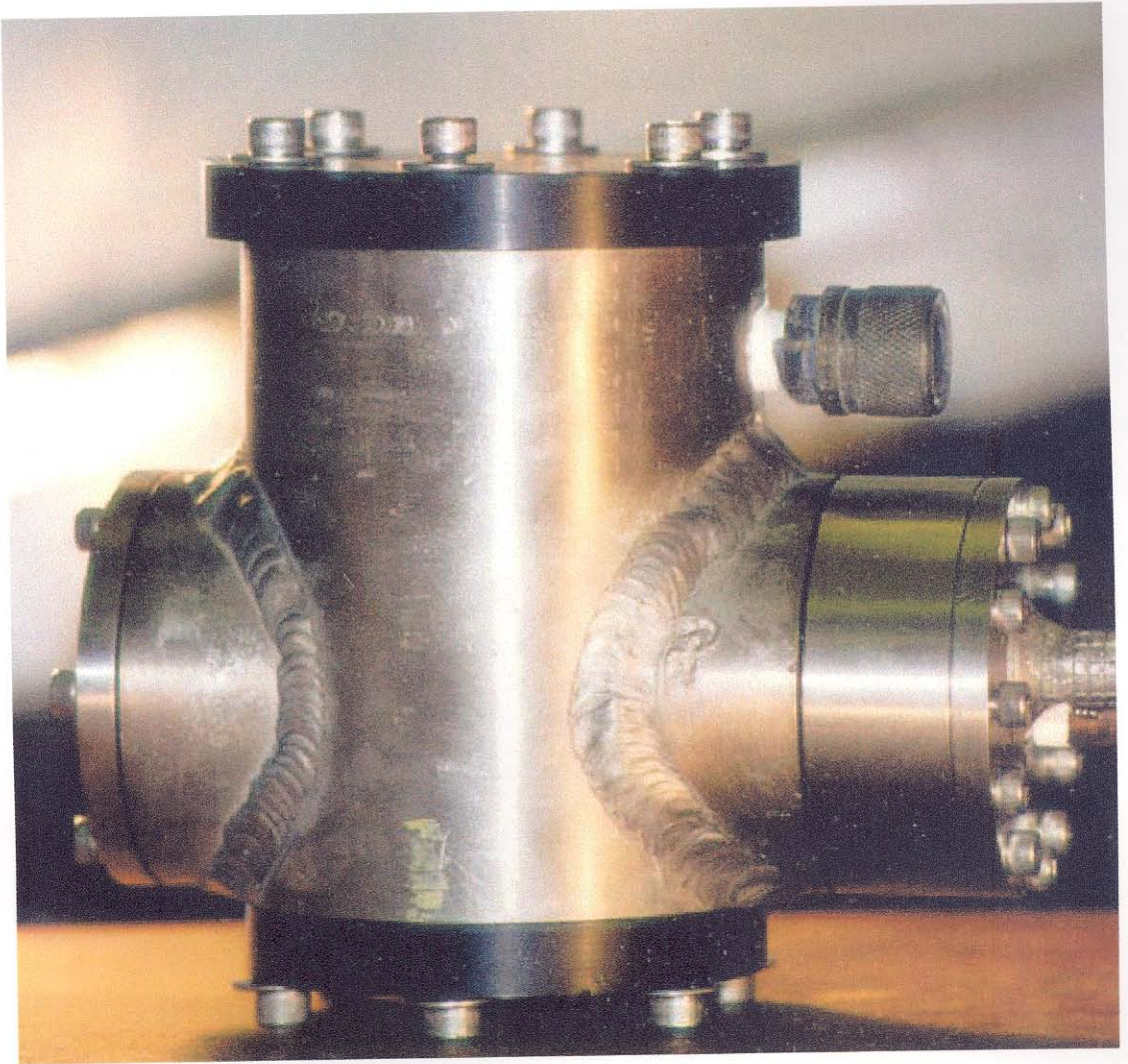


Figure 2.11: Picture of the HP-PCD assembly.

to serve as side-windows enabling us to couple the PCD to the pressure chamber. When not in use the side-windows were covered with steel side-caps. Stainless-steel stiffeners were bolted with the PPO end-caps in order to minimize the deflection of end-caps. The side-windows were designed such that the PCD focused on the chamber axis 55.9 mm from the bottom end of the cylinder assembly.

The cylinder had a port (pressure port (A) in figure 2.10), that could be connected to a high-pressure hose (Swagelok Co., Solon, OH - SS7R4-PM4-PM4-24), using a quick-connect coupling (Swagelok Co., Solon, OH - B-QF-4 series). The other end of this hose was connected to the same N<sub>2</sub> manifold that also supplied the PCD through pressure port (B). The N<sub>2</sub> manifold connected to a N<sub>2</sub> cylinder. A pressure regulator, control valve, pressure gage, and a discharge valve were provided on this manifold (see figure 2.12). Thus, both the pressure chamber and the PCD were pressurized the same. Hence there was no pressure difference across the piezoceramic element and consequently no tensile stresses associated with the overpressure (with a tensile strength of 76 MPa the 2 mm thick piezoceramic element is able to withstand 1 MPa overpressure applied to one side). Two miniature C-clamps were included within the chamber for holding aluminum foils or polymeric films at F2. A cylindrical PPO support pin was attached to the top PPO end-cap, to hold the parabolic or flat reflector. The HP-PCD assembly was mounted on the motor driven X-Y-Z slides, described in section 2.1.4 (refer figure 2.12 for a schematic). This enabled alignment of the HP-PCD assembly with the lithotripter acoustic axis and F2.

The internal diameter of the pressure chamber (63.5 mm), and the axial location of F2 from the bottom end of the chamber assembly (55.9 mm) created an effective aperture of 59° (figure 2.10). The aperture of the hemiellipsoidal reflector of the lithotripter is 68° (see [12]), thus we expect some truncation of the wavefront. This was assessed by measuring the waveform at F2 inside the pressure chamber using the Imotec needlephone. The peak positive and negative pressures of the lithotripter pressure trace were reduced by less than 5%, and the overall wave profile was not altered despite the presence of the pressure chamber. With the PCD assembled to the pressure chamber, the needlephone was introduced from the opposite window



and the acoustic field of the PCD was scanned (procedural details discussed in section 2.3.1). The acoustic field of the PCD was unchanged, indicating that the reflections from the chamber or window walls did not influence the acoustic field of the focused hydrophone.

## 2.4 Foil exposure

Aluminum foil (Reynolds Wrap from Reynolds Metals Co., Richmond, VA – 38  $\mu\text{m}$  thick) and cellophane film (Highland Supply Corp., Highland, IL – 25  $\mu\text{m}$  thick film) targets were used to study shock wave damage. Prior to shock wave exposure, samples of these targets were scanned using an atomic force microscope (AFM) to obtain their surface topological features. This was done in order to obtain the roughness of the surface, which is an indicator of the capability of the surface to trap air and provide cavitation nuclei. The aluminum foils had a surface roughness (average peak to depth) of about 800 nm. Cellophane film had a surface roughness of only 40 nm, hence much smoother than aluminum foil. The targets were exposed to lithotripter wave-field and the refocused wave-field at different overpressures. The targets were oriented perpendicular to the lithotripter acoustic axis. After shock wave exposure aluminum foils were examined under a microscope (Nikon MM-22) at 25X – 200X magnification (GALCIT). Photographs were also taken (IU) using a digital camera (Nikon - CoolPix 990) in order to obtain the three-dimensional features of the foil deformation. Cellophane films were scanned (Hewlett Packard, Palo Alto, CA - Scanjet 4c). Results are discussed in section 3.4 and are for a lithotripter setting of 18 – 20 kV at 1 Hz pulse repetition rate.

## 2.5 Cell lysis

Cell lysis experiments carried out in this study were similar to those described previously [75] with the exception that the cells were held in a vial stoppered with a parabolic (or flat) reflector. Brass reflectors were used for the acoustic and bubble

emission measurements described in sections 2.2 and 2.3 while stainless-steel reflectors were used with cells. The acoustic impedance of brass is very close to that of stainless-steel (27 and 30 times that of water), so the reflectors were considered acoustically equivalent. Briefly, freshly drawn human RBC's were washed with phosphate-buffered saline (PBS) and suspended at a volume concentration of 3.1%. Vials fashioned from the bulb end of polyethylene pipets [74] were filled with cell suspension and then plugged with a reflector. Care was taken to avoid introducing bubbles into the vial. This resulted in a polyethylene container with rounded end filled with the RBC suspension (about 2 ml total) that was in direct contact with the reflector (figure 3.17a).

Studies with RBC's were performed at IU by Drs. James McAteer and James Williams using the overpressure chamber described in [64]. Vials were mounted round-end down, centered on the acoustic axis and positioned so that the F2 of the lithotripter (corrected for the focusing effect of PPO) was 3 mm from the aperture plane of the parabolic (or flat) reflector. Prior to shock wave treatment the pressure in the chamber was adjusted to  $\sim 12$  MPa. Vials were exposed to 150 shock waves (20 kV, 1 Hz). Controls included vials that were pressurized and not exposed to shock waves, and vials that were not pressurized and not shock wave treated. Following shock wave exposure in the presence of either the parabolic or flat reflector an aliquot of cell suspension was taken for measurement of cell lysis. The cell suspensions were centrifuged at 6000g for 10 min and absorbance of the supernatant measured at 414 nm. Cells in the pellets were lysed with detergent and absorbance similarly determined. Lysis was calculated as percent of total hemoglobin released into the supernatant.

# Chapter 3 Experimental results

## 3.1 Lithotripter characteristics

Measurements of the acoustic field and the electrical parameters of the GALCIT lithotripter are described in this section.

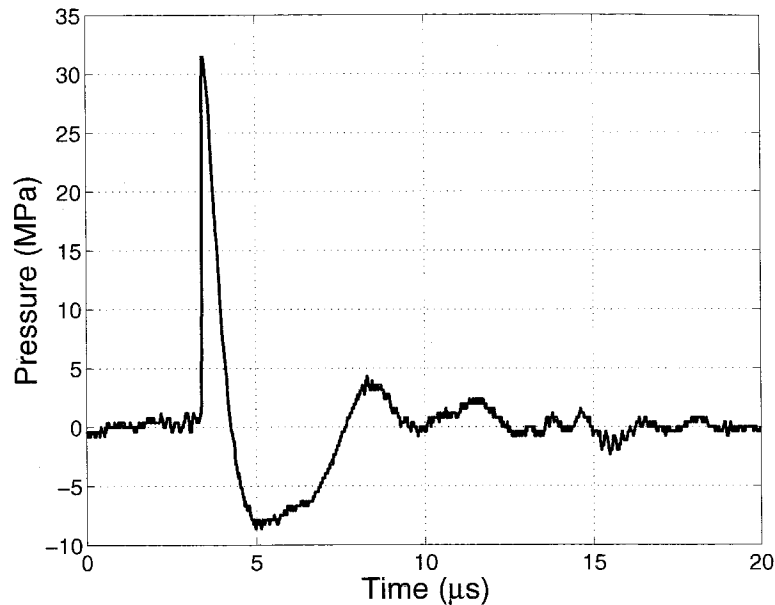


Figure 3.1: Pressure pulse at lithotripter focus.

### 3.1.1 Lithotripter acoustic field

Figure 3.1 shows the pressure trace, measured by the membrane hydrophone, located at F2. The lithotripter pressure trace, at F2, comprises of a leading shockfront, which decays to zero in  $1 - 2 \mu\text{s}$ , and has a negative tail of  $4 - 6 \mu\text{s}$  duration. The amplitude of the shockfront at F2 (denoted as  $p_{max}^+$ ) is measured to be  $\approx 35 \text{ MPa}$  (see [12]). Though measurements indicate a shock rise time of  $50 \text{ ns}$ , the shockfront is estimated to be  $40 \text{ ps}$  ( $60 \text{ nm}$ ) thick (see [65]), for the above shock-strength. The  $50 \text{ ns}$  shock



thickness measurement can be attributed to two reasons, imperfect alignment of the hydrophone with the shock plane, and more importantly, the limited bandwidth of the hydrophone (50MHz bandwidth means a temporal resolution of 20 ns). The negative tail has an amplitude ( $p^-$ ) of 10 MPa. The wave amplitude decays farther away from the axis, and has a 6 dB beamwidth (i.e., location where the shock amplitude drops to half the peak value) of 1 cm. This can be seen from figures 3.8a & 3.8b, where the dashed line plots the off-axis distribution of peak pressures ( $p^+$ ,  $p^-$ ) in the plane of F2, for the lithotripter wave. Similar pressure traces for Dornier ESWL's have been reported earlier [17, 45].

### 3.1.2 Electrical parameters

The characteristics of the high voltage system were measured during a spark discharge. Figure 3.2 shows the current measured by the Rogowski coil during the discharge of shorted electrodes in both the GALCIT lithotripter and the HM3-A clinical machine at the Methodist Hospital, Indianapolis. The maximum current of the HM3-A is about 30% larger than that of the GALCIT EHL. Given a capacitance of 80 nF, measurements of the frequency and decay time of these traces can be used to calculate the circuit inductance  $L_c$  and the resistance  $R_c$ . These are given as a function of capacitor discharge voltage for both the GALCIT EHL and the HM3-A in Fig. 3.3. The GALCIT machine showed more scatter than the HM3-A, and the resistance of the GALCIT machine varied more strongly with the supply voltage. Both of these features are attributable to differences between the EG&G trigger switch and the switch used in the Dornier HM3. The higher resistance in the research lithotripters is probably associated with parasitic resistance in both the trigger gap and the capacitors. Quantitative results for  $L_c$  and  $R_c$  at 18 kV are given in table 3.1. The effect of the larger inductance of the research lithotripters is to slightly reduce the resonant frequency of the circuit, from 2.28 MHz to 2.17 MHz, and that of the increased resistance is to reduce the number of cycles during which the discharge current decays, from 11 to 5. Since the rise time of the current pulse is nearly

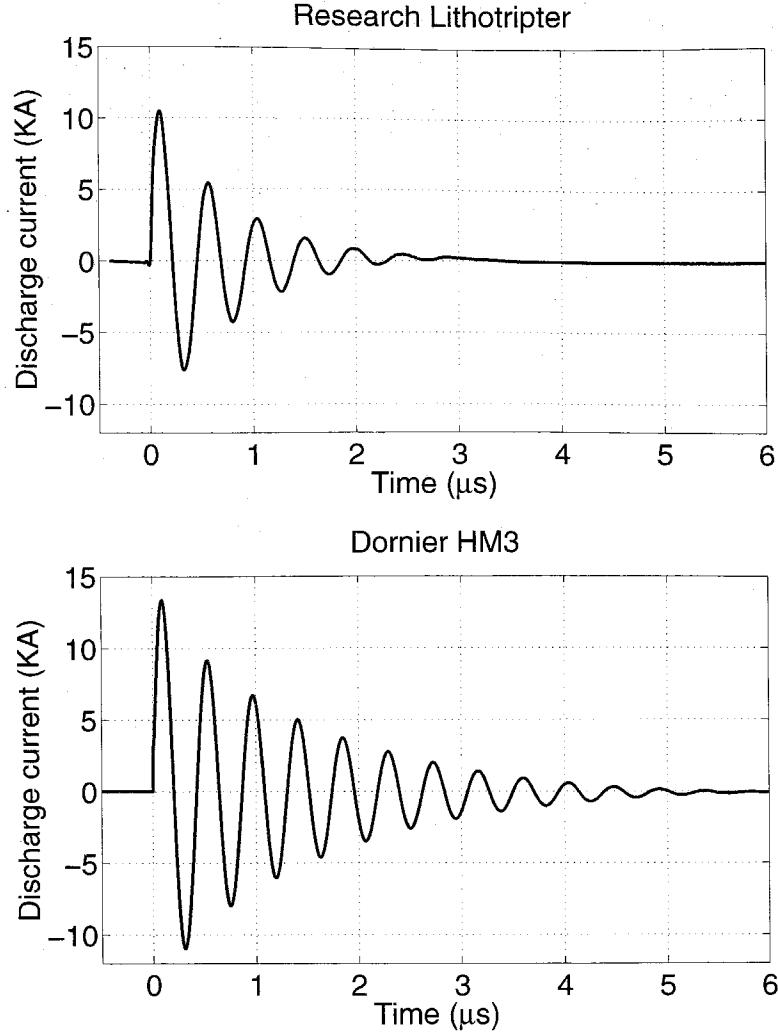


Figure 3.2: Discharge current measured by the Rogowski coil.  $V_0 = 18$  kV, shorted electrode. Top, GALCIT EHL; bottom, HM3-A.

Machine	$L_c$ (nH)	$R_c$ ( $\Omega$ )
HM3-A	$60.5 \pm 0.4$	$0.093 \pm 0.008$
GALCIT EHL	$66.7 \pm 2.8$	$0.177 \pm 0.012$

Table 3.1: Inductance and resistance at 18 kV.

the same in the two machines, the parameters of the shock waves generated by the Caltech EHLs are expected to reproduce those of the HM3. The major consequence of the substantially larger resistance in the Caltech lithotripters should be that the capacitor life is extended. When the spark is struck in water, as during the normal

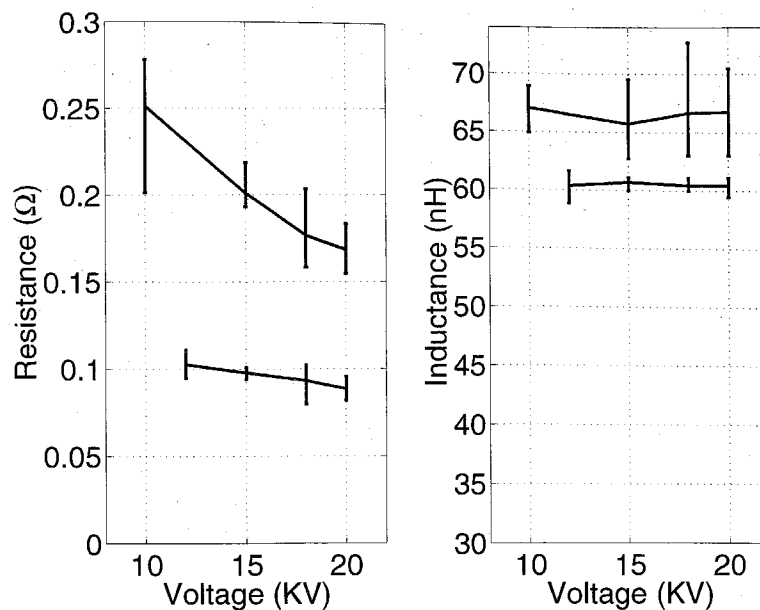


Figure 3.3: The resistance  $R_c$  (left) and inductance  $L_c$  (right) of the lithotripter spark supply circuits. Top curves, GALCIT EHL; bottom curves, HM3-A. Note the truncated scale of inductance.

lithotripter operation, the plasma gap adds an additional variable resistance to give a total resistance (for the GALCIT EHL) of  $0.233 \pm 0.013 \Omega$ , while other measured parameters remain the same. From the  $R_c$  and  $L_c$  values the Caltech machines very closely mimic the parameters of the HM3.

### 3.1.3 Effect of pulse repetition frequency

The ability of the research machines to maintain consistent output over a range of clinically relevant firing rates was also investigated. In clinical settings the HM3 is typically synchronized to the patient's heart beat and fired at 1-2 Hz. The synchronization is required because some patients suffer arrhythmia if the discharge occurs in certain parts of the heart cycle; however, often it is possible to fire the HM3 faster. Figures 3.4 & 3.5 show the variation in the characteristics of the high voltage system (discharge resistance and peak current) and the acoustical output (peak positive and peak negative pressures at the focus) as a function of voltage and firing rates in the GALCIT lithotripter.

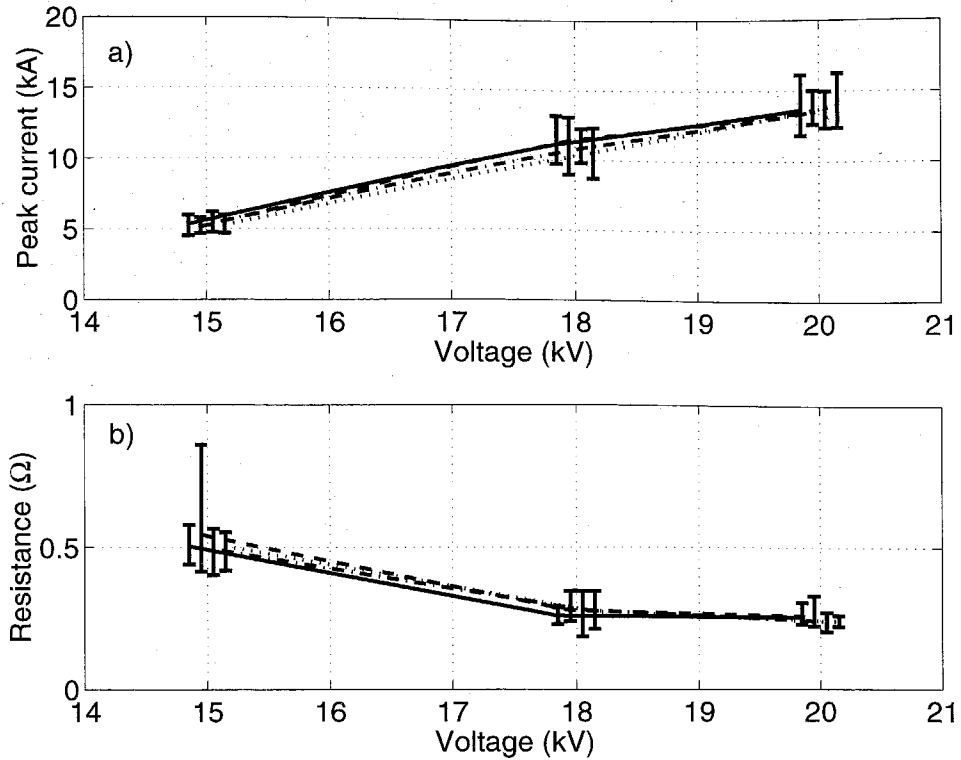


Figure 3.4: Variation in electrical parameters of the GALCIT lithotripter (resistance and peak current) as a function of firing rate and voltage. Legend : – single shock, - - 1 Hz, - · - 2 Hz, · · · 3 Hz.

As seen from figure 3.4 the measured resistance and peak current is independent of firing rate. These, however, vary with voltage: the resistance is significantly higher at 15 kV and the peak current increases monotonically with voltage. The maximum peak positive pressure increased significantly with increasing voltage regardless of the pulse rate. The peak positive pressure did not vary significantly with pulse rate, except for a rate of 2 Hz which was statistically higher than a rate of 1 Hz. The magnitude of the peak negative pressure increased significantly with increasing voltage regardless of the pulse rate. The magnitude of the peak negative pressure decreased with increasing firing rate. This was the only parameter that varied with pulse rate and this could probably be due to cavitation induced bubbles collecting on the surface of the membrane hydrophone.

Finally, the pressures at the focus were measured over successive shots to ensure

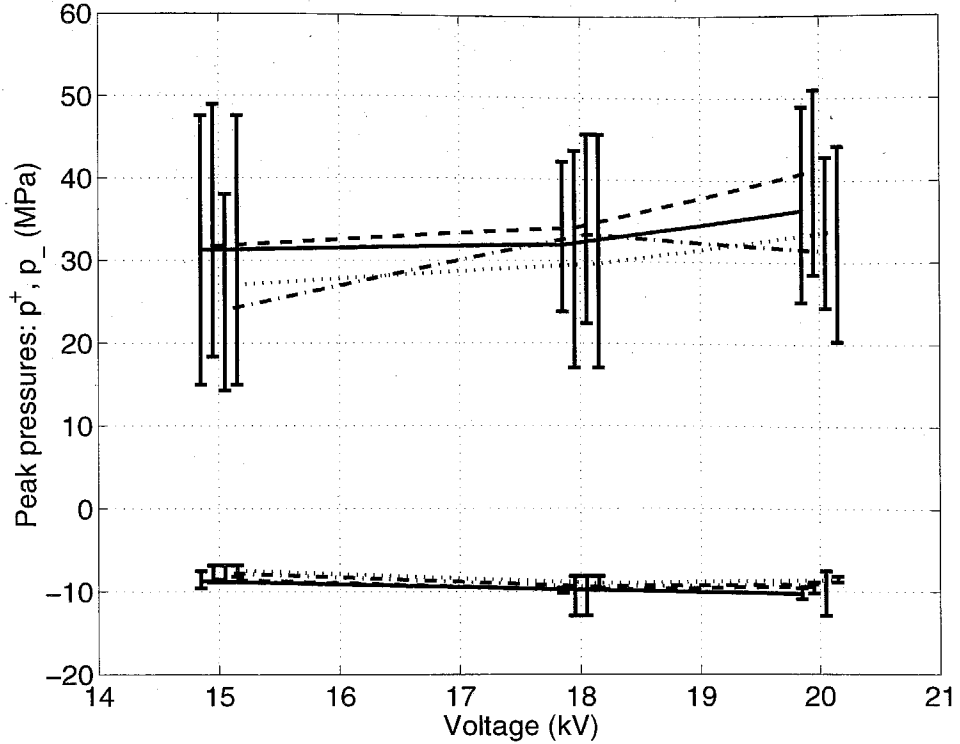


Figure 3.5: Variation in peak pressures ( $p^+$ ,  $p^-$ ) of the GALCIT lithotripter as a function of firing rate and voltage. Legend : — single shock, - - 1 Hz, --- 2 Hz, ... 3 Hz.

that the output remained constant. Figure 3.6 shows the peak pressures at the focus after 2, 10 and 20 shock waves at firing rate of 2 Hz. The voltage was held fixed at 18 kV. This measurement shows that neither peak positive pressure nor peak negative pressure is affected by the number of shots. These results indicate that the acoustic output and the electrical parameters of the Caltech lithotripters remains stable over consecutive shots, at various firing rates, and at various voltages.

## 3.2 Refocused wavefield

The pressure trace and the acoustic field of the reflected wave can be seen in figures 3.7 and 3.8, respectively. These measures were collected using the membrane hydrophone positioned in the plane of F2 and, therefore, immediately in front of the reflector. Thus, the lithotripter wave hits the hydrophone before it strikes the reflector to be

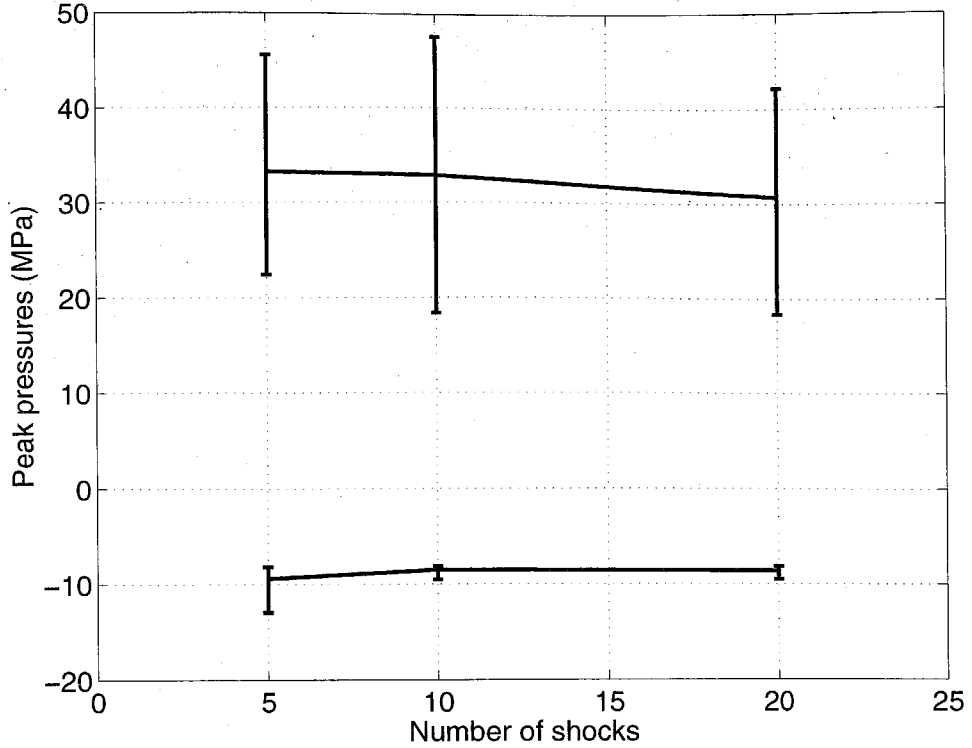


Figure 3.6: Variation in peak positive pressure and peak negative pressure as a function of number of shots for a firing rate of 2 Hz.

reflected back to hit the hydrophone a second time. The time required for the wave to travel from the hydrophone to the reflector and back is approximately  $5 \mu\text{s}$ . In figure 3.7, a reflected shock with a 50 ns rise time is clearly seen for the flat reflector case (right column). For the parabolic reflector (left column) the reflected shock did not show a similar rise time. This was due to difficulty in aligning the reflector and the hydrophone at F2. Even with perfect alignment of the hydrophone and the parabolic reflector with the lithotripter acoustic axis and F2, the shot-to-shot variability of the lithotripter rendered this alignment meaningless.

The off-axis variation of the peak pressure amplitudes ( $p^+$ ,  $p^-$ ) for the parabolic and flat reflector wave-fields and the lithotripter wave-field is compared in figure 3.8. As expected, the focusing effect of the parabolic reflector is higher than the original lithotripter wave. The wave reflected off the flat reflector also has some focusing effect. A possible explanation is that the lithotripter wave incident on the reflector

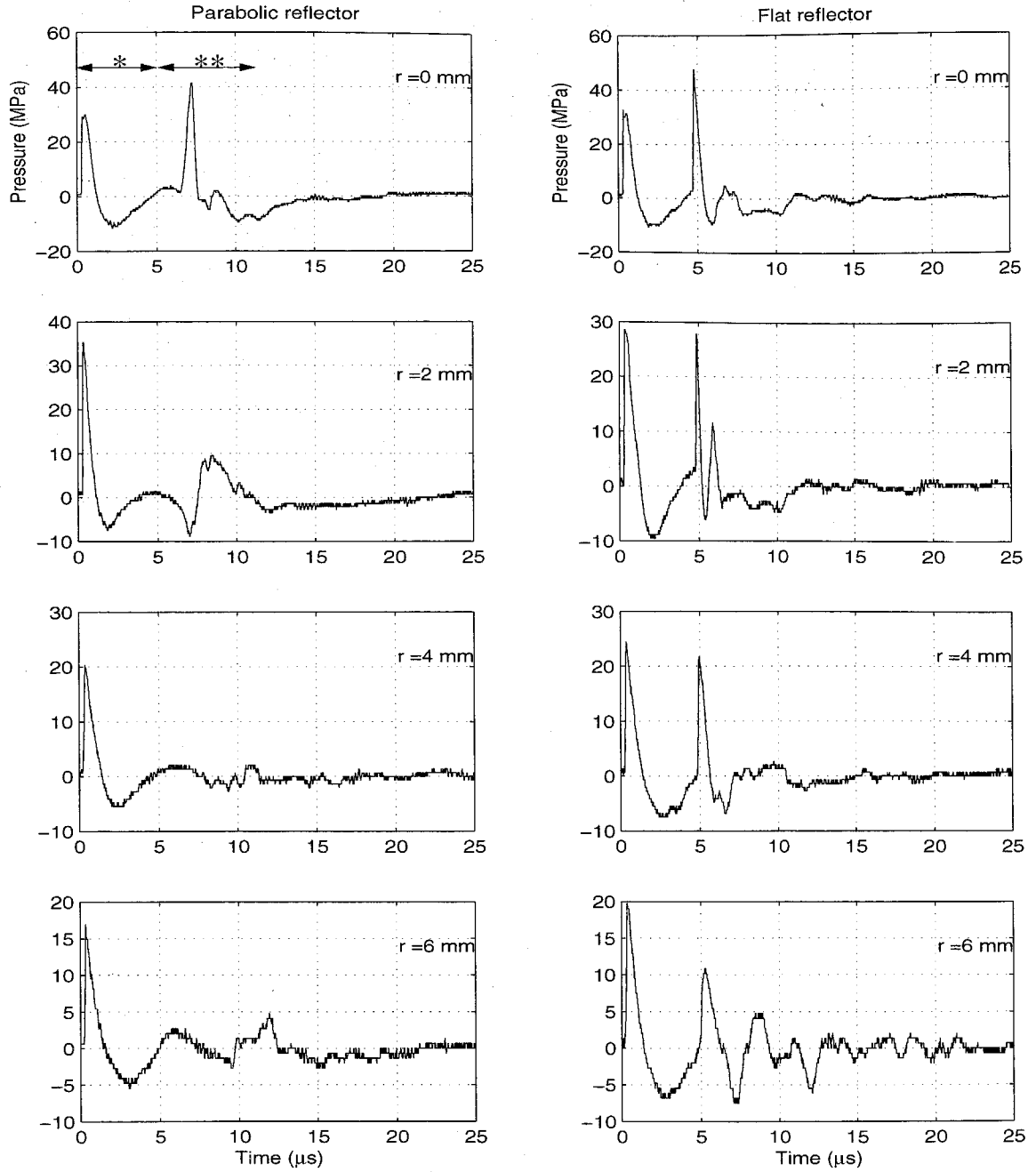


Figure 3.7: Pressure trace measured in the focal plane, at  $r = 0, 2, 4$  and  $6$  mm from the acoustic axis ( $r = 0$ ). The leading pulse (first  $5 \mu$ s) is the lithotripter wave, and the trailing pulse is the reflected wave (marked '\*' and '\*\*', respectively, in top left trace). a) Left column, off the parabolic reflector. b) Right column, off the flat reflector.

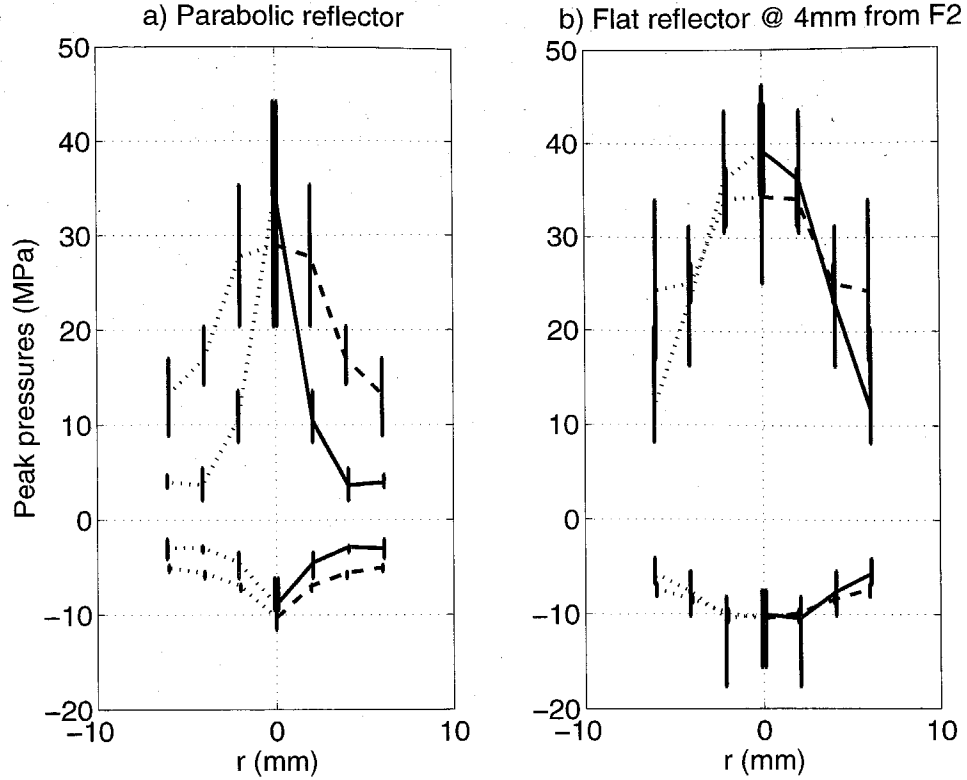


Figure 3.8: Off-axis variation of peak pressures, measured at  $r = 0, 2, 4$ , and  $6$  mm from the acoustic axis ( $r = 0$ ). Solid and dashed lines indicate variation of reflected and lithotripter wave-field, respectively. Scans shown for  $r < 0$  are shown dotted, since these are replica of  $r > 0$ , flipped over. a) Parabolic reflector. b) Flat reflector.

	$p_{max}^+$ (MPa)	6 dB width (mm)	$k(\sim \partial u_z / \partial r)$ ( $s^{-1}$ )
Lithotripter wave	35 – 40	10	$1.25 \times 10^3$
Reflected wave :			
Parabolic reflector	37	5	$2.5 \times 10^3$
Flat reflector	38	7	$1.8 \times 10^3$

Table 3.2: Comparison of acoustic fields.

may not be perfectly planar, but may have some curvature. The values of  $p_{max}^+$ , 6 dB width, and the resultant velocity gradient ( $k$ ) are listed in table 3.2. The velocity gradient is calculated from the acoustic velocity due to  $p_{max}^+$ , and the 6 dB width ( $k = 1/2 (p_{max}^+ / \rho c) / (6 \text{ dB width})$ ). The parameter  $k$  which is a measure of the rate of flow-field deformation, and hence its lytic effectiveness, is highest for the reflected



wave-field off the parabolic reflector.

### 3.3 Bubble emission measurements

The acoustic emission measurements described below are divided into two parts: ‘free-field’ and ‘closed-field’ measurements. Acoustic emission measurements made using the PCD without any pressure chamber are denoted as free-field, whereas those obtained by the HP-PCD are denoted as closed-field in order to indicate the constraining effect of the pressure chamber on bubble activity.

#### 3.3.1 Free-field emission

Figure 3.9 shows typical ‘double-bang’ emissions at F2 of our research lithotripter. Since there is considerable variability in these emissions, ten traces are shown here. For any given trace, the first emission can be seen at  $t \sim 0$ , and the second emission (i.e., from inertial collapse) occurs at  $t \sim 300 \mu\text{s}$ , of about 0.5 V amplitude. In all the PCD signals, reported here, the time-scale has been offset by the amount of time elapsed from the instant the capacitor discharges (detected by the Rogowski coil) to the instant when the first acoustic emission reaches the piezoceramic element. This total time ( $228 \mu\text{s}$ ) is a summation of travel time taken by the lithotripter wave to reach F2 ( $186.6 \mu\text{s}$ ) and for the acoustic emission to travel from F2 to the PCD ( $41.3 \mu\text{s}$ ). In the vicinity of the second emission ( $300 \mu\text{s}$ ), other smaller signals can also be seen. One plausible explanation is that the collapsing bubble regrows and recollapses, i.e., it rebounds after the first inertial collapse. The smaller signals succeeding the first major pulse could be attributed to this recollapse. Alternatively these signals could be due to cavitation events occurring outside the focal region of the lithotripter (F2). In this case the signal might reach the PCD earlier than the emissions from F2.

For the lithotripter wave the time between the two collapse events was found to vary from  $250 - 350 \mu\text{s}$ . This is in good agreement with other measurements (from figure 6a in [13], this time is  $250 - 325 \mu\text{s}$  for identical experimental conditions). The acoustic emissions were also measured transverse to the acoustic axis. The amplitude

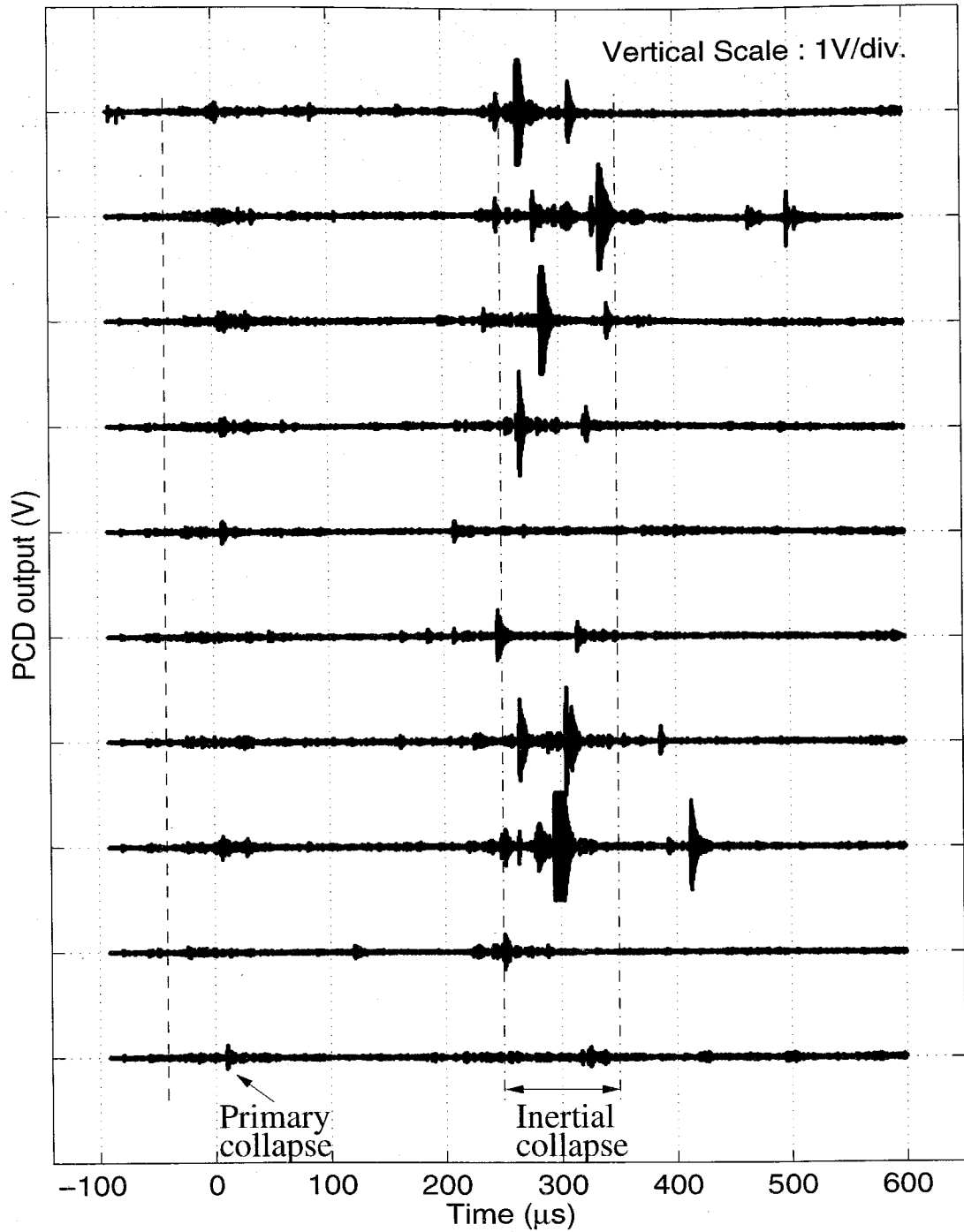


Figure 3.9: Free-field bubble emission (i.e., no pressure chamber - at ambient pressure), in response to the lithotripter wave, as detected by the PCD. Ten traces are shown here to give an indication of the variability in the measurements. Time-scale has been offset by the time taken by bubble emission at F2 to reach PCD. Dotted line (@  $-41.3 \mu\text{s}$ ) indicates time of shock wave arrival at F2. Measurements are offset by multiples of 1V for clarity.

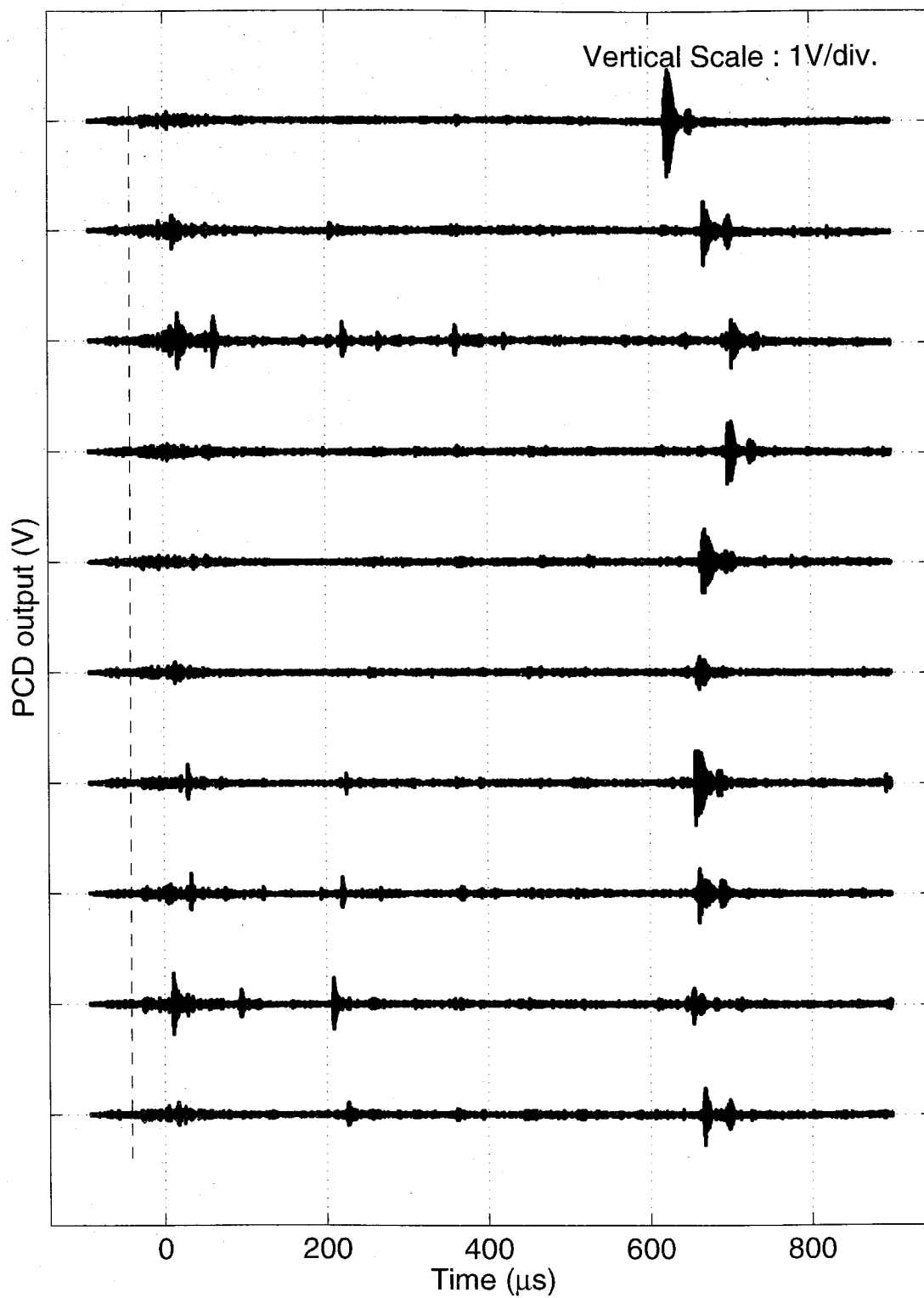


Figure 3.10: Free-field bubble emission in response to the reflected wave from the flat reflector.

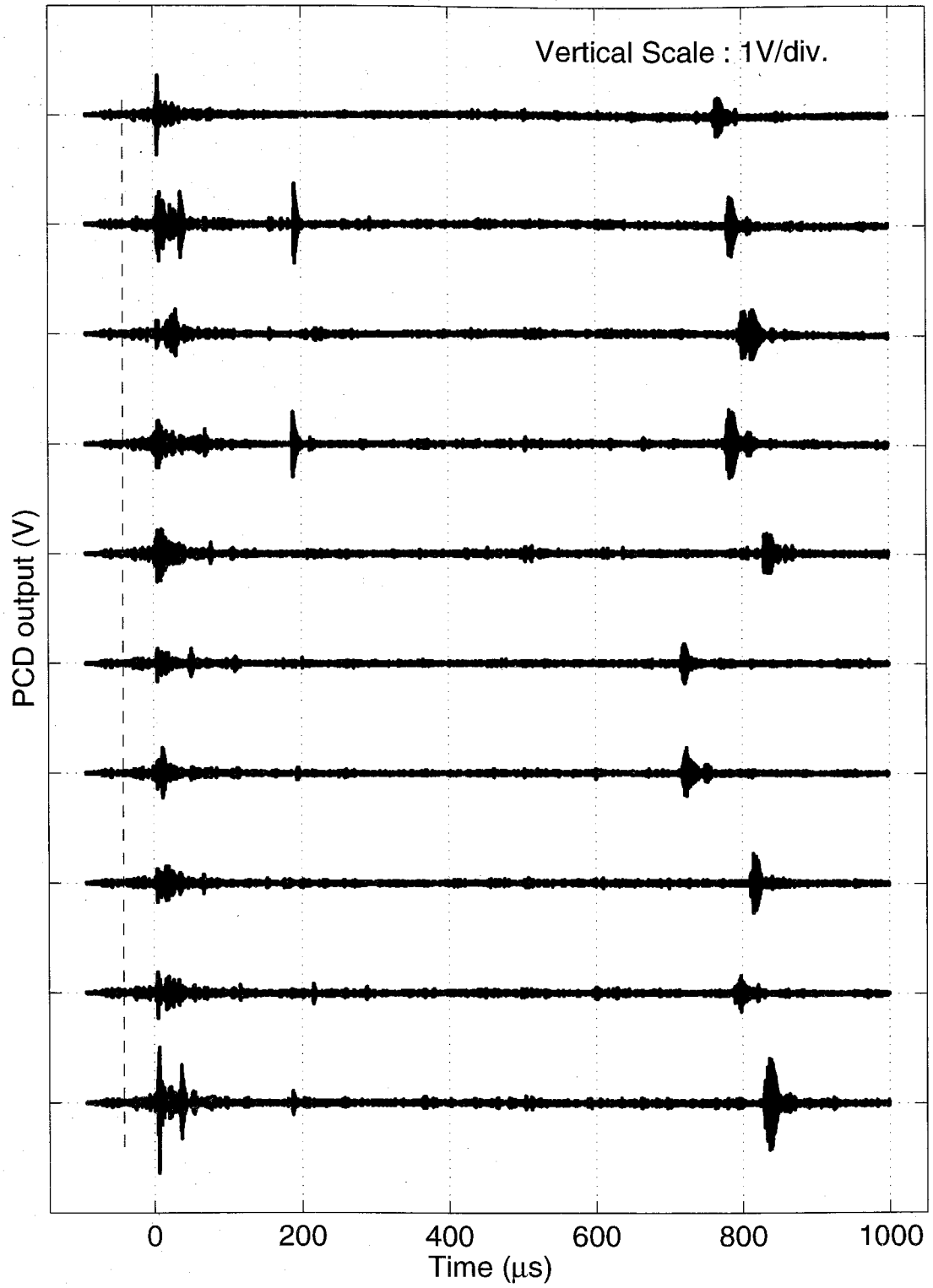


Figure 3.11: Free-field bubble emission in response to the reflected wave from the parabolic reflector.

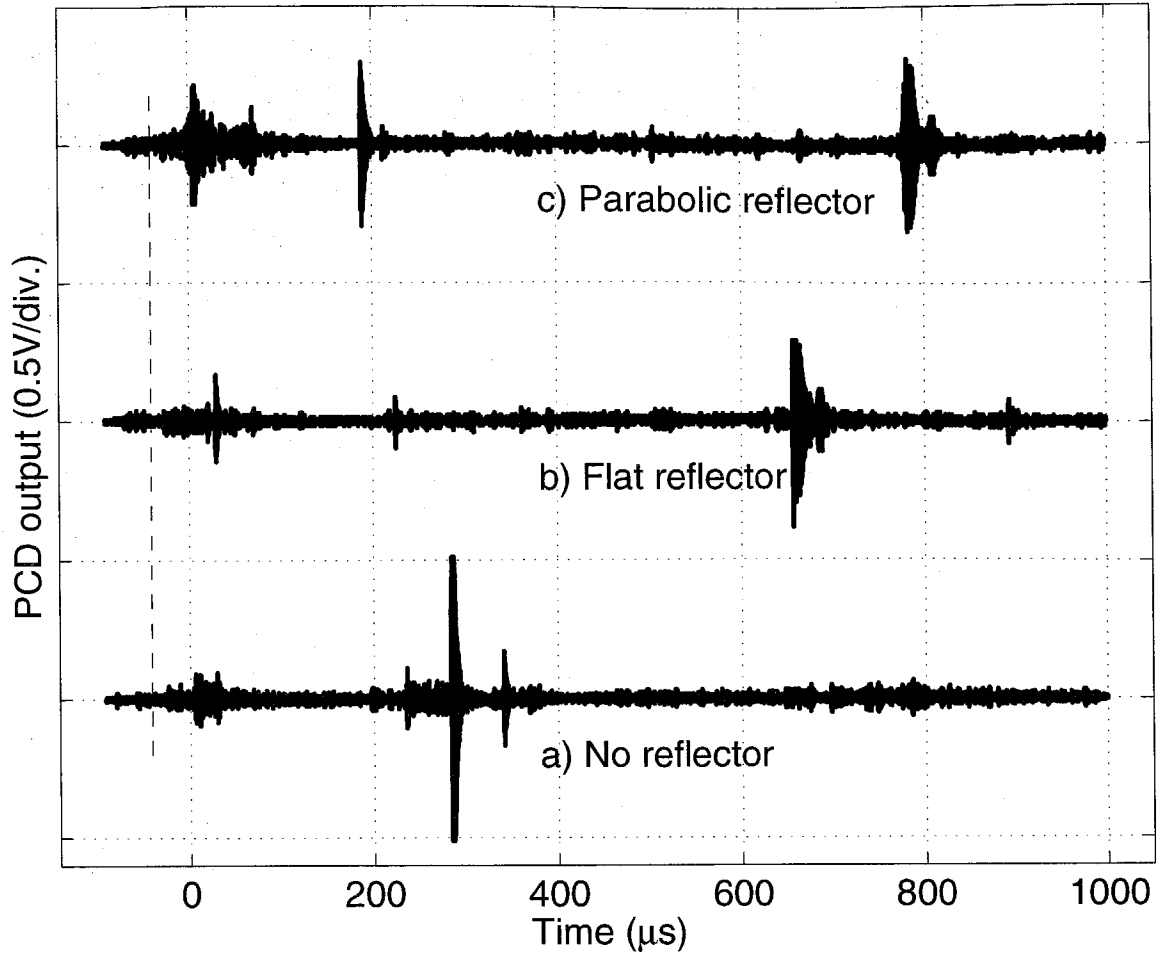


Figure 3.12: Comparison of free-field emission - Response to: a) Lithotripter wave. b) Reflected wave from flat reflector. c) Reflected wave from parabolic reflector.

of the emissions decayed with distance from F2; however, the time duration between the two collapses remained in the above range. This observation is consistent with bubble-cloud behavior rather than the activity of a single bubble which would predict a smaller collapse time.

The acoustic emission for the reflected wave-field, using a parabolic or flat reflector, is shown in figures 3.10 and 3.11. Figure 3.12 compares the emission from the three wave fields (i.e., lithotripter wave versus the reflected wave from parabolic and flat reflectors). The strong inertial collapse (0.5 – 1 V) seen at 250 – 350  $\mu\text{s}$  without any reflectors was weaker ( $< 0.3$  V) and observed only occasionally. However,

another weak signal ( $< 0.3$  V) was invariably seen at  $t \sim 600 - 800 \mu\text{s}$ . Thus, it is speculated that the reflected wave delays the cloud collapse to later than  $600 \mu\text{s}$  and the collapse expected to occur at  $250 - 300 \mu\text{s}$  either did not occur, or was weak. Single-bubble calculations (using the Rayleigh model [56]) with the bubble subjected to the lithotripter wave and the reflected wave, however, did not predict such a modification in the timing or strength of the collapse events. This modification was likely due to bubble-cloud dynamics, and the presence of the rigid reflector wall close to the bubble cloud. Single-bubble models assume an unbounded fluid, a condition no longer satisfied in this case due to proximity of the reflector to the bubble cloud.

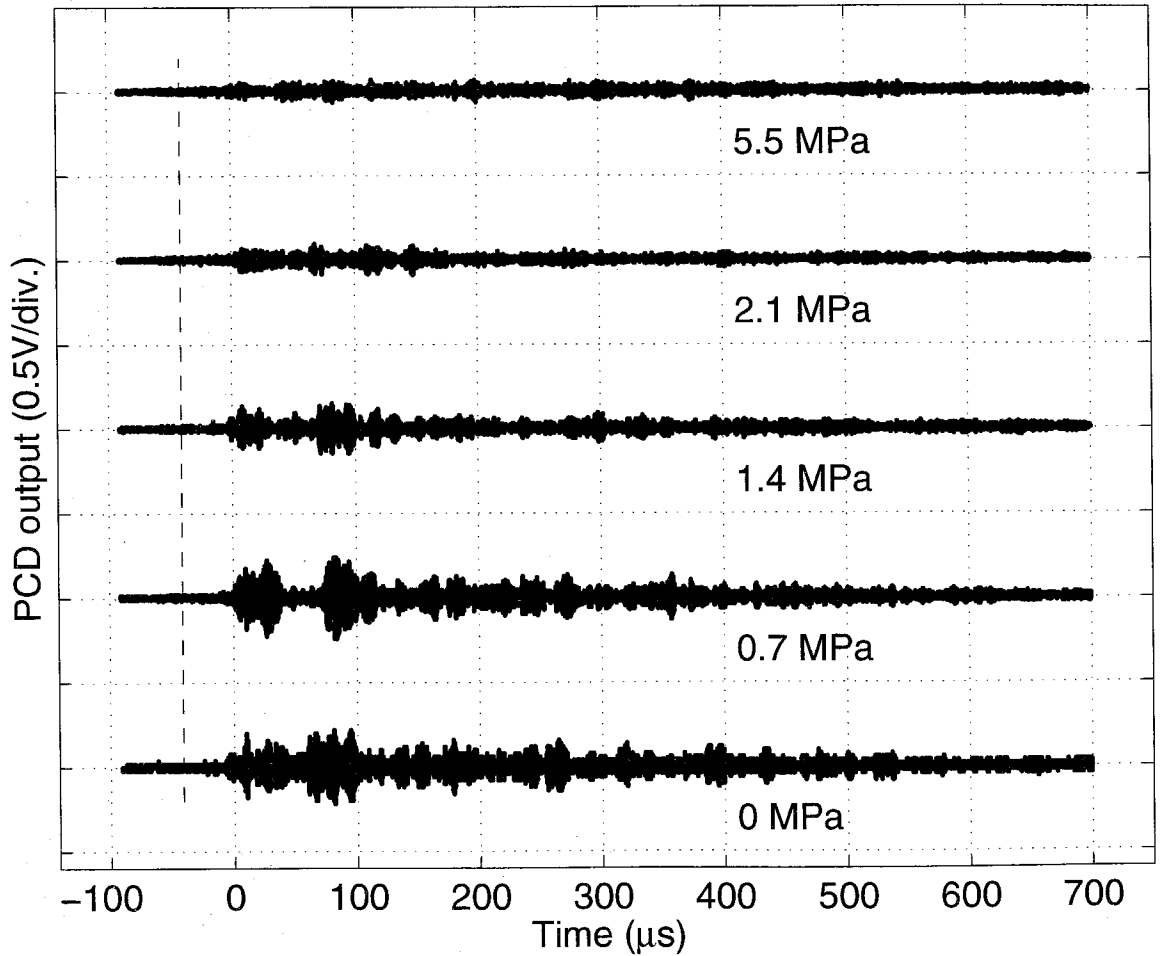


Figure 3.13: Closed-field bubble emission in response to the lithotripter wave. Shows effect of increasing overpressure (0 – 5.5 MPa).

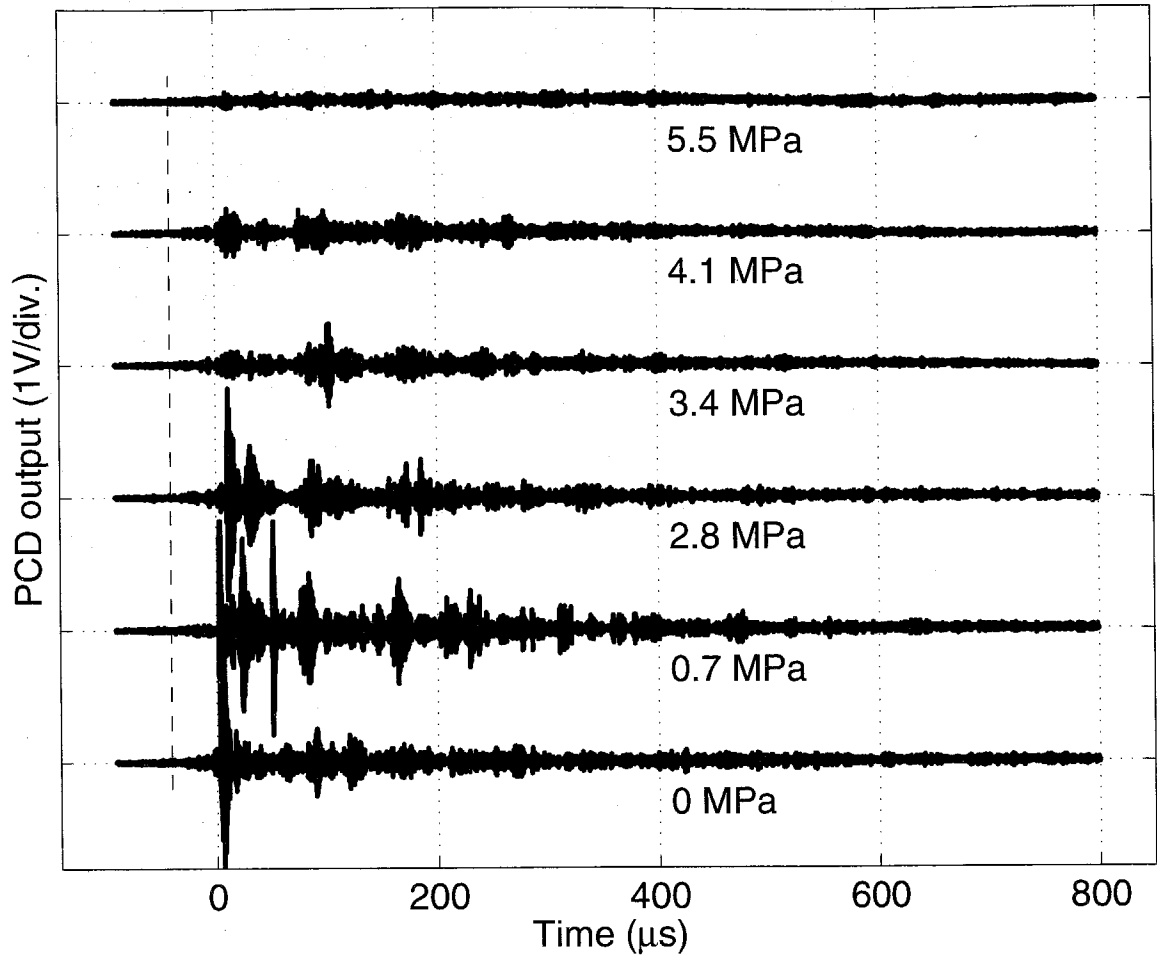


Figure 3.14: Closed-field bubble emission in response to the wave reflected by the parabolic reflector. Shows effect of increasing overpressure (0 – 5.5 MPa).

### 3.3.2 Closed-field emission

Figure 3.13 shows measurements of the lithotripter wave-field using the HP-PCD with increasing overpressure (0 – 5.5 MPa). The acoustic emission measured at 0 MPa overpressure was significantly different from that in the free-field (figure 3.9) even though the lithotripter wave-field was identical (see section 2.3.2) in both cases. The water used in both these measurements (i.e., free-field and closed-field) was identical and same as that of the lithotripter test-tank. In order to fill the pressure chamber with water, it was immersed in a water-filled trough and the side-caps and end-caps were assembled under water. The high-pressure hose was also partially

filled. This ensured that there were no air bubbles trapped inside the chamber. All other experimental parameters, e.g., firing rate, supply voltage setting, filters used for signal processing, were the same.

Inertial collapse expected at  $250 - 350 \mu\text{s}$  following the primary collapse was not detected. Instead of exponentially decaying sinusoids which indicate discrete events in the bubble growth-collapse cycle, a continuum of weak signals ( $< 0.2 \text{ V}$ ) was recorded over the  $0 - 500 \mu\text{s}$  period. The source of these signals is not clear; however, we speculate that the coherent bubble-cloud collapse which was responsible for the typical double-bang signature no longer exists or was too weak to be detected. Increased overpressure caused these signals to diminish in strength and duration until eventually no signals were detected (@  $5.5 \text{ MPa}$ ). Investigating bubble dynamics in this closed-field is beyond the scope of this work, and it suffices to state here that beyond a threshold overpressure of  $5.5 \text{ MPa}$ , no bubble activity was detected.

Figure 3.14 shows the emission measurements using the HP-PCD, for the wave-field reflected by the parabolic reflector, with increasing overpressure ( $0 - 5.5 \text{ MPa}$ ). Regardless of the overpressure there was no emission seen at either  $250\text{--}350 \mu\text{s}$  or at  $600\text{--}800 \mu\text{s}$ . However, very strong emissions occurred at  $t \sim 0$  which could be due to scattering of the shock wave from the bubble, or from a primary collapse event. Again, elevating the overpressure above  $5.5 \text{ MPa}$  caused all emissions to die out.

### 3.4 Foil damage data

When aluminum foils are exposed to lithotripter shocks at ambient pressure, ‘pitting’ damage is commonly seen (e.g., [3, 37]). These pits have been observed to be of the form of rounded depressions surrounded by a toroidal ring [16]. Such pitting deformation has been attributed to asymmetrical bubble collapse in the vicinity of the foil. Figure 3.15a shows this pitting damage. Exposure to 50 lithotripter shocks resulted in pits of about  $0.5 \text{ mm}$  width. On applying overpressure these pits gradually diminish in size and number and eventually disappear. The pits in figure 3.15c were of  $\sim 50 \mu\text{m}$  width when observed at 200X magnification.



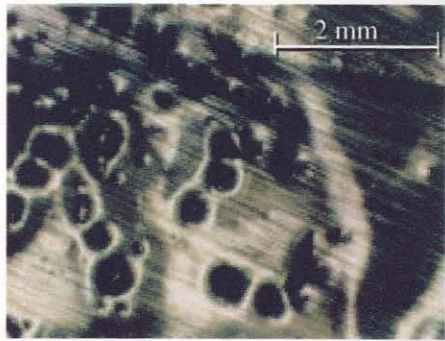
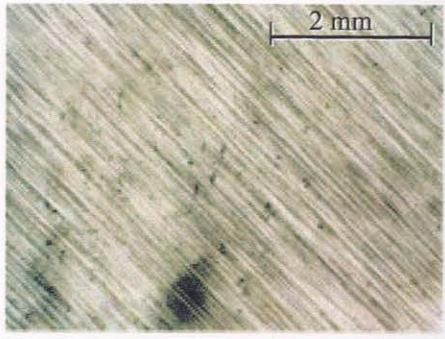
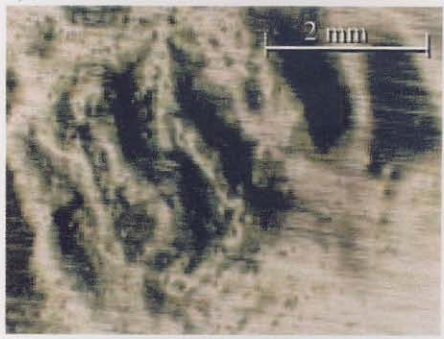


O/P (MPa)	Lithotripter wave	Refocused wave
0	a) 50 shocks @ 1 Hz, 18 kV 	
6	b) 50 shocks @ 1 Hz, 18 kV 	c) 50 shocks @ 1 Hz, 18 kV 
12	d) 100 shocks @ 1 Hz, 20 kV 	e) 100 shocks @ 1 Hz, 20 kV 

Figure 3.15: Comparison of aluminum foil damage/deformation patterns for various overpressures and wave-fields. a), b) and c) are photographs taken at 25X using a microscope. d) and e) are photographs from a digital camera. Cavitation pits ( $\sim 0.5$  mm wide) can be clearly seen in a), which get smaller in c) ( $\sim 50$   $\mu$ m wide) and are eliminated in b), d) and e). Wrinkling and denting deformation due to refocused wave can be seen in c) and e).

In contrast, foils subjected to the reflected wave-field of the parabolic reflector (figures 3.15c & e) showed other deformation features besides pitting. A *single* depression/dent with a wrinkled surface was observed, at an overpressure of 12 MPa. This dent was  $\sim 4$  mm wide, which corresponds to the 6 dB region of the refocused wave (5 mm - refer table 3.2). The wrinkling deformation could be described as a series of adjacent peaks and troughs on the foil observed over the dented area. No such denting and wrinkling deformation was seen for foils exposed to the lithotripter wave-field alone, either at atmospheric or at elevated pressures. Hence these deformation features of aluminum foils were due to the refocused wave-field from the parabolic reflector and not due to bubble collapse.



Figure 3.16: Cellophane film subjected to 50 lithotripter shocks @ 18 kV, 1 Hz. Damage comprises of holes and tears.

Cellophane film targets subjected to lithotripter shock waves under ambient conditions showed rounded holes, with cracks or 'tears' propagating from these holes (figure 3.16). These rounded holes can be attributed to bubble collapse akin to pitting damage on aluminum foils. On applying overpressure the number of holes as well as the number of tears diminished. At 10 MPa overpressure, a dose of 100 shocks reflected from the parabolic reflector yielded no damage to cellophane films. Films in which holes were introduced artificially (by a pin prick) also showed similar tears when exposed to shock waves at high overpressure (10 MPa). Thus, the tears are at-

tributed to shock wave propagation and cavitation-induced holes act as weak points at which subsequent shocks form tears. Eliminating cavitation also eliminates these tears implying that the cellophane is sufficiently strong to sustain shock waves, and tears occur only in the presence of weak spots caused by cavitation pitting. The threshold overpressure beyond which cavitation damage was eliminated, was lower for cellophane films than for aluminum foils. This is attributed to the lower surface roughness of the cellophane film (see section 2.4).

In summary, cavitation damage to foils is also a function of the surface roughness in addition to the incident waveform and the overpressure applied to the target. Also the nature of deformation/damage due to the shock was different (denting vs. tears), which is attributed to the difference in mechanical (elastic/plastic) properties of the cellophane film vis-a-vis aluminum foil.

### 3.5 Cell lysis results

Cell lysis experiments were conducted with the vials at  $> 12$  MPa overpressure. As shown here, an overpressure of 5.5 MPa was needed to eliminate all bubble activity. Foil damage was suppressed at pressures  $> 12$  MPa. It has also been shown that cell lysis is dramatically reduced, but is not eliminated at these overpressures which preclude cavitation [75]. In those experiments, using the same overpressure chamber [64], cells contained in rigid polypropylene vials were exposed to half the number of shock waves (75) as in the present study; shock wave induced cell lysis at high pressure was  $1.03 \pm 0.09\%$  compared to  $0.53 \pm 0.02\%$  for untreated controls. In the present study, also at overpressure to preclude cavitation, lysis with the parabolic reflector ( $4.2 \pm 0.4\%$ ) was approximately four-fold higher, and lysis with the flat reflector ( $2.4 \pm 0.4\%$ ) was about twice that of untreated controls ( $1.2 \pm 0.2\%$ ). Thus, shock wave induced cell lysis was significantly enhanced by the reflected wave field.

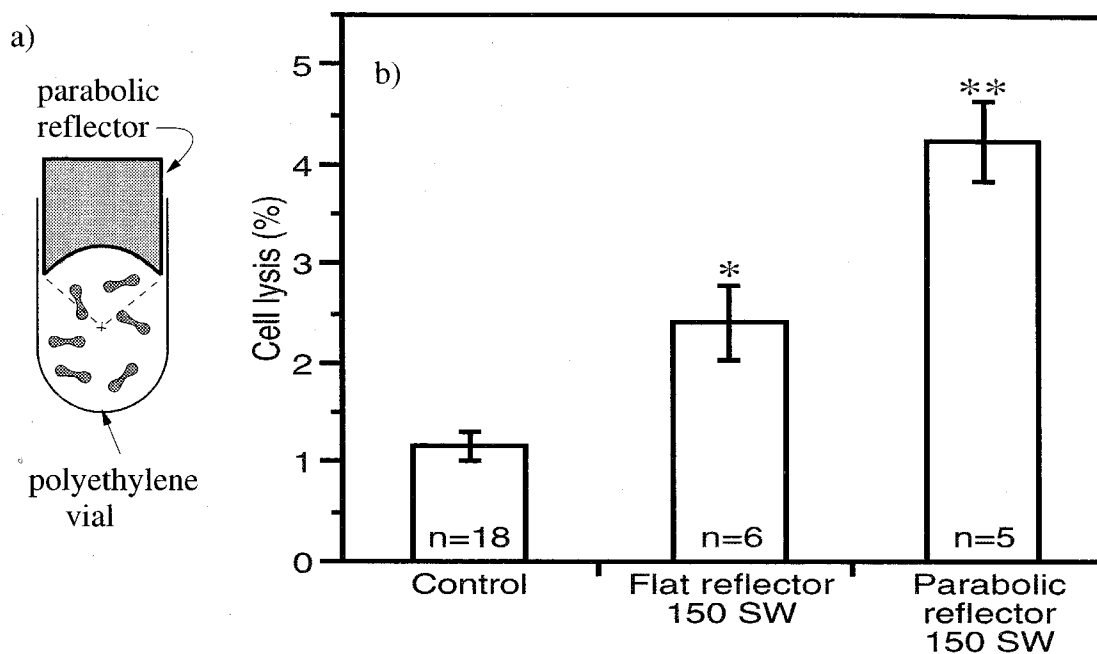


Figure 3.17: a) Schematic of parabolic reflector inserted into polyethylene vial containing suspension of RBC's (cells drawn larger than scale). b) Lysis of RBC's in suspension, in the presence of either the flat or parabolic reflector. 'Control' includes groups controlling for handling and pressurization effects (which were not significant) and received no shock waves. Shock waves were administered at 20 kV and 1 Hz.  $n$  indicates number of trials for each case. \*Different from control and parabolic,  $p < 0.01$ ; \*\*different from control,  $p < 0.001$ .

## Chapter 4 Analysis of cell deformation

In this chapter the RBC deformation and membrane tension due to shock-induced and bubble-induced flow-fields are analyzed.

### 4.1 Kinematic decomposition of fluid flow-field

In order to evaluate membrane tension, induced by a fluid flow-field, it is necessary to decompose a complex flow-field into more elementary forms, as illustrated in figure 4.1. The shock wave induces a shear flow, due to the velocity gradient along the shock front, and a radial flow due to curvature of the wavefront. The shear flow can be decomposed into a uniform translational flow and a “pure shear” component. The “pure shear” component is further comprised of a rigid body rotation and an extensional flow component. Radial motion due to symmetrical bubble expansion/implosion is decomposed into a uniform translational flow and an extensional flow component. Asymmetrical bubble expansion/implosion will also cause a jet-like flow, equivalent to a shear flow. Thus the flow-field due to both the mechanisms can be decomposed into a translational flow, a rigid body rotation and an extensional flow. This decomposition of flow-field is called Cauchy-Stokes decomposition theorem: *an arbitrary instantaneous state of motion may be resolved at each point into a uniform translation, a dilatation along three mutually perpendicular axes, and a rigid rotation of these axes* ([70], [1]).

Only the extensional flow causes deformation of an elementary fluid particle. The other two components instead tend to displace and rotate the fluid particle without any deformation. The same holds true for cells suspended in the fluid medium, that is, only the extensional flow-field tends to deform the cells. The underlying theme of this work is that two apparently distinct mechanisms of hemolysis, shock-induced and bubble-induced are actually identical inasmuch as their mechanistic effects are

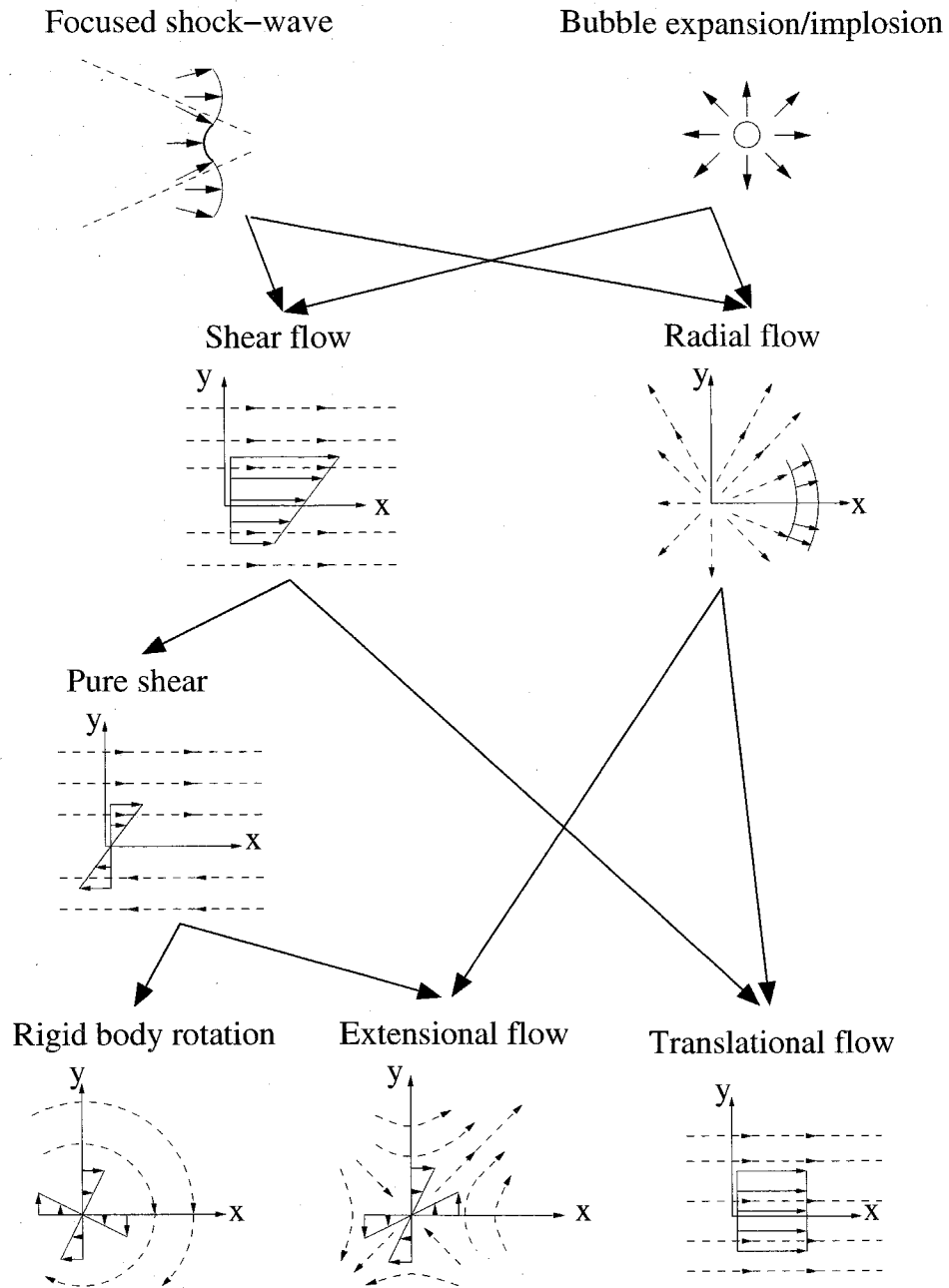


Figure 4.1: Kinematics of flow induced by focused shock wave and bubble motion. Solid arrows are velocity profiles and dashed arrows are streamlines for each flow field.



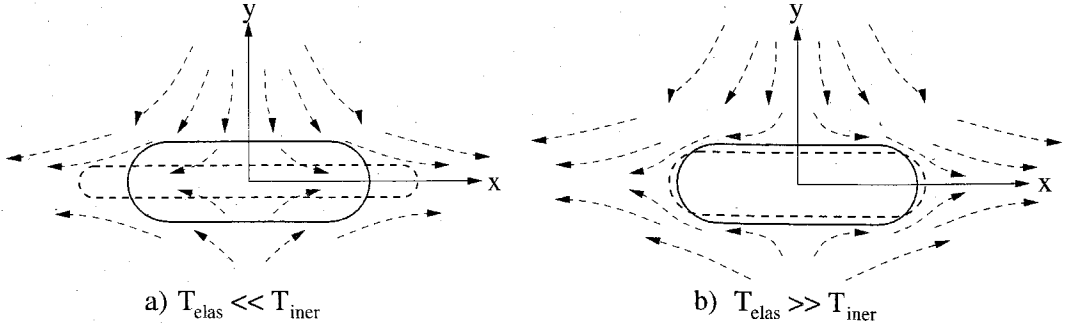


Figure 4.2: Cell deformation due to extensional flow. Dashed arrows indicate streamlines. a) Inertial mode of deformation. b) Viscous mode of deformation.

concerned. That is, both flow-fields constitute of a sufficiently strong extensional flow-field, inducing a membrane tension greater than  $T_c$ , causing lysis. Derivations for the above decompositions have been included in appendix B, for ready reference. According to the above hypothesis, the shock wave by itself does not cause cell lysis, rather it is the flow ensuing the shock which is responsible for cell membrane deformation, and concomitant lysis. Thus, if the shock-front is plane and of uniform strength, then the flow ensuing this shock is a uniform translational flow, causing no lysis.

## 4.2 Cell deformation

The problem at hand is to describe the interaction between an extensional flow and the cell. The forces acting on the cell wall are due to inertia of the fluid particles ( $T_{iner}$ ), and viscous stresses ( $T_{visc}$ ), causing it to deform. The quantity,  $T_{iner}$ , is a measure of the fluid inertia, expressed as a tension.  $T_{visc}$  is the membrane tension due to tangential viscous stresses, exerted by the fluid, on the cell wall. Deformation of the membrane due to the extensional flow induces an elastic tension,  $T_{elas}$ , which opposes the above forces exerted by the flow-field. At any given instance there exists a balance between  $T_{elas}$  and either one or both of the above mentioned forces. Based on the relative strengths of these forces, we can classify this interaction into two limiting cases (as shown in figure 4.2), denoted as inertial and viscous modes of deformation:

- *Inertial mode* ( $T_{elas} \ll T_{iner}$ ): The cell membrane is very *weak* as compared to the inertial forces, and hence deformation is described by flow kinematics, as shown in figure 4.2a. The presence of the membrane only perturbs the flow in its vicinity. As long as  $T_{elas} \ll T_{iner}$  a steady-state deformation of the cell cannot be attained, and the cell continues to deform, identical to deformation of fluid particles in absence of the membrane. As a consequence, there are negligible viscous stresses on the cell membrane, i.e.,  $T_{visc} \approx 0$ .
- *Viscous mode* ( $T_{elas} \gg T_{iner}$ ): The cell membrane is *strong* as compared to the inertial forces, and hence membrane deformation cannot be described by flow kinematics. The flow-field is still extensional in the far-field, but at the cell wall it has to conform to the no-slip boundary conditions. Figure 4.2b depicts this scenario. Thus, tangential viscous stresses are exerted on the cell wall, which will be in equilibrium with the membrane tension,  $T_{elas} \sim T_{visc}$ . In this case a steady-state deformation of the cell could exist, provided the membrane elastic stress does not exceed the threshold value, i.e.,  $T_{elas} < T_c$ .

In the next section, the mechanical properties of lipid membranes and the mechanics of pore formation in membranes is briefly reviewed, since it forms the basis of the membrane rupture hypothesis. The inertial and viscous forces are estimated in sections 4.4 and 4.5, respectively. In an unsteady flow-field, the relative magnitudes of the inertial and viscous forces, compared to the elastic membrane tension, can change with time. In such a situation the interaction could change from the inertial mode to the viscous mode, or vice-versa, as the flow evolves. The transition from inertial mode to viscous mode, is discussed in section 4.6. The analysis culminates in section 4.7 with a calculation of the membrane tension due to unsteady extensional flow produced by a focused shock wave and by radial bubble expansion.



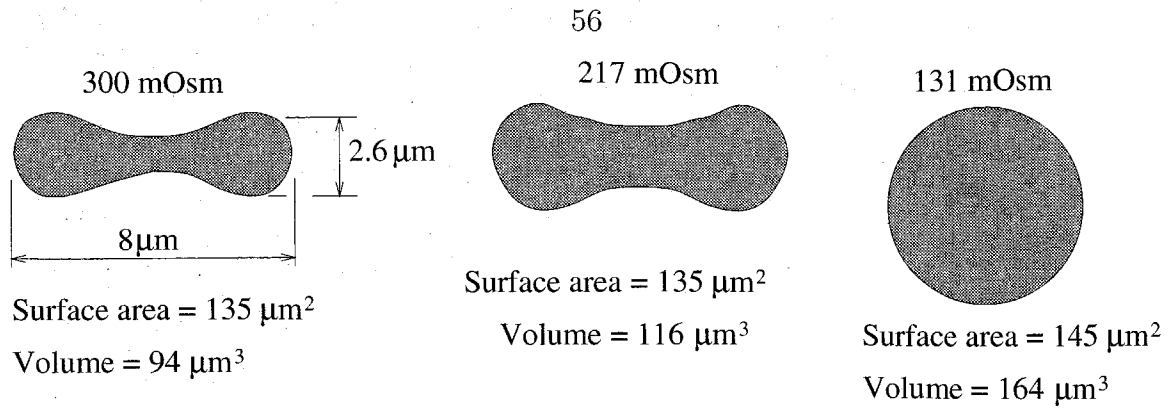


Figure 4.3: Osmotic lysis.

### 4.3 Membrane properties

For purpose of this analysis, the RBC is structurally equivalent to a fluid-filled capsule, with a cell membrane separating the cell contents from its exterior. The cell shape is a biconcave disc, with the disc diameter being  $8\mu\text{m}$  and the disc thickness varying from  $1\mu\text{m}$  at the center to  $2.6\mu\text{m}$  at the periphery. The RBC membrane is 5 – 10 nm thick, as obtained from electron microscope measurements. The membrane, which forms the enclosure, consists almost entirely of lipids and proteins. Proteins are either embedded in the lipid bilayer, known as integral proteins, or they form a network lining the endoface, parallel to the membrane, known as skeletal proteins. Though the protein network is relatively sparse as compared to the surface area of the cell, they have a direct contribution to the strength of the membrane and hence indirectly influence pore formation in the lipid bilayer, which results in cell lysis.

Mechanical properties of RBC membrane have been investigated in detail in the past. A simple experiment that shows membrane characteristics is osmotic swelling and subsequent lysis of cells. The disc-sphere transformation was first reported by Hamburger in 1895 and since then has been studied extensively (refer [51], for review of earlier work). Figure 4.3 shows the cell shapes, at three different osmolarities (salt concentration), enroute to cell lysis [23]. At 300 mOsm, the osmotic pressures exerted by the cell interior and the solution are identical, and hence the cell retains its shape. As the osmolarity of the solution decreases, the cell swells, forming into a sphere

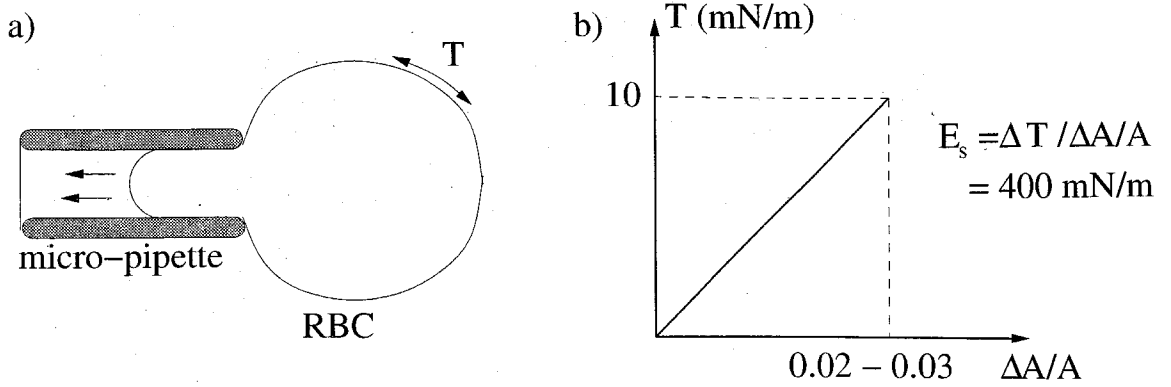


Figure 4.4: a) Micro-pipette aspirator, b) Linear  $T$  vs  $\Delta A/A$  relation.

at 131 mOsm, and eventually ruptures. It should be noted that the cell volume increases significantly during this process (75%), whereas its area remains almost constant (increases by 7%). A hypothesis first proposed by Rand [54, 55], that pores appear in the cell wall when the membrane surface area exceeds a threshold value, has found general acceptance in the literature.

More controlled experiments, on a single cell [24, 46], are performed using a micro-pipette aspirating system in conjunction with an optical processing system (refer to figure 4.4). Applying a suction pressure in the micro-pipette causes an increase in the length of the aspirated part of the cell and a reduction in the cell radius, which is a consequence of the cell volume remaining approximately constant. These dimensions are measured at a given pressure in the aspirator. The tension,  $T$ , in the cell wall is calculated from the pressure difference across it, and the radius of the cell. Areal strain ( $\Delta A/A$ ) is obtained from the length of the cell projection in the pipette (see [24] for details of this calculation). Measurements indicate a linear relation between the membrane tension and the areal strain. The lipid bilayer is treated as a continuum in two dimensions, and is characterized by its surface elasticity modulus ( $E_s = dT/(dA/A)$ ), the critical values of tension ( $T_c$ ), and the areal strain ( $(\Delta A/A)_c$ ) for which failure occurs. These properties are analogous to those of three-dimensional solids: the surface elasticity modulus is analogous to bulk modulus, and the critical tension and areal strain are analogous to the ultimate stress and strain at failure.

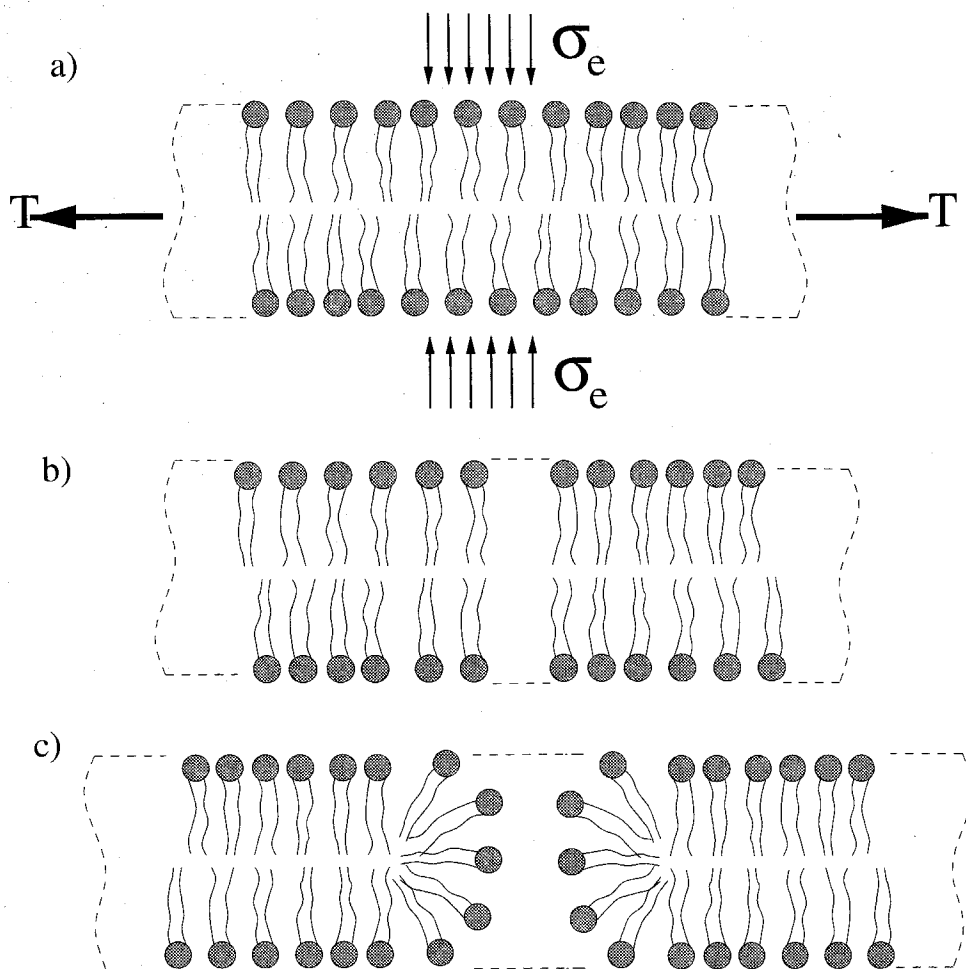


Figure 4.5: Membrane instability. a) Membrane stress state, b) Hydrophobic pore, c) Hydrophilic pore.

These refined experiments indicate an even smaller threshold for critical areal strain ( $2 - 3\%$ ), a critical tension,  $T_c$ , of  $10 \text{ mN/m}$ , and surface elasticity modulus  $\sim 400 \text{ mN/m}$ . These membrane properties will be used in subsequent calculations. While studying membrane deformation, it is typical to measure the tension (which has units of force/length or stress  $\times$  membrane thickness) rather than the stress (force/area = tension/membrane thickness) itself. This is because variations in membrane thickness will be negligibly small ( $\sim (\Delta A/A)_c$ ), and measurement of the membrane thickness under tension is difficult. In what follows, the words tension and stress are thus used interchangeably (though it always refers to tension (force/length)).

Besides the micro-pipette aspirator, another commonly used apparatus, for mea-

suring cell membrane properties, is a cone-plate or the Couette flow viscometer. Fluid shear stress, measured by this apparatus, is correlated with membrane tension. The critical membrane tension at rupture is thus obtained from a threshold shear stress, measured by the viscometer. These measurements compare well with the aspirator measurements, in certain flow regimes of the viscometer (for a review of measurement of membrane properties, refer to [5]). Uncontrolled effects of flow transients, roughness of the viscometer wall and exposure time, complicate the task of interpreting these results and comparing the two techniques. Besides laminar flow, experiments have also been reported in which a turbulent jet issues into a RBC suspending medium [25]. In these studies the turbulent shear stress is correlated with membrane strength. As mentioned in the introduction, a flow which has no shearing motion can also cause the cells to deform (see figure 4.1) and lyse. Thus membrane properties cannot always be correlated with shear stresses in the fluid. In this work, results from the micro-pipette aspirator experiments are considered as a base for comparison, since calculation of membrane tension under static forces is straightforward.

Another important mechanical property of the membrane is its bending rigidity, which is a measure of the resistance offered by the membrane to changes in its curvature. It is well known from the theory of shells and plates that bending rigidity is proportional to modulus of elasticity, and the third power of shell thickness. Hence, for thin shells, this rigidity is several orders smaller than the numerical value of the elasticity modulus. Thus, a membrane offers very little resistance to 'flexing', or deformations involving change in curvature, and stiffly resists areal strains (see [26] for a detailed discussion). This attribute of high flexibility enables the RBC to navigate the tortuous network of blood vessels, which at times can have a smaller diameter than the cell.

The formation of pores in the lipid bilayer, under the action of an isotropic tension, has been explained as an electro-mechanical instability of the membrane. This instability is related to the amphiphilic nature of the lipid molecules, and their bilayer configuration. The lipid macro-molecule consists of a water-soluble (hydrophilic), polar head-group of molecules, and an insoluble (hydrophobic) non-polar hydrocar-

bon tail. In the bilayer configuration, the hydrophilic head-groups face the aqueous medium, and the hydrophobic tails face inward (towards each other). This stable arrangement minimizes the energy of the system. However, when the membrane is subjected to an isotropic tension, the molecules are drawn further apart. The tail of the lipid molecule is exposed to the aqueous medium and forms a hydrophobic pore (figure 4.5b). Such a hydrophobic pore can also be caused by thermal fluctuations of the molecules. Since the hydrophobic pore is unstable, the molecules reorient themselves to form a hydrophilic pore, as illustrated in figure 4.5c [39].

The above membrane instability, in the presence of tension, can be understood by examining the energy of the pored state. The edge of the pore results in an energy increment of  $2\pi r_p \Gamma$ , where  $r_p$  is the pore radius, and  $\Gamma$  is an edge energy associated with the exposure of the hydrocarbon tails to the aqueous medium. Pore formation causes a reduction in elastic energy by an amount  $\pi r_p^2 T$ . For all pore radii less than a critical pore radius ( $\Gamma/T$ ), the pore will heal itself since this tends to reduce the energy. Pores larger than the above critical radius, by contrast, will grow unstably and combine with adjacent pores. For RBC membrane, pores of 1 – 10 nm are estimated [39] to be unstable. These pore sizes give an areal strain of  $(\Delta A/A)_p \sim 10^{-7} - 10^{-5}$ , which is several orders smaller than the experimentally measured critical strain ( $\sim 10^{-2}$ ). This discrepancy is explained by the fact that the probability of a pore growing unstably increases with time, membrane tension  $T$  (or the corresponding membrane strain  $\Delta A/A$ ), and temperature, for a membrane of given composition. For strains of the  $\mathcal{O}(\Delta A/A)_c$ , the probability that the membrane ruptures is close to unity, and is readily observed, whereas for strains  $\mathcal{O}(\Delta A/A)_p$ , this probability is negligibly small and hence not observed. Numerical simulations described in the literature (e.g., [63]) investigate the effect of the membrane parameters on unstable pore formation.

Pore formation and membrane permeabilization due to the application of an electric field is termed electroporation. Instead of the mechanically applied tension, an electric field applied across the membrane induces a compressive stress ( $\sigma_e$ ) across the membrane thickness, and results in a similar instability (termed electro-mechanical

instability [46]) to that described above. Current understanding about pore formation in cell membranes stems largely from electroporation experiments (see [73], for review on electroporation theory). In these experiments, application of a short duration electric field across the membrane, causes an increased transport of molecules across the membrane [47], if it exceeds a certain threshold. Cell lysis is also observed following the application of electric field. Cell lysis can occur either due to rupture of the membrane, i.e., unstable pore formation, or due to significant molecular transport between the intra- and extra-cellular environments, which leads to a chemical imbalance from which the cell is unable to recover. Thus, depending upon the electric-field parameters and the membrane characteristics, the membrane is either transiently permeabilized or irreversibly ruptured. By analogy, deformation of cell membrane induced by a fluid flow-field also results in an increased transport across the cell membrane or cell lysis, depending on the flow parameters.

## 4.4 Inertial forces

As explained in section 4.1, and illustrated in figure 4.2a, in the *inertial mode* ( $T_{elas} \ll T_{iner}$ ) membrane deformation is identical to that of an elementary fluid particle. The velocity potential,  $\phi(t)$ , for such a flow field, is given by

$$\phi(t) = k(t) \left( \frac{r^2}{2} - z^2 \right). \quad (4.1)$$

Equation (4.1) can be obtained from (B.12) in appendix B, by neglecting terms of  $\mathcal{O}(z^3, zr^2)$ , reverting to the dimensional form, and denoting  $u_R(t)/R$  as  $k(t)$ . The parameter  $k(t)$  is a kinematic property of the flow-field, and is a measure of the rate of deformation of the flow (see appendix B for a rigorous definition). For a shear flow  $k(t) = \frac{\partial u_x}{\partial y}$ . In this analysis, a coordinate system fixed with reference to the cell, is adopted. The parameter  $k$  will vary at different locations in the flow-field, i.e.,  $k = k(r, z, \phi, t)$ , however, we adopt a Lagrangian description for this quantity, i.e.,  $k = k(\chi, t)$ , where  $\chi$  is a label for a Lagrangian fluid particle, which is identical to the

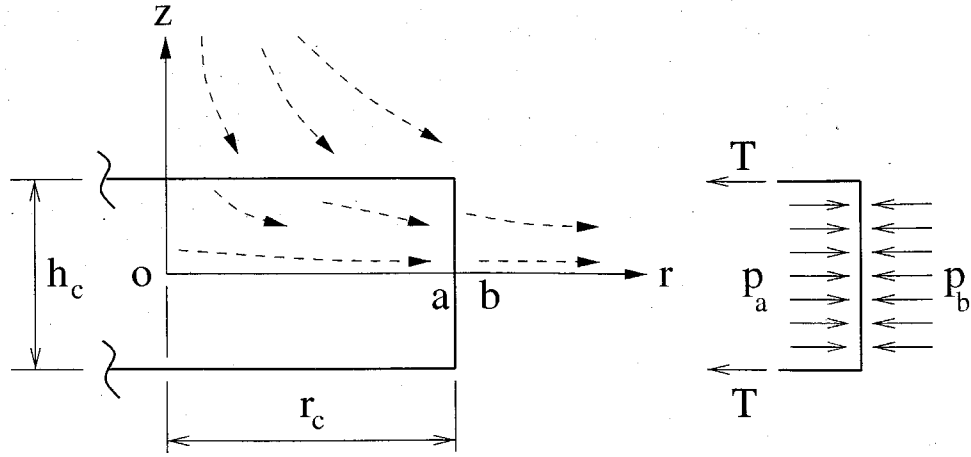


Figure 4.6: Cell deformation due to inertial force. Cell membrane is indicated by thick lines, and the cell is assumed to be disc-shaped. Dashed arrows indicate streamline pattern.

cell. Hence for any given cell,  $k$  depends only on time, as the cell assumes the motion of the fluid particle. Bernoulli's equation for unsteady, incompressible, potential flow, is

$$\frac{\partial \phi}{\partial t} + \frac{(\nabla \phi)^2}{2} + \frac{p}{\rho} = \text{constant}. \quad (4.2)$$

In the above equation  $p$  and  $\rho$  are pressure and density respectively, and gravitational potential is ignored. Substituting (4.1) in (4.2), we get

$$\dot{k}(t) \left( \frac{r^2}{2} - z^2 \right) + \frac{k^2(t)}{2} (r^2 + 4z^2) + \frac{p}{\rho} = \text{constant}. \quad (4.3)$$

Figure 4.6 shows the problem configuration, the disc-shaped cell deforming due to the unsteady extensional fluid flow-field. The potential,  $\phi$ , given by (4.1), is assumed to apply to the interior as well as exterior to the cell. This requires that the flow is minimally perturbed by the cell membrane. Also  $\rho$  is assumed to be identical for the fluid inside the cell (sp. gr. = 1.1), and the suspending medium. Depending on *in vivo/vitro* condition, this medium is either plasma (sp. gr. = 1.03), or saline solution (sp. gr.  $\approx 1$ ). Applying (4.3) to a radial streamline (refer figure 4.6), originating

from the origin (o) up to a point just interior of the cell (a), we get

$$\dot{k}(t) \frac{r_c^2}{2} + \frac{k^2(t)}{2} r_c^2 = \frac{p_o - p_a}{\rho} . \quad (4.4)$$

The quantity  $kr_c$  is a measure of the fluid velocity at the cell wall, in a cell-fixed reference frame. In (4.4), the left-hand side represents the inertial force of the fluid (temporal and convective acceleration of fluid), balanced by hydrodynamic pressure on the right hand. In the absence of the cell membrane, the hydrodynamic pressure is continuous at all points in the flow-field, and hence  $p_a = p_b$  (refer figure 4.6), for adjacent points a and b. However, with a membrane, the extensional flow causes the membrane to deform, inducing a tension in it, which requires a pressure differential to exist across the membrane, in order to balance this elastic tension. This balance is given by

$$T_{elas} = (p_a - p_b)h_c \approx (p_a - p_b)r_c , \quad (4.5)$$

where  $T_{elas}$  is the elastic tension in the membrane, and  $h_c$  is the width of the disc, which is approximated by a characteristic cell dimension,  $r_c$ . Using (4.5), equation (4.4) can be rewritten as

$$\frac{r_c^2}{2} (\dot{k}(t) + k^2(t)) = \frac{p_o - p_b}{\rho} - \frac{T_{elas}}{\rho r_c} . \quad (4.6)$$

Thus from (4.6), the inertial force of the fluid, expressed as a tension, is given by

$$T_{iner} \sim \rho r_c^3 (\dot{k}(t) + k^2(t)) . \quad (4.7)$$

The dependence of temporal and spatial acceleration terms on  $k(t)$  should be noted here. Since the temporal term is proportional to  $\dot{k} \sim k/\tau$ , where  $\tau$  is a timescale associated with the unsteady flow, and the spatial or convective term is proportional to  $k^2$ , the ratio of temporal to spatial acceleration is  $1/(\tau k)$  (note that  $k$  has the dimension of  $\text{time}^{-1}$ ). Thus, when the time scale of variation of the unsteady flow-field is smaller than  $1/k$ , ( $\tau \ll 1/k$ ), the unsteady inertial force will be predominant,



i.e.,

$$T_{iner} \sim \rho r_c^3 \dot{k}(t) \sim \rho r_c^3 \frac{k}{\tau} . \quad (4.8)$$

As will be seen in section 4.7, this is indeed the case, for the shock-induced extensional flow, for a very brief time duration.

The elastic tension,  $T_{elas}$ , actually induced in the membrane, is a function of the membrane deformation. Since the membrane deforms with the fluid, the radial displacement of a particle on the disc surface (refer figure 4.6) will be given by

$$\Delta r = \int_0^\tau u_{rR} dt = r \int_0^\tau k(t) dt , \quad (4.9)$$

where  $u_{rR}$  is the radial component of velocity (see appendix B for explanation of notation). Thus, for a disc of radius  $r_c$ , with thickness  $h_c < r_c$ , the areal strain is approximately given by

$$\Delta A/A \approx \Delta r_c/r_c = \int_0^\tau k(t) dt . \quad (4.10)$$

For an extensional flow which grows linearly from 0 to  $k$  in a time  $\tau$ , the areal strain is estimated as  $\sim k\tau$ . Consequently, the tension induced in the membrane,  $T_{elas}$ , will be  $\sim E_s k\tau$ . These estimates of areal strain and membrane tension hold only for inertial mode of deformation.

## 4.5 Viscous forces

In this section the viscous force ( $T_{visc}$ ), exerted on the cell membrane due to the unsteady extensional flow, is estimated. As explained in section 4.2, when the inertial forces are weak ( $T_{elas} \ll T_{iner}$ ), the membrane does not deform with the extensional flow-field, rather, the extensional flow-field has to obey the no-slip condition at the cell wall. Thus, a transient boundary layer,  $\delta_\omega$ , develops (refer figure 4.7), and a tangential stress,  $\tau_w$ , is exerted on the wall. This tangential stress induces a membrane tension.

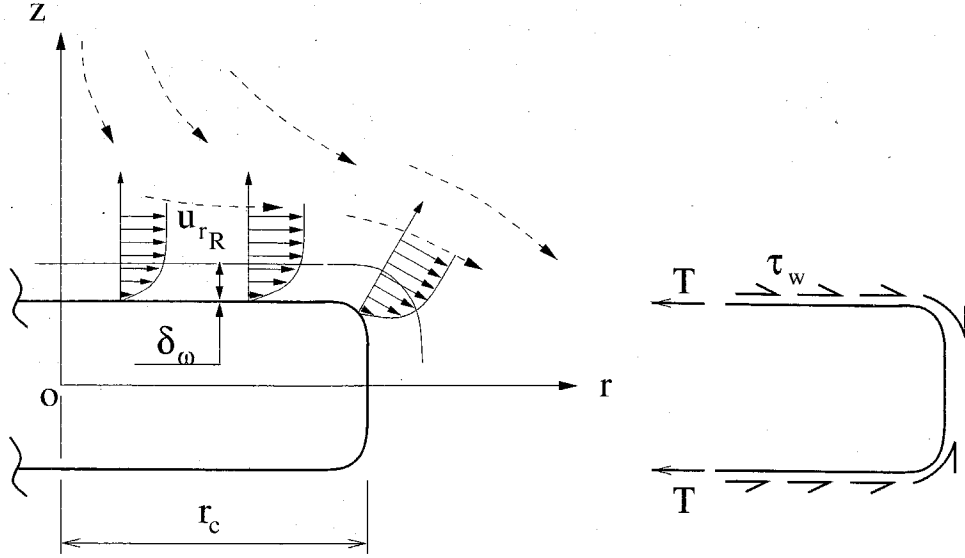


Figure 4.7: Cell deformation due to viscous force. Cell membrane is indicated by thick lines. Velocity profiles show boundary layer formation. Dashed arrows indicate streamline pattern for the far-field extensional flow,  $u_{rR}$  is the radial velocity tangential to the wall, determined from the far-field flow.

In appendix C expressions for  $\delta_w$  and  $\tau_w$  have been derived for Stokes' 1<sup>st</sup> problem, which deals with one-dimensional, unsteady flow. The problem at hand can be assumed to be one-dimensional if the boundary layer width,  $\delta_w$ , is smaller than the cell dimension,  $r_c$ . For the unsteady flow, the boundary layer width grows with time,  $\delta_w = \sqrt{\pi\nu t}$  (equation (C.6)), where  $\nu$  is the kinematic viscosity of the suspending medium. Hence the above problem can be treated as a one-dimensional unsteady flow, for  $t < r_c^2/(\pi\nu) \approx 6\mu\text{s}$ . For  $t > 6\mu\text{s}$  the boundary layer grows larger than the cell size, and the flow-field can be approximated as a quasi-steady Stokes' flow. RBC subjected to quasi-steady Stokes' flow has been dealt in several theoretical and computational works ([4, 36, 53] are a few notable ones). The motivation in these works is to calculate RBC deformation, and explain other features of RBC motion, for instance, *tank treading* motion of the cell membrane, as it commutes through the blood vessels.

Since the far-field flow is an extensional flow, the radial velocity is given by  $u_{rR} = k(t)r$ . This is identical to (B.9) if  $\mathcal{O}(r^2, z^2)$  terms are neglected. The definition of

$k(t)$  remains the same as in the previous section, i.e.,  $k(t) = u_R(t)/R$  for a radial flow,  $k(t) = \frac{\partial u_x}{\partial y}$  for a shear flow. When the above  $u_{r_R}$  is substituted in (C.10), we obtain

$$\tau_w(r, t) = \rho r \sqrt{\frac{\nu}{\pi}} \int_0^t \frac{dk(\tau)}{d\tau} \frac{1}{\sqrt{(t-\tau)}} d\tau. \quad (4.11)$$

Appendix D has a derivation for membrane force balance, in presence of a tangential wall stress. Substituting (4.11) in (D.4), we get

$$T_{visc}(r, t) = \rho \sqrt{\frac{\nu}{\pi}} \int_r^{r_c} r dr \int_0^t \frac{dk(\tau)}{d\tau} \frac{1}{\sqrt{(t-\tau)}} d\tau, \quad (4.12)$$

$$T_{visc}(0, t) = \frac{\rho r_c^2}{2} \sqrt{\frac{\nu}{\pi}} \int_0^t \frac{dk(\tau)}{d\tau} \frac{1}{\sqrt{(t-\tau)}} d\tau. \quad (4.13)$$

If  $k(t)$  grows linearly with time ( $= Kt$ ), then (C.11) or (C.16), in conjunction with (4.13), gives

$$T_{visc}(0, t) = \rho r_c^2 K \sqrt{\frac{\nu t}{\pi}} = \rho r_c^2 k(t) \sqrt{\frac{\nu}{\pi t}}. \quad (4.14)$$

Since the elastic tension in the membrane equilibrates with the viscous forces,  $T_{elas} \approx T_{visc}$ , and consequently membrane deformation is proportional to  $T_{visc}$ . Thus, critical deformation is reached when  $T_{visc} = T_c$ .

In contrast with the above estimate of wall tension, for a steady flow, wall tension due to viscous force is estimated as

$$T_{visc,st} \approx \tau_w r_c, \quad (4.15)$$

$$\approx \mu k r_c. \quad (4.16)$$

The steady flow assumes that the flow, characterized by  $k(t)$ , remains constant for a sufficient duration. The ratio,  $T_{visc,st}/T_{elas} \sim \mu k r_c / T_{elas}$ , is a counterpart of the capillary number ( $\mu k r_c / \gamma$ ), associated with bubbles suspended in a shear flow, with the elastic tension replacing the constant surface tension ( $\gamma$ ) in the denominator.

In table 4.1, calculations of this section and the preceeding section have been tabulated. In this table,  $T_{visc}$  is calculated assuming a linearly increasing  $k(t)$ , for a

	$T_{iner}$	$T_{visc}$	$T_{iner}/T_{visc} \sim Re$
Unsteady	$\rho r_c^3 k / \tau$	$\rho r_c^2 k (\nu / \tau)^{1/2}$	$r_c / (\nu \tau)^{1/2}$
Steady	$\rho r_c^3 k^2$	$\mu k r_c$	$(k r_c) r_c / \nu$
$T_{unst}/T_{st}$	$1/(k\tau)$	$r_c/(\nu\tau)^{1/2}$	

Table 4.1: Summary table of viscous and inertial tensions, in steady and unsteady flow.

time period  $\tau$ . The ratio  $T_{iner}/T_{visc}$  gives the relevant Reynolds number of the flow, for both the cases, i.e., steady and unsteady. This ratio ( $Re$ ) determines the relative strength of the two forces. The last row tabulates the ratio of unsteady forces to steady forces,  $T_{unst}/T_{st}$ , for the same extensional flow. This ratio can be seen to be proportional to the ratio of a steady timescale to an unsteady timescale (Strouhal number). Thus, if the flow remains steady for a time duration of the order of the steady timescale, then the steady calculations are valid. Conversely, if the flow varies at a timescale smaller than the steady timescale, then the unsteady calculations, presented in this work, are valid. For inertial effects, the steady timescale is  $1/k$ , whereas for viscous effects the steady timescale is  $r_c^2/\nu$ .

## 4.6 Transition from $T_{iner}$ to $T_{visc}$

In the previous two sections, while estimating the inertial and viscous forces, the magnitude of the inertial force relative to the elastic tension was assumed to be such that the deformation mode (inertial/viscous) does not change. However, since the flow is unsteady, the relative magnitude of  $T_{iner}$  can change with respect to  $T_{elas}$ , with time, causing a transition in the deformation mode as well. In this section a qualitative description of this transition is provided. Although, in the following paragraphs it is assumed that  $k$  increases linearly with time, this description of transition can be generalized to flow-fields which vary arbitrarily with time.

Figure 4.8a illustrates a sequence of possible deformation states for a monotonically increasing  $k$ . The distinct states in this sequence are numbered as follows: initial state is 0, lysed states are numbered as 1 or 2, and primed numbers (1', 2',

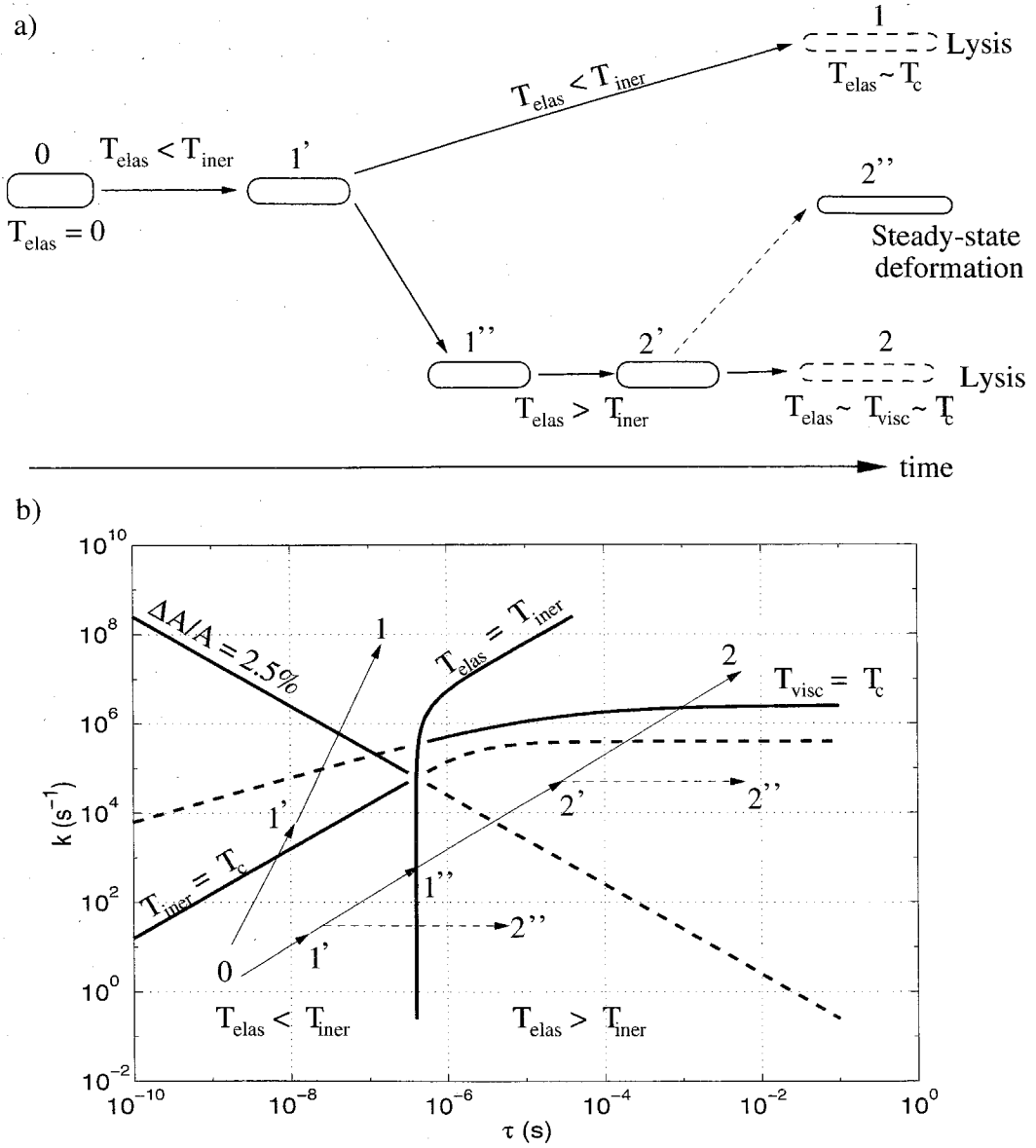


Figure 4.8: Cell deformation due to unsteady extensional flow. Deformation states of the cell are represented by numbers: 0, 1, 1', etc. a) Sequence of possible deformation states in an unsteady extensional flow. b) Sequence shown in a) represented on a  $k - \tau$  plane (see text for explanation).

1'', etc.) represent some intermediate state. In figure 4.8b the same sequence of deformation is plotted on a  $k - \tau$  plane. The line marked as  $T_{elas} = T_{iner}$  is a solution of the equation,  $\rho r_c^3 (k/\tau + k^2) = E_s k \tau$ , and demarcates the two modes of deformation, on the  $k - \tau$  diagram. The region left of the above line implies  $T_{elas} < T_{iner}$ , and hence an inertial mode of deformation. The region right of the above line will have  $T_{elas} > T_{iner}$ , and represents the viscous mode of deformation. Lines marked as  $T_{iner} = T_c$  and  $\Delta A/A = 2.5\%$  are solutions of the equations  $\rho r_c^3 (k/\tau + k^2) = 0.01$ , and,  $k\tau = 0.025$ , respectively. The line marked as  $T_{visc} = T_c$  is a solution of the equation,  $\rho r_c^2 k (\nu/\tau)^{1/2} + \rho \nu k r_c = 0.01$ . These lines are plotted bold in their respective regimes of validity, and dashed otherwise. For the lines  $T_{iner} = T_c$  and  $T_{visc} = T_c$ , the rising portions indicate the dominance of the unsteady contribution to the total force, whereas flat portions indicate the contribution of steady force (independent of  $\tau$ ). It should be noted here that only  $k$  and  $\tau$  are properties of the flow-field,  $r_c$ ,  $E_s$ ,  $T_c$  and  $(\Delta A/A)_c$ , are attributes of the RBC, and  $\rho$ ,  $\nu$  are physical properties of the fluid. Physical properties of water are used for plotting the above lines:  $\rho = 10^3$  kg/m<sup>3</sup>,  $\mu = \rho\nu = 10^{-3}$  Pa s.

For all unsteady flow situations, as in the case of ESWL, the membrane is initially undeformed, i.e.,  $T_{elas} = 0$ , and hence initial deformation will always be of inertial mode (0 - 1'). Two possible scenarios exist for subsequent deformation. One possibility is that the fluid inertia is strong enough to cause the cell to lyse (1' - 1), and viscous forces have no role to play. In the inertial mode, critical deformation is attained for state points above  $\Delta A/A = 2.5\%$  (e.g., 1). Alternatively, the membrane is stronger than the inertial forces, then the viscous forces determine the fate of the cell. The transition from inertial to viscous mode will occur gradually, in the vicinity of the line  $T_{elas} = T_{iner}$ . However, here it is assumed that the transition occurs instantaneously, across the above line (e.g., at state point 1''). State point 2' indicates a sub-critical deformation, in the viscous mode, whereas state point 2 indicates a critical deformation, sufficient for lysis. In the viscous mode, critical deformation is attained for state points above the line  $T_{visc} = T_c$  (e.g., 2). If  $k$  is maintained constant (instead of monotonously increasing) after attaining state points 1' or 2', then

a steady-state deformation of the cell ( $2''$ ) results. In subsequent calculations, the quantities  $T_{iner}$  and  $T_{visc}$  will be calculated without regard to this transition, since such a detailed calculation is beyond the scope of this work.

## 4.7 Application

In this section  $T_{iner}$  and  $T_{visc}$  for the shock-induced and bubble-induced flow are estimated, using results from the previous section. As can be seen from (4.13, 4.7) derived earlier, the quantity  $k(t)$ , characterizing the unsteady extensional flow, needs to be deduced for each of the flow situations, in order to compute the tensions and the deformations.

### 4.7.1 Shock-induced flow

Figure 4.9 illustrates the shock-RBC interaction. In figure 4.9a the length and timescales of this interaction are shown. For a shock strength of 40 MPa, the shock rise time, as obtained from Taylor's formula [69], is  $\sim 35$  ps. This translates into a shock thickness of  $\sim 50$  nm. The pressure rises steeply at the wavefront and eventually decays to the ambient conditions, in around  $2 \mu\text{s}$  ( $\sim 2.9$  mm), and then becomes negative for a duration of  $2 - 4 \mu\text{s}$ . In this work we will discuss the interaction with the positive wavefront only (extension to the negative portion can be done similarly). RBC dimensions shown in figure 4.9 have been discussed earlier, in section 4.3. The shock-RBC interaction can be differentiated into two time regimes (refer figure 4.9):

- a)  $0 < t < \tau$ . The time duration ( $\tau$ ) corresponds to the time required for the shock to propagate past a cell. Based on a cell width of  $2.6 \mu\text{m}$ ,  $\tau = 1.8$  ns. However, in general, the cell radius ( $r_c = 4 \mu\text{m}$ ) is a characteristic cell dimension, which gives  $\tau \sim r_c/c_o \approx 3$  ns ( $c_o = 1450$  m/s). As the wavefront propagates through the cell, it induces a flow-field in and around the cell. The extensional flow is not fully developed, but comes into existence at the end of this time duration. Hence the analysis presented in this work is not strictly valid in this

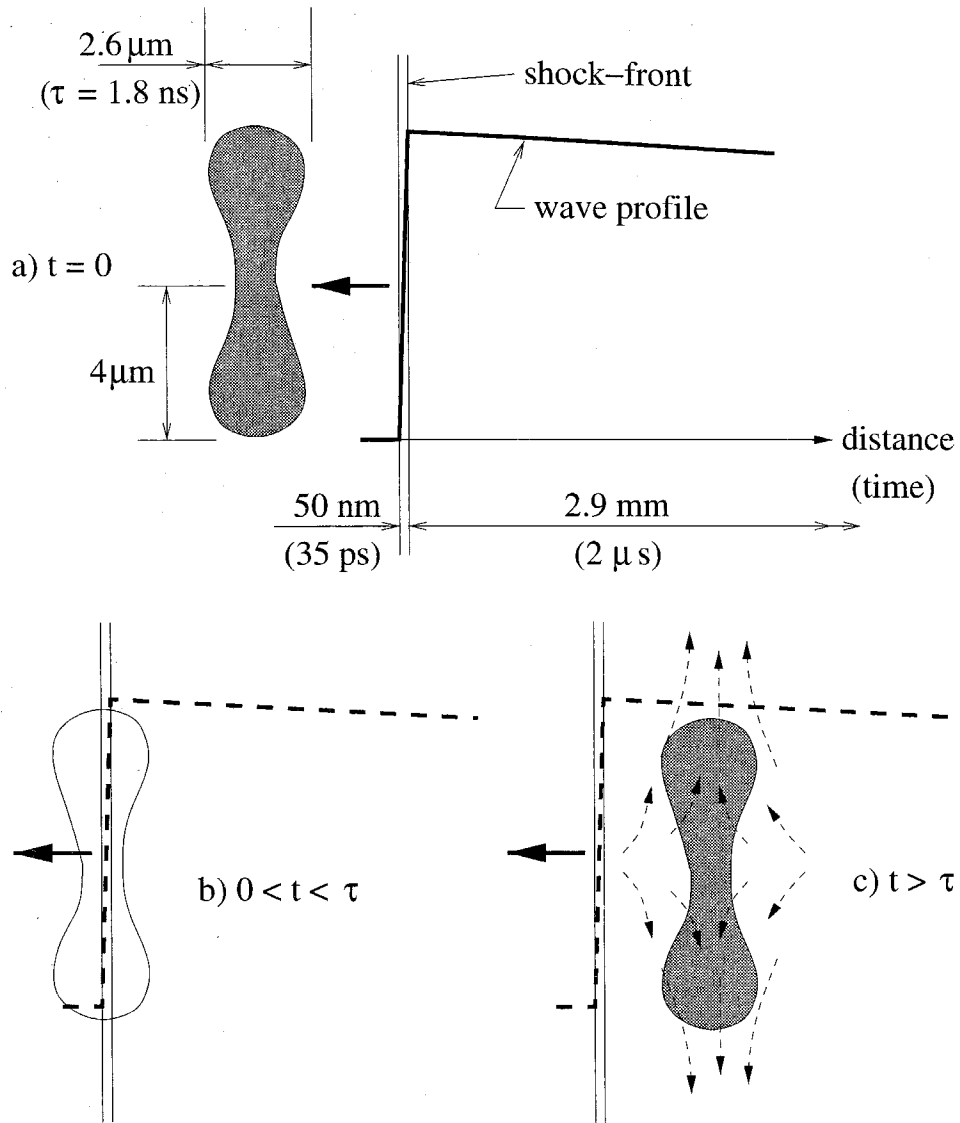


Figure 4.9: Illustrates the shock-RBC interaction, and the length(time) scales involved, drawn approximately to scale. Thick line indicates pressure (or velocity) profile of the wave. a)  $t = 0$ , before interaction, b)  $0 < t < \tau$ , c)  $t > \tau$ , decaying flow-field. Dashed arrows represent the extensional flow-field induced by the shock.



time regime, and the parameter  $k(t)$ , characterizing the extensional flow, has no meaning. However, we assume  $k(t)$  to grow linearly during this period to a maximum value, this maximum value being computed from measurements along the shockfront. Thus, the spatial gradient of the shock, along the direction of propagation, is approximated by a temporal variation in  $k(t)$ . It should be noted here that for situations where the shock rise time is greater than 3 ns the above assumption is not required and  $\tau$  should be replaced by the shock rise time in the following analysis.

- b)  $t > \tau$ . The extensional flow set-up by the shock wave during the earlier time regime decays in this time regime. Consequently, the tensions ( $T_{iner}$  and  $T_{visc}$ ) also decay.

As explained in section 4.1, the lithotripter-generated focused shock wave has a curved wavefront of varying shock strength. Both, the differential shock strength and the wavefront curvature, result in an extensional flow. The parameter  $k(t)$ , due to both these effects, is now estimated. In a uniform fluid, the peak positive pressure, which is a measure of shock strength, drops from 40 to 0 MPa within a distance of 1 cm (see section 3.2 and [12]). Thus, the fluid particle velocity associated with this pressure ( $u = \Delta P / \rho c = 26$  m/s) also has the same gradient. This gives us a maximum velocity gradient of,  $k_{max} = 26 / 0.01 \approx 3 \times 10^3$  s<sup>-1</sup>. Although this  $k_{max}$  is temporally a maximum quantity, spatially (over a beam-width of 2 cm) it is an average quantity. Since the shockfront is almost planar near the focus,  $k$  would have a spatial maximum away from the acoustic axis.

The curved shockfront induces a radial flow. Assuming that the shockfront is smooth (see [65, 66] for discussion on “kinks” in shockfront), this radius will be of the order of the beam-width, i.e., 2 cm. Thus, the quantity  $u_R / R$ , characterizing the radial flow is of the same order as the quantity  $k_{max}$  calculated above, for a shear flow. Hence in subsequent calculations, for shock-induced flows, the radial flow due to curvature of the focused shock will be disregarded, with a proviso that under conditions where shock curvature is significant its effect has to be accounted for. Thus

$k(t)$  is defined as:

$$k(t) = k_{max} \frac{t}{3 \times 10^{-9}}, \quad 0 \leq t \leq 3 \times 10^{-9}, \quad (4.17)$$

$$= k_{max} \left(1 - \frac{t - 3 \times 10^{-9}}{2 \times 10^{-6}}\right), \quad 3 \times 10^{-9} \leq t \leq 2 \times 10^{-6}, \quad (4.18)$$

$$= 0, \quad t \geq 2 \times 10^{-6}. \quad (4.19)$$

Figure 4.10a shows the velocity gradient,  $k(t)$ , defined in (4.17 – 4.19). Inertial and viscous tensions are calculated using (4.7) and (4.13), and plotted in figures 4.10b and 4.10c respectively (note the change in scale of abscissa, in figure 4.10, after  $3 \times 10^{-9}$  s). The maximum value of the tension, due to inertial force, is given by  $\rho r_c^3 k_{max} / \tau \approx 64$  mN/m. During the decay period of the wave, this tension attains a value 0.1 mN/m. Thus, the inertial force is strong enough to overcome the critical tension, but it lasts for a very brief time,  $\tau$ . The areal strain, induced during this period, is  $\Delta A / A \sim k_{max} \tau \sim 10^{-5}$ . Though the above strain is less than the critical areal strain of  $10^{-2}$  [24] needed for failure, it is sufficient for pores to form (see discussion in section 4.3). It should be noted here that the quantity  $k_{max} / \tau$ , which determines the magnitude of inertial stress, is dependent on the pressure gradient in the direction of the shock propagation (since  $\tau \sim$  shock rise time, for shock rise times  $> 3$  ns, and  $k_{max} \sim$  peak pressure/beam width). Hence a smaller shock rise time ( $\tau$ ) (i.e., steeper pressure front) would result in a higher  $T_{iner}$ , but at the same time the product  $k_{max} \tau$  reduces, lowering the areal strain.

The maximum viscous tension is given by  $\rho(\nu/\pi\tau)^{1/2} r_c^2 k_{max} \approx 0.5$  mN/m, where  $k_{max} \approx 3 \times 10^3 \text{ s}^{-1}$  and  $\tau \approx 3 \times 10^{-9}$  s, as explained above. The tension decays from the maximum value in time  $\sim \tau$ . This tension is always less than the critical membrane tension,  $T_c$ . As discussed in section 4.1, when  $T_{elas} \ll T_{iner}$ , the membrane deforms with the fluid, and there is negligible relative motion between the fluid and the membrane, i.e.,  $T_{visc} \approx 0$ . Thus, the above calculation of  $T_{visc}$  during the 3 ns time duration is an over-estimate, and does not hold. However, after  $T_{iner}$  has died out ( $t > 3$  ns), the viscous forces calculated here are valid. It should be noted that

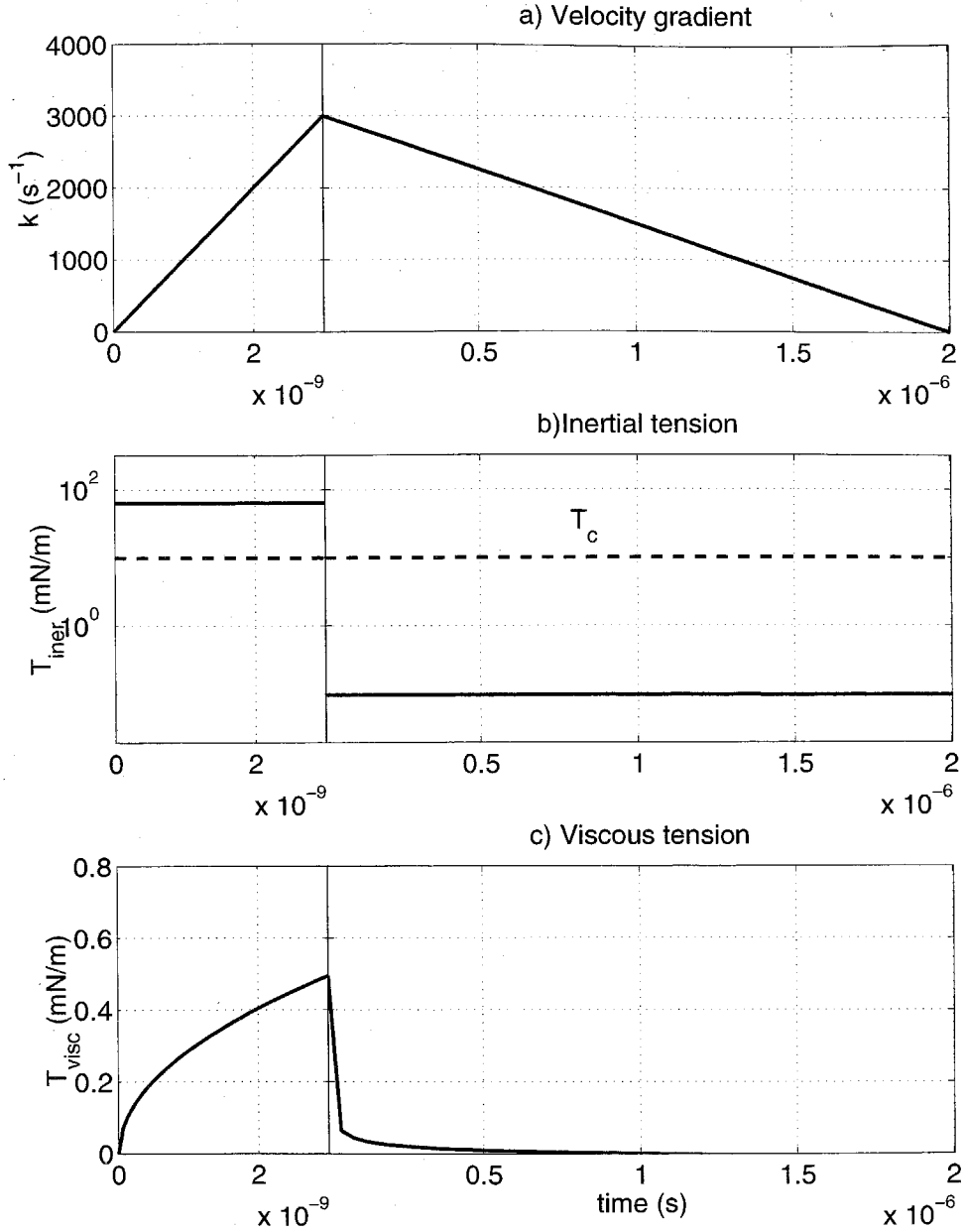


Figure 4.10: Membrane tension due to shock-induced shear flow. Note the change in scale of abscissa after  $3 \times 10^{-9}$  s. a) Velocity gradient as defined in (4.17). b) Tension due to inertial forces,  $T_{\text{iner}}$ , as given by (4.7). The ordinate has a log-scale. Dashed line indicates critical tension,  $T_c$ , for cell rupture. c) Tension due to viscous forces,  $T_{\text{visc}}$ , as given by (4.13).

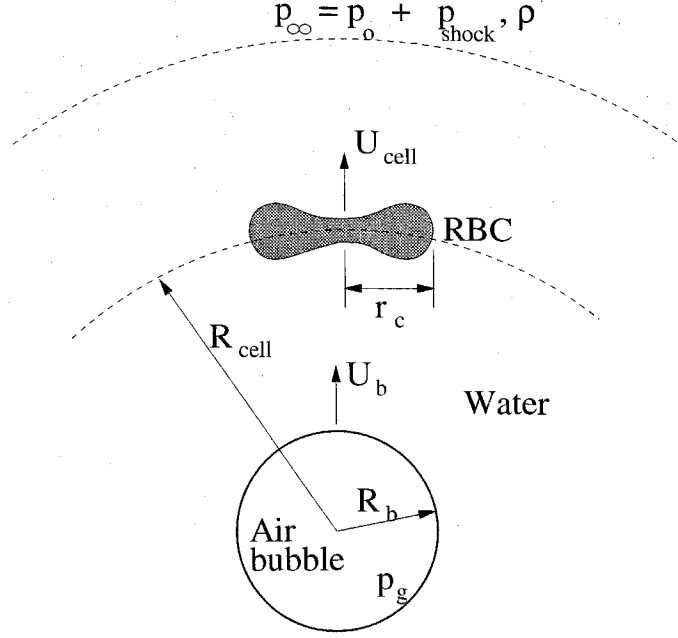


Figure 4.11: Model problem for bubble-RBC interaction.

the maximum viscous tension calculated here is two orders higher than that obtained from a steady flow calculation ( $T_{visc,st} \sim \mu k r_c \approx 10^{-2}$  mN/m).

#### 4.7.2 Bubble-induced flow

The parameter  $k(t)$ , and the corresponding membrane tension, for bubble-induced flow is calculated in this section. Rayleigh's model [56] is used for predicting the radial response of a single spherical bubble to a lithotripter pulse. The model problem is shown in figure 4.11. The equation of motion for bubble radius,  $R_b$ , is

$$\ddot{R}_b R_b + \frac{3}{2} \dot{R}_b^2 = \frac{1}{\rho} (p_g - p_\infty), \quad (4.20)$$

where  $p_g$  is the gas pressure inside the bubble,  $\rho$  is the density of liquid surrounding the bubble, and  $p_\infty (= p_0 + p_{shock})$  is the far-field pressure, which comprises of the ambient pressure ( $p_0$ ) and the shock pressure ( $p_{shock}$ ). The center of the RBC is located at a radius  $R_{cell}$ , from the bubble center. By definition (refer to section 4.4),  $k(t) = U_{cell}/R_{cell}$ , where  $U_{cell} = dR_{cell}/dt$  is the radial velocity of the cell center.

The quantities,  $R_{cell}$ ,  $U_{cell}$ , are related to the bubble radius and bubble wall velocity ( $U_b = dR_b/dt$ ) by

$$R_{cell}^3 - R_b^3 = R_{cell0}^3 - R_{b0}^3, \quad (4.21)$$

$$U_{cell} = U_b \left( \frac{R_b}{R_{cell}} \right)^2. \quad (4.22)$$

Equation (4.21) is from volume conservation of an incompressible fluid.  $R_{cell0}$  is the initial radial location of the cell and  $R_{b0}$  is the initial bubble radius. Equation (4.22) is obtained by differentiating (4.21). The gas inside the bubble is assumed to be air, obeying an isentropic law,  $p_g = p_0(R_{b0}/R_b)^{3\gamma}$  (where  $\gamma = 1.4$  is the ratio of the specific heats). The effects of surface tension and viscosity, which enter through a force balance across the bubble wall, have been neglected. The Gilmore-Akulichev formulation has been used by others [3, 11] for calculating bubble response to lithotripter acoustic fields, and a comparison of various bubble models can be found in literature [72]. The Gilmore-Akulichev formulation, which accounts for compressibility of the surrounding liquid, is supposed to be most accurate [72] for calculating violent bubble collapses. Since only the preceeding expansion phase of the bubble is considered here, and not the violent collapse phase, the accuracy of the Rayleigh model is considered to be sufficient.

Figure 4.12 shows the results of the calculations. The differential equation (4.20) is integrated numerically using an explicit Runge-Kutta (4,5) routine (ode45 in Matlab - MathWorks Inc., Natick, MA). A 5  $\mu\text{m}$  bubble is subjected to a tensile pulse of magnitude 5 MPa and duration 5  $\mu\text{s}$ . We ignore the positive pressure, present in an actual ESWL pulse, since it has a minimal effect on bubble growth which is due to the tensile portion only. As seen in figure 4.12b, the bubble wall continually accelerates for the duration of application of the negative pulse (5  $\mu\text{s}$ ), beyond which it starts to decelerate. Dashed lines in figure 4.12 indicate the radial location and velocity of a cell. The cell center is initially located 40  $\mu\text{m}$  from the bubble center ( $R_{cell0}$ ). This initial location is selected to satisfy the assumption,  $r_c/R_{cell0} \ll 1$ , which was made while linearizing the radial flow to an extensional flow (B). Membranes of cells

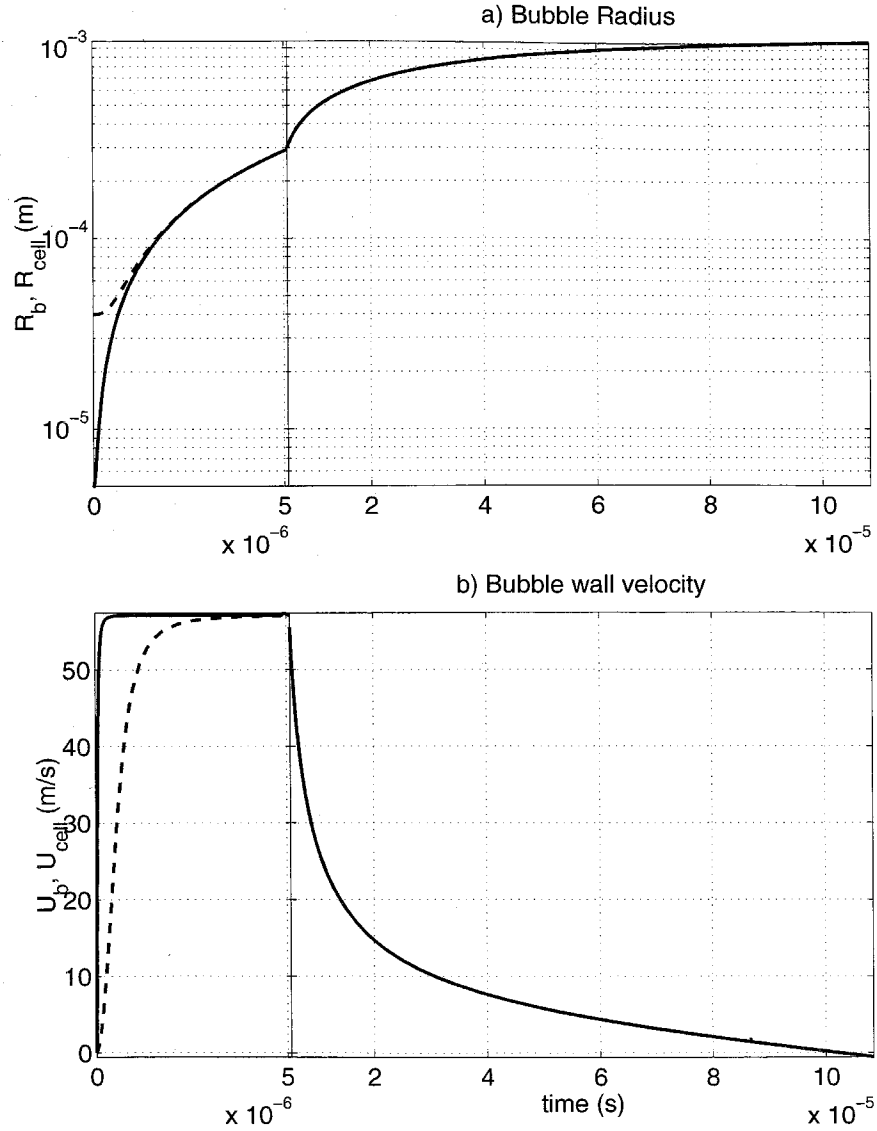


Figure 4.12: Response of a  $5 \mu\text{m}$  bubble from Rayleigh's model. Bubble subjected to a tensile pulse of  $5 \text{ MPa}$  for a duration of  $5 \mu\text{s}$ . Note change in scale of abscissa after  $5 \times 10^{-6} \text{ s}$ . a) Bubble radius ( $R_b$ ) (solid curve). Dashed curve corresponds to radial location of a cell ( $R_{cell}$ ), initially at  $40 \mu\text{m}$  from the bubble center. b) Bubble wall velocity ( $U_b$ ). Dashed curve corresponds to radial cell velocity ( $U_{cell}$ ).

closer to the bubble will be subjected to stronger forces than that calculated here, but these cannot be estimated accurately due to the approximations made here. As seen in figure 4.12a, the difference between the cell radial location ( $R_{cell}$ ) and the bubble radius ( $R_b$ ) can be seen for a very short time only ( $2 - 3 \mu s$ ). Similarly, the radial cell velocity,  $U_{cell}$ , differs from the bubble wall velocity for the first few  $\mu s$  only.

The parameter of interest,  $k(t)$ , which characterizes the extensional flow in the frame of reference of the cell, is plotted in figure 4.13a. It reaches a maximum ( $k_{max}$ ) of  $7 \times 10^5 \text{ s}^{-1}$  at  $\tau \approx 0.9 \mu s$ . This gives an inertial tension of  $100 \text{ mN/m}$  (seen from figure 4.13b). Using the estimates from table 4.1, the unsteady and steady inertial tensions can be calculated as  $64 \text{ mN/m}$  and  $31 \text{ mN/m}$ , respectively. Thus the bubble-induced flow exerts an inertial force of the same order as the shock-induced flow, both of them higher than the membrane critical tension (figure 4.10b). However, in this case, this force lasts for a duration of  $1 \mu s$ , causing an areal strain of  $\Delta A/A = k_{max}\tau \approx 1$  (or 100%), two orders higher than the required strain of  $2 - 3\%$ , for failure.

Viscous tension in the absence of inertial deformation is plotted in figure 4.13c, for the sake of completeness. As discussed for the shock-induced flow, the cell in this case will deform in accordance with the inertial forces, and there will be negligible relative motion between the cell and the extensional flow. Consequently,  $T_{visc} \approx 0$ , for the first  $1 \mu s$ , contrary to the plotted values.

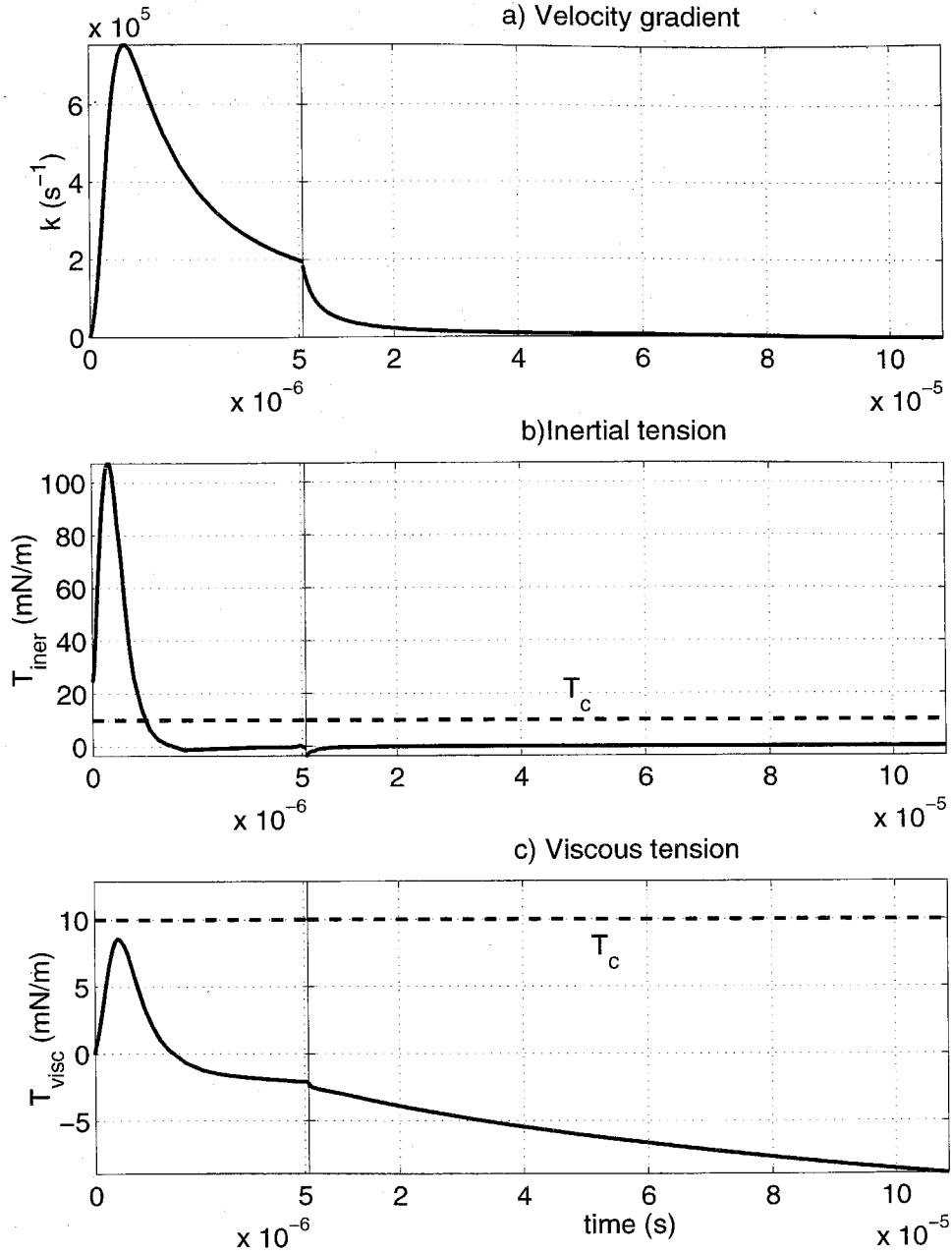


Figure 4.13: Membrane tension due to bubble-induced radial flow. Note the change in scale of abscissa after  $5 \times 10^{-6}$  s. a) Velocity gradient as defined in (4.17). b) Tension due to inertial forces,  $T_{\text{iner}}$ , as given by (4.7). Dashed line indicates critical tension,  $T_c$ , for cell rupture. c) Tension due to viscous forces,  $T_{\text{visc}}$ , as given by (4.13).



## Chapter 5 Discussion and conclusions

Tissue damage in SWL was experimentally and analytically investigated in this work. Earlier experiments have shown that *in vitro* exposure of RBC's to SWL shock waves, when suspended in either a cavitating or a non-cavitating environment, cause the cells to lyse. Although most studies of tissue damage in SWL have focused on cavitation as the damage mechanism (e.g., [16, 18]) cell lysis has also been observed due to lithotripter shock waves under conditions in which cavitation was prevented [75]. This damage was attributed to shear. The notion that shearing motion of fluid causes deformation of cells and subsequently causes them to lyse has been widely accepted in other applications and is also applicable to flow-fields induced by SWL shock waves [30]. Shear flow induces stress/strain in cell membranes and can result in irreversible leakage of cellular contents.

### 5.1 Analysis

The deformation of a cell due to an arbitrary flow-field is analyzed, and this analysis is applied to SWL flow-fields. The fluid motion is kinematically decomposed into extensional, translational, and rotational motions. Since only the extensional motion causes the cell to deform, that component must be large enough if the flow is to be lytically effective. In SWL, a focused shock wave, as well as radial flow, due to an expanding/imploding bubble, both comprise of an unsteady extensional flow, causing cells to deform.

The inertial and viscous forces exerted on the cell membrane by an unsteady extensional flow, are estimated. The rate-of-deformation parameter ( $k$ ), and the time-scale ( $\tau$ ) of the flow-field, are the important parameters, which govern the magnitudes of the inertial and viscous forces on the cell membrane. Figure 4.8b is reinterpreted in figure 5.1, and summarizes the analytical results. As explained in section 4.6, the

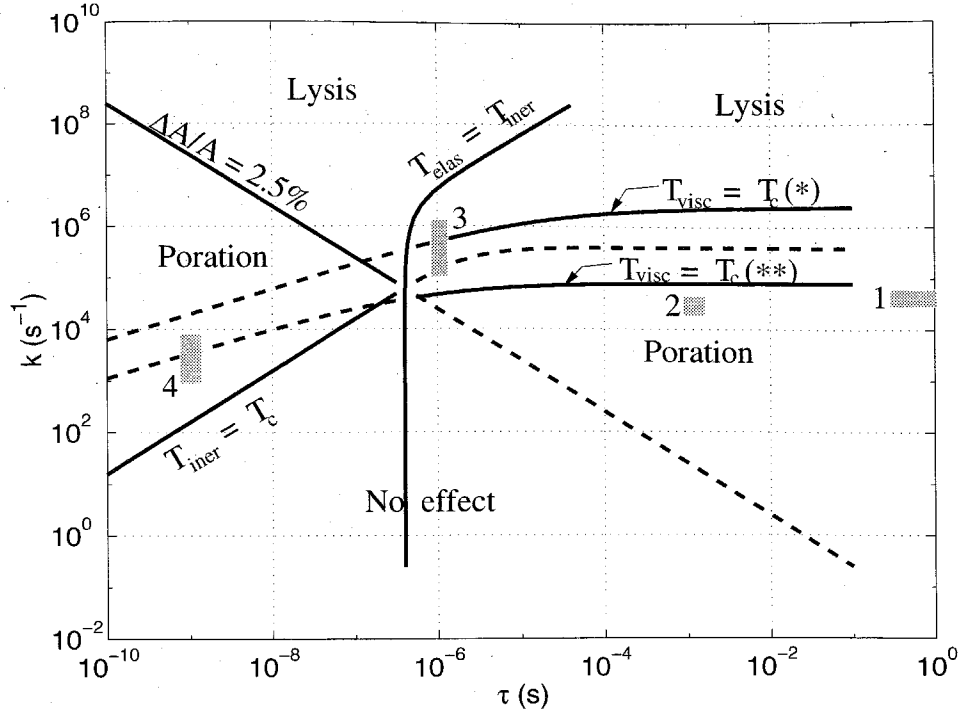


Figure 5.1: Cell deformation/lysis regimes on a  $k - \tau$  plot. Shaded areas (marked by numbers) represent operating regimes of various experimental setups, tabulated in table 5.1 (see corresponding number in table). \* water is the suspending fluid,  $\mu = 10^{-3}$  Pa s, \*\* suspending fluid has  $\mu = 31 \times 10^{-3}$  Pa s (from [58])

No.	Experiment	$k$ ( $s^{-1}$ )	$\tau$ (s)	Deformation/ lysis modes	References
1	Viscometer	$10^4 - 10^5$	1 – 10	Viscous	[35]
2	Single bubble	$10^4 - 10^5$	$10^{-3}$	Inertial/Viscous	[58]
3	Cavitation <sup>†</sup> (SWL)	$10^6$	$10^{-6}$	Inertial/Viscous	[18, 64]
4	Shock wave <sup>†</sup> (SWL)	$10^3 - 10^4$	$10^{-9}$	Inertial	[42, 75]

<sup>†</sup>  $k - \tau$  values are estimated in this work.

Table 5.1: Summary table of various experiments on RBC lysis, listing  $k - \tau$  parameter of their flow-fields, and deformation/lysis mode(s).

inertial/viscous modes of deformation are demarcated by the line  $T_{elas} = T_{iner}$ , on the  $k - \tau$  plane. Also, the deformation can be either sub-critical, i.e., a transient population of pores can arise in the membrane, or critical, i.e., the membrane can rupture

irreversibly, resulting in cell lysis. The solid portions of the lines  $\Delta A/A = 2.5\%$  and  $T_{visc} = T_c$  demarcate the regimes of sub-critical and critical cell deformation, on the  $k - \tau$  plane (figure 5.1), marked as ‘poration’ and ‘lysis’, respectively. Currently, there is no clear criterion to demarcate regions on the  $k - \tau$  plane which have a transient pore population from a region which has absolutely no pore formation. However, cell deformation is clearly reduced as we move farther away from the above lines (in the direction of reducing  $k$ ). Since the parameters  $k$  and  $\tau$  determine the lytic capabilities of a flow-field, in figure 5.1, representative  $k - \tau$  values for a range of experimental setups have been superposed on the above analytically determined cell deformation/lysis regimes. These experimental results are tabulated in table 5.1, and discussed briefly.

As discussed in section 4.3, viscometers have been more commonly used for measuring cell lysis. Typical values of  $k$  for viscometers (e.g., [35]) are  $10^4 - 10^5 \text{ s}^{-1}$ . These are represented by the shaded region marked 1, in figure 5.1. The parameter  $\tau$  (time taken by the viscometer to accelerate to the maximum speed) is usually  $\sim 1 - 10 \text{ s}$ , and hence the steady shearing effect dominates in this regime of operation. However, during this steady regime, the duration of exposure is important, because of visco-elastic deformation of the cell membrane [9, 29], and due to the statistical nature of the membrane rupture process, as discussed in section 4.3. Leverett has summarized in his work [35] a plot of threshold shear stress for lysis vs. duration of exposure, which would be identical to figure 5.1, for  $\tau \gg 10^{-6} \text{ s}$  (since  $k$  multiplied by viscosity yields shear stress, and  $\tau$  would mean duration of exposure). In figure 5.1, the shaded area marked 2 represents cell lysis experiments performed by Rooney [57, 58]. In Rooney’s experiment, a single bubble was set into translational motion, by an acoustic field, in a suspending fluid of viscosity  $0.031 \text{ Pa s}$ . A steady streaming motion is set up due to the bubble translational motion, which was explained to cause cell lysis.

Inertial tension due to bubble-induced radial flow-field, during its expansion phase, was calculated to be  $100 \text{ mN/m}$  (section 4.7). This force is much higher than the threshold membrane tensions measured in single cell experiments. Also, the calcula-

tions suggest a strain of  $\sim 100\%$ , which means that the surface area will be stretched to twice the original area, well beyond the critical strains measured in experiments. In figure 5.1, the calculated values of  $k$  and  $\tau$ , for bubble-induced radial motion, are marked 3. It should be noted that although 3 lies in the viscous deformation regime, it is located proximally to the transition line ( $T_{elas} = T_{iner}$ ), and hence cell deformation/lysis is due to inertial forces. In the above calculation the cell was assumed to lie at a particular radial distance from the bubble center ( $R_{cell0} = 40 \mu\text{m}$ ). Cells farther away from the bubble will be subjected to smaller magnitudes of forces and strains, and will consequently have a lower probability of failure. Hence in a region surrounding the bubble, cell lysis is readily explained in terms of the radial motion of the bubble set up by the tensile phase of the lithotripter pulse.

The inertial tension due to shock-induced flow-field was calculated to be  $64 \text{ mN/m}$ . Though this force is sufficient to deform the membrane, it lasts for a very short time,  $\sim 3 \text{ ns}$ . The strain induced by the inertial forces is  $\sim 10^{-5}$ , much lower than the critical strain,  $\sim 10^{-2}$ , needed to rupture the cells, but larger than that required to induce pores,  $\sim 10^{-7} - 10^{-5}$ , as described in section 4.3. Thus, the strain is sufficient to induce pores, but since it is much lower than the critical strain, the probability that these pores grow unstably and cause the membrane to rupture is very low, i.e., only a fraction of all the cells subjected to shock waves will be lysed. To estimate this fraction would require the analysis of membrane dynamics beyond the pore formation stage, which is beyond the scope of this work. The area marked 4 in figure 5.1 represents shock-induced flow parameters.

While calculating the shock-induced deformation, the effect of wavefront curvature was ignored. For finite amplitude focused waves, this is an important effect [65]. A finite amplitude converging wavefront is unstable, and forms sharp corners, or ‘kinks’, equivalent to Mach reflection. This formation of sharp corners has been observed experimentally [66], for conditions in which the wavefront geometry and strength (shock Mach number,  $M_s \sim 1.05$ ) are similar to that in lithotripsy. It was shown that, close to the focal region, non-linearity always causes the formation of a Mach stem, i.e., a sharp corner in the shockfront. The inherent variability of the lithotripter

acoustic field, which is due to the variability of the spark generation at the focus [12], makes it difficult to confirm the absence or presence of these sharp corners in the shockfront. However, the presence of these ‘kinks’ in the shockfront would suggest that the deformation parameter ( $k(t)$ ) is several orders higher, leading to higher lytic effects in these small regions.

In this analysis the effect of shock gradient in the direction of propagation is approximated by a temporal variation in the flow-field ( $\dot{k}$ ) past the cell. Thus, a steeper shock gradient (higher  $\dot{k}$ ) results in a higher value of  $T_{iner}$ . The effect of shock gradient on cell lysis has been studied experimentally by Doukas et al. [19], using laser generated stress waves. These investigators [19] have found a higher cell lysis with an increasing stress gradient in the direction of wave propagation. The stress wave propagating through their cell sample was assumed to be uniform and planar. Their result would corroborate our hypothesis provided their stress wave is found to have curvature or non-uniform strength. Absence of curvature or lateral variations in their shockfront would mean that the stress gradient in the direction of the wave propagation solely determines membrane permeabilization, and this analysis needs to be suitably modified to take that into account. Also, with the lithotripter generated shock wave, it is not possible to control the lateral shock gradient independently of the shock rise time, since both of these are manifestation of the shock focusing effect. Hence, with this setup, it is not possible to differentiate the effects of lateral and transverse shock gradients on cell lysis.

The limitations of the analysis presented in this work are now discussed:

- The analysis presented here is applicable to flows having a length-scale much larger than the cell dimension. Thus, while describing the interaction of the shock with the cell (section 4.7.1), an assumption of linearly increasing  $k(t)$  was made for times  $0 < t < 3$  ns. Also, while analyzing the radial-flow–RBC interaction (section 4.7.2), the cell was assumed to be initially located at ( $R_{cell0} =$ ) 40  $\mu\text{m}$  from the bubble center, since  $R_{cell} \sim \mathcal{O}(r_c)$  cannot be accurately described by this analysis.

- The extensional flow-field, described by the parameter  $k(t)$ , was assumed to be given (either derived from experimental measurements, or calculated), and not influenced by the cell deformation. It is immediately apparent that for the viscous mode of deformation (figure 4.2b), viscous effects alter the main flow, from which the extensional flow is derived, i.e., the radial flow-field, due to bubble growth, is damped out by viscous flow past the cell. Hence, for a more accurate description of this interaction, this damping effect should be accounted for in the bubble response model.
- The membrane was characterized by static mechanical properties. The growth of an unstable pore is a highly statistical process, and a single value of critical membrane tension, and strain, does not adequately describe the process of membrane rupture. Also RBC membranes have visco-elastic properties ([9]), which influences cell deformation. The lines demarcating ‘lysis’ from ‘poration’ regimes can be more accurately determined by accounting for the visco-elastic properties of the membrane.
- In section 4.5, while estimating  $T_{visc}$ , the membrane was assumed to remain stationary, and not deform with the extensional flow. Hence for times during which  $T_{elas} \gg T_{iner}$ , the above assumption gives an over-estimate of  $T_{visc}$  (as shown in figures 4.10c and 4.13c). Also, the model problem for calculating  $T_{visc}$  was an unsteady unidirectional flow (as discussed in C), which is valid for early times. For later times, the model problem should be an axisymmetric stagnation flow (see [52], page 208), in order to account for the two-dimensionality of the flow.
- In this analysis, only radially outward flow was considered, with the cell oriented such that its axis of symmetry coincides with a radial direction. This ensures that the cell membrane will always be subjected to a tension. A compressive stress, in the plane of the membrane, would cause the membrane to buckle, and complicate the analysis. Thus, analysis of cell deformation, having an arbitrary orientation with respect to the extensional flow, requires membrane buckling to

be incorporated, which is a more difficult problem and is beyond the scope of this preliminary work.

- Experiments investigating exposure of RBC's to shock waves usually determine the amount of hemoglobin in the suspending medium, after exposure. This is used to calculate the fraction of RBC population which has lysed. In this work, the membrane stresses and strains of an individual RBC were determined, at a particular location in the flow-field. Though this enables us to determine the effectiveness of a flow-field to lyse a cell, this analysis needs to be extended, to obtain the fraction of cell population lysed, in the entire flow-field. This would enable a comparison of the theory with experimental results.
- This analysis needs to be extended to *in vivo* environment. *In vivo*, bubble growth is highly constrained due to the presence of the enclosing tissue material, but at the same time the cells will be in close contact with the growing/collapsing bubble. Shock waves propagating through a random medium would be attenuated, but highly regular acoustic inhomogeneities can cause variation in shock strength and a differential motion lateral to the shockfront ([31, 34]). *In vivo* effects were ignored in these calculations since it is difficult to estimate them, and in this preliminary work the intention was to interpret *in vitro* results.

## 5.2 Experiments

### 5.2.1 Cell lysis

The analysis showed that both the flow-fields, i.e., that of a focused shock and the radial motion due to bubble expansion were able to induce stresses of the order of critical stress required to rupture a RBC membrane. However, the shock wave flow-field applies this stress for a very small duration, and the membrane strain is estimated to be several orders smaller than that required for failure. Hence, the

fraction of cells lysed due to lithotripter shock waves under conditions which preclude cavitation was smaller ( $\sim 0.5\%$  above control after 75 shocks; [75]) than lysis under atmospheric conditions ( $1.5 - 6.5\%$  above control, depending on cell suspension and vial orientation; [75]), where cavitation occurs. As reported in this work, the refocused wave-field from the parabolic reflector lysed  $\sim 3\%$  cells above control after 150 shocks, whereas the reflected wave-field from a flat reflector lysed only  $1\%$  cells above control. Thus, cell lysis correlates with the lateral shock gradient and corroborates the shearing mechanism.

### 5.2.2 Cavitation detection and suppression

In the present work a novel cavitation detector (HP-PCD) was devised, which measured acoustic emission from the focal region of the lithotripter under conditions of high overpressure. The free-field acoustic emission measured by this detector indicated the typical double-bang signature. The presence of a parabolic or a flat reflector at F2 modified this signal and delayed the collapse of the bubble cloud. Calculations using single-bubble model (e.g., Rayleigh model or Gilmore model) do not predict such a modification in the collapse times and this effect needs to be investigated. In the presence of the pressure chamber, the double bang emission was conspicuously absent. The influence of the pressure chamber on cloud collapse could be possibly due to one of the following: a) waves reflecting from the cylinder walls cause the bubble cloud to collapse prematurely, b) since the chamber restricts free circulation of water, cavitation nuclei are not easily available, leading to a lack of cloud formation and collapse. An overpressure of  $5.5 \text{ MPa}$  was determined to be sufficient to suppress all acoustic emission.

### 5.2.3 Foil damage

Aluminum foil targets were exposed to the lithotripter wave-field and the reflected wave-field at various overpressures. Aluminum foils subjected to the refocused wave at an overpressure  $\sim 12 \text{ MPa}$  did not show the typical pitting damage, but instead



a single depression/dent with wrinkled surface was observed. Unlike pitting damage which can be suppressed by applying overpressure, these deformation features were persistent at elevated pressures. The dent formed on the foil can be obtained by the application of a force which is concentrated at the center of the foil and reduces radially outwards. Such a force distribution is consistent with the off-axis distribution of peak pressures of the refocused wave-field and the dent dimension corresponds to the 6 dB width of the refocused wave-field. Hence, these foil deformation features are attributed to the refocused shock wave. Cellophane films were also used to study the shock wave damage. The damage pattern is comprised of holes and tears, which is attributed to cavitation micro-jetting and shock wave propagation, respectively. A lower overpressure was needed for eliminating cavitation holes, as compared to the overpressure needed to suppress pitting on aluminum foils, which is attributed to lower surface roughness of the cellophane films.

## 5.3 General

### 5.3.1 Optimized wave-field

The goal of this study was to understand the damage mechanisms in the stone/tissue medium and suggest modifications to the lithotripter wave-field which will minimize tissue injury and enhance stone comminution, by exploiting the differences in the damage mechanisms. In figure 5.2 a comparison of two focused wave-fields with different beam-widths, but identical acoustic energy, is depicted.

In [40] stone fragmentation due to spalling was analyzed. Stone damage, denoted by  $\chi_{sto}$ , was shown to be of the form

$$\Delta\chi_{sto} = A_{sto}\chi_{sto} + B_{sto}, \quad (5.1)$$

where  $A_{sto}$  and  $B_{sto}$  depend on physical properties of the stone and shock wave parameters. In [40] stone damage,  $\chi_{sto}$ , was characterized by the dimensions of the flaw in the stone. A more realistic measure would be the number of fragments formed, or

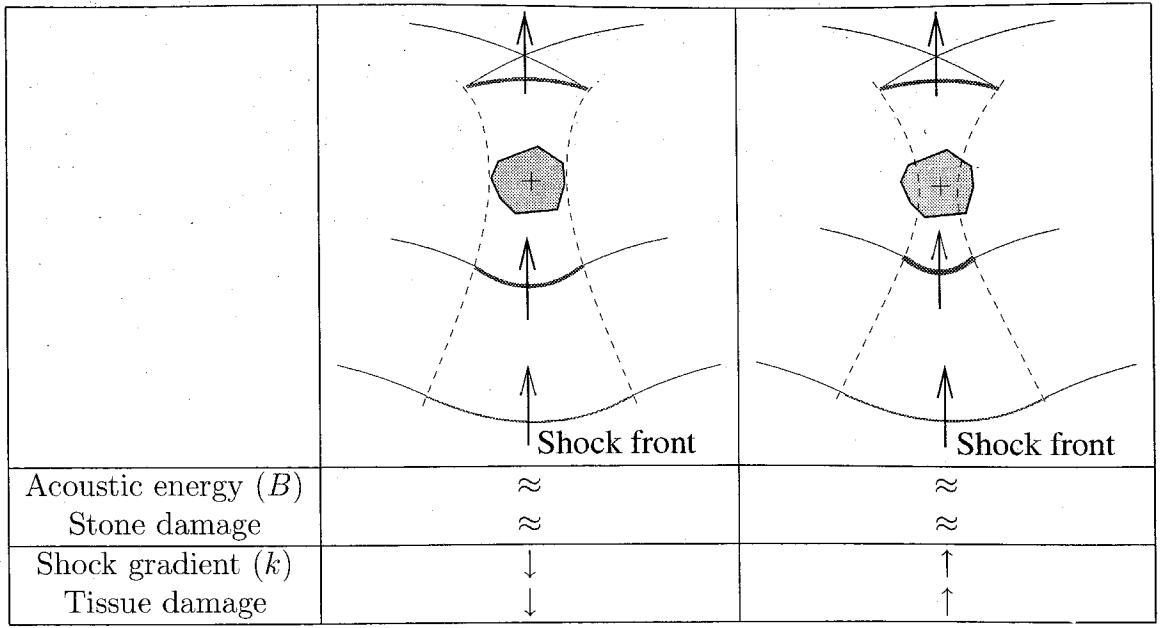


Figure 5.2: Stone vis-a-vis tissue damage for different focusing fields.

the stone surface area. The quantity  $A_{sto} \ll 1$  (note that the quantity  $A_{sto}$ , as used in 5.1 above, equals  $A_{sto} - 1$ , as defined in [40]) and hence the damage is mostly dependent on the parameter  $B_{sto}$  which can be shown to be related to the energy required for fragmenting which is due to the formation of new interfaces as the fragmentation proceeds. The source of this energy is the acoustic energy supplied by the wave-field. Thus, the acoustic energy of the wave-field will be the sole determinant of stone fragmentation if it is assumed that all the energy supplied by the lithotripter wave-field is utilized for stone fragmentation, and the stone does not reflect/transmit the energy to the surrounding medium, or energy does not get dissipated in the stone material by other mechanisms. Hence, in figure 5.2 the two wave-fields which have different beam-widths but identical acoustic energy will result in identical stone damage.

On the other hand cell lysis is dependent on the gradient of the shock strength, as seen from the cell lysis results (refer section 3.5). The acoustic energy of the reflected wave-field due to the flat and the parabolic reflector will be identical, since the incident wave-field is identical for both the cases, but the parabolic reflector has a higher cell lysis, which is due to a higher shock gradient ( $k$ ). Hence, the wave-

field of the beam with a tighter focus will result in a higher tissue damage. Thus a beam-width no smaller than the stone dimension would be ideal for this treatment.

### 5.3.2 Lysis modes

Though the primary motivation of this work was to analyze cell lysis due to SWL induced flow-fields, a systematic means of classifying all the previously reported modes of cell lysis, based on the nature of the predominant force, is presented in this section (figure 5.3). As discussed in section 4.3, the bilayer configuration is a metastable

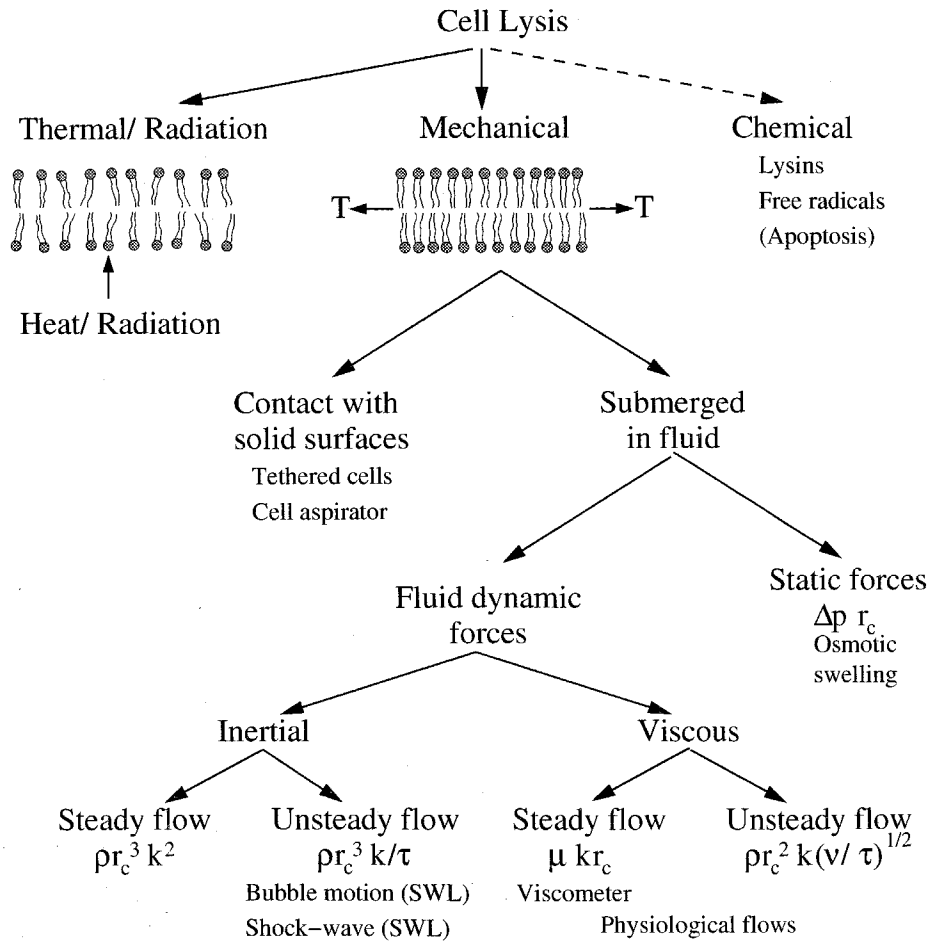


Figure 5.3: Cell lysis mechanisms and membrane forces.

state of the membrane, and membrane rupture can be effected by providing a sufficient amount of energy. Hence a very general classification of cell lysis mechanisms is

based on the means of providing this energy - i.e., thermal (or radiation) or mechanical. Chemically-induced lysis can be seen as an independent mode, or as an aid to the former two modes (e.g., by weakening the ultra-structure of the membrane, and lowering the energy needed for rupture). In mechanical modes, the cell membrane is subjected to a tension by mechanical means (e.g., the cell aspirator (figure 4.4) discussed earlier). A cell could be entirely submerged in a fluid medium, without any contact with a solid surface, or could be tethered (or in contact) to a solid surface. For cells submerged in a fluid medium, the membrane could be subjected to static forces (e.g., osmotic pressure), which do not arise due to bulk fluid motion. When there is bulk fluid motion, fluid dynamic forces are exerted on the cell membrane. These fluid dynamic forces are primarily inertial and viscous forces, either due to a steady or an unsteady flow. Cell lysis due to micro-streaming, or cell lysis in viscometers, are classified into the viscous steady-flow category, whereas the bubble-induced and shock-induced SWL flow-fields belong to the inertial, unsteady category.

Thus, this work provides a foundation for analyzing the interaction between the flow-field and the cell membrane. This analysis can be advanced to understand membrane poration and concomitant exchange of extra- intra-cellular material. A variety of related problems, including localized drug delivery using shock waves, increased hemolysis in prosthetic heart valves [21], etc., have a potential gain from such an improved understanding.

### 5.3.3 Summary

In figure 5.4 the current state of understanding of tissue damage mechanisms in SWL, including the contribution made by this work, is summarized. All experiments aiming to understand tissue damage mechanisms can be classified as either *in vivo* or *in vitro*. *In vitro* studies typically use RBC or polymer films as targets to study shock wave exposure effects whereas *in vivo* studies use an animal model (e.g., pig, mice, etc.). *In vitro* studies have shown overwhelming damage to RBC's and polymer films. This damage is attributed to cavitation due to the nature of the observed

	Cavitation	Shear
In-vitro (RBC, Al foils, Cellulose)	Overwhelming evidence  Acoustic emissions from bubble clouds	RBC lysis, foil damage ~ shock gradient <b>(this work)</b>
In-vivo (human ~ pig)	Similar emissions not detected  (does cavitation occur ?) (as intense as in-vitro ?)	<b>?????</b>  (no cavitation hence shear ?)

Figure 5.4: A summary of experimental work and the current state of understanding of tissue damage mechanisms in SWL.

damage. Also, *in vitro* measurements of cavitation emissions indicate a significant bubble activity, commensurate with the observed *in vitro* damage. However, similar acoustic emissions have not been measured under *in vivo* exposure conditions. Hence it is not clear whether cavitation occurs *in vivo* and whether its damaging effects are comparable to that of *in vitro* exposure conditions.

In this work experiments showed that damage to RBC and foils was related to the shock gradient, in accordance with the shearing mechanism. Although, this work concludes that shearing would be a pre-dominant damage mechanism under exposure conditions which suppress cavitation, it does not provide any direct evidence suggesting shearing as a pre-dominant *in vivo* damage mechanism. Such evidence could only be obtained from *in vivo* studies. An alternative strategy would be to characterize the effects of *in vivo* environment on shock wave propagation and bubble dynamics, and then simulate the same effects in *in vitro* experiments.

## Appendix A List of symbols

$\delta_w$	boundary layer thickness
$\gamma$	ratio of specific heats
$\omega$	vorticity
$\mu$	viscosity (Pa s)
$\nu$	kinematic viscosity (m <sup>2</sup> /s)
$\phi$	velocity potential
$\rho$	density (kg/m <sup>3</sup> )
$\sigma_e$	compressive stress across membrane thickness
$\tau_w$	tangential wall stress
$\Gamma$	edge energy of pore
$c$	acoustic speed (m/s)
$h_c$	cell width
$k$	rate of flow-field deformation (s <sup>-1</sup> )
$p_{shock}$	shock pressure
$p$	pressure
$p_0$	ambient pressure
$p_\infty$	far-field pressure
$p_g$	gas pressure inside bubble
$r_p$	pore radius
$r, z$	cylindrical coordinates
$r_c$	cell radius ( $\mu\text{m}$ )
$t, \tau$	time (s)
$u, U$	velocity in fixed frame
$u_{\tau R}, u_{zR}$	velocity components in moving reference frame
$u_R$	velocity of moving reference frame

$A$	cell surface area
$(\Delta A/A)_c$	critical membrane areal strain
$(\Delta A/A)_p$	membrane strain due to a pore
$E_s$	surface elasticity modulus (mN/m)
$M_s$	shock Mach number
$Q(t)$	source/sink strength
$R$	radial coordinate
$R_b$	bubble radius
$R_{cell}$	radial location of cell center
$Re$	Reynolds' number
$T$	membrane tension (mN/m)
$T_c$	critical membrane tension
$T_{elas}$	elastic tension
$T_{iner}$	inertial tension
$T_{st}, T_{unst}$	steady/unsteady tension
$T_{visc}$	viscous tension
$U_b$	bubble wall velocity
$U_{cell}$	cell center velocity

## Appendix B Decomposition of radial flow-field

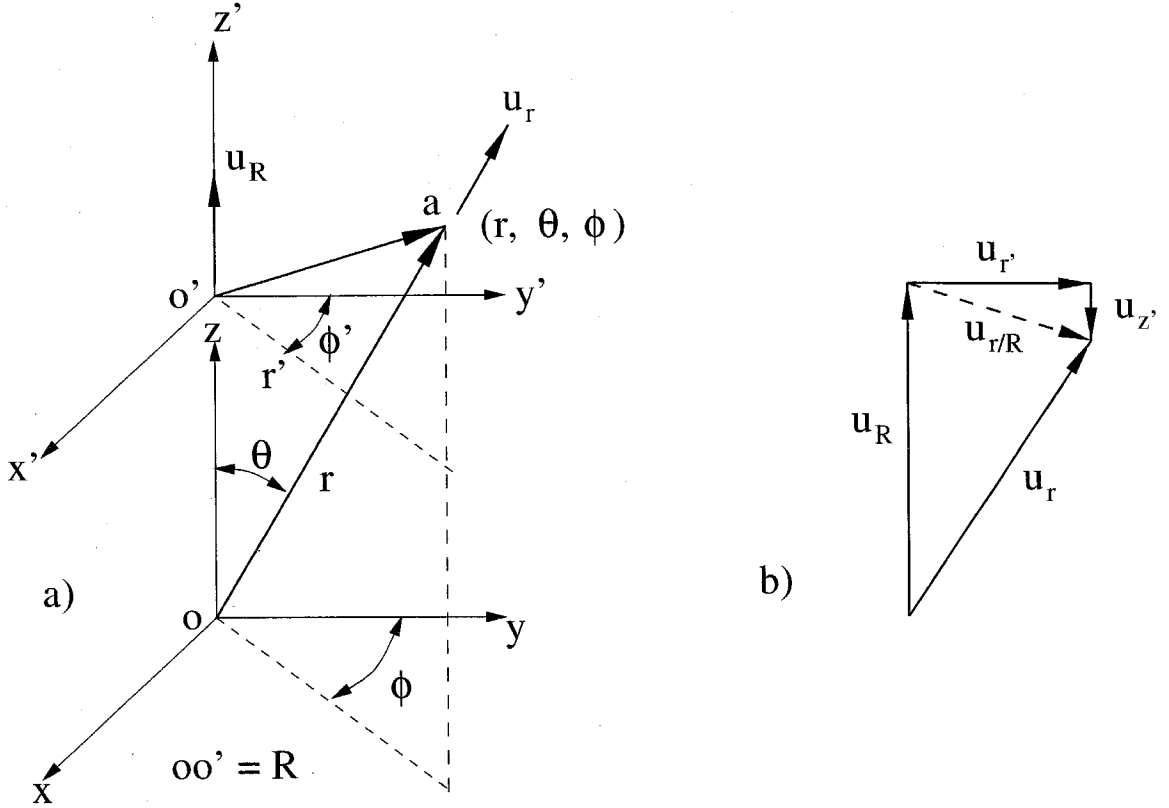


Figure B.1: Radial flow decomposition. a) Coordinate system  $(x, y, z)$  is fixed in space, with source at its origin,  $(x', y', z') \equiv (r', z', \phi')$  is moving with the particle velocity  $u_R$ . b) Resolving velocity components in the moving co-ordinate system  $(r', z', \phi')$ .

Three-dimensional radial flow is given by

$$\vec{u}_r = \frac{Q(t)}{4\pi r^2} \vec{e}_r, \quad (\text{B.1})$$

where  $Q(t)$  represents an unsteady source term at  $r = 0$ ,  $r$  is the radial coordinate



with respect to the source location (in figure B.1a, the source is located at the origin of the  $(x, y, z)$  reference system), and  $\vec{e}_r$  is a unit vector along the radial direction (oa). The coordinate transformation from the fixed frame of reference  $(x, y, z)$  to the moving frame of reference  $(x', y', z')$  (this is equivalent to  $(r', z', \phi')$ ) is given by

$$(\phi', r', z') = (\phi, r \sin \theta, r \cos \theta - R). \quad (\text{B.2})$$

Non-dimensionalize  $r', z'$  by  $R$  and denoting them as  $r'', z''$ , we get

$$r^2 = R^2((z'' + 1)^2 + r''^2), \quad (\text{B.3})$$

$$\cos \theta = (z'' + 1)/((z'' + 1)^2 + r''^2)^{1/2}, \quad (\text{B.4})$$

$$\sin \theta = r''/((z'' + 1)^2 + r''^2)^{1/2}. \quad (\text{B.5})$$

For brevity, the double primes (") over normalized variables will be dropped. Using the above transformation, (B.1) can be written as

$$\vec{u}_r = \frac{Q(t)}{4\pi R^2} \frac{(\vec{e}_{r'} \sin \theta + \vec{e}_{z'} \cos \theta)}{(z + 1)^2 + r^2}, \quad (\text{B.6})$$

where  $\vec{e}_{r'}, \vec{e}_{z'}$  are unit vectors along  $r', z'$  directions shown in figure B.1a. The velocity of the moving reference frame  $(x', y', z')$  is,  $u_R(t) = Q(t)/(4\pi R^2) \vec{e}_{z'}$ . The components of the velocity field, given by B.6, expressed in the moving reference frame is given by

$$u_{rR} = u_R(t) \left( \frac{r}{((z + 1)^2 + r^2)^{3/2}} \right), \quad (\text{B.7})$$

$$u_{zR} = u_R(t) \left( \frac{z + 1}{((z + 1)^2 + r^2)^{3/2}} - 1 \right), \quad (\text{B.8})$$

where the subscript  $r_R, z_R$  indicates the  $r, z$  components relative to the moving frame. Linearizing the velocity components, i.e., assuming  $r, z \ll 1$ , (B.7, B.8) can be written

as (consistent to  $\mathcal{O}(r^2, z^2, zr)$ )

$$u_{rR} = u_R(t) (r - 3zr), \quad (\text{B.9})$$

$$u_{zR} = u_R(t) (-2z + 3z^2 - \frac{3}{2}r^2). \quad (\text{B.10})$$

The above equations can be checked to satisfy the continuity equation,

$$\frac{1}{r} \frac{\partial(ru_{rR})}{\partial r} + \frac{\partial(u_{zR})}{\partial z} = 0, \quad (\text{B.11})$$

and the condition for potential flow,  $\vec{u} = \nabla\phi$ , with the velocity potential being

$$\phi(t) = R u_R(t) \left( \frac{r^2}{2} - z^2 - \frac{3}{2}zr^2 + z^3 \right). \quad (\text{B.12})$$

For a shear flow,

$$\vec{u}(x, y, z) = U (1, 0, 0) + (k(t)y, 0, 0), \quad (\text{B.13})$$

the decomposition is fairly trivial. Equation (B.13) can be written as

$$\vec{u}(x, y, z) = U (1, 0, 0) + \left( \frac{k(t)}{2}y, \frac{-k(t)}{2}x, 0 \right) + \left( \frac{k(t)}{2}y, \frac{k(t)}{2}x, 0 \right). \quad (\text{B.14})$$

The three terms on the right side of (B.14) represent the following, respectively: uniform translation, rotation about z-axis, and an extensional flow, with the principal axes of deformation oriented at  $45^\circ$  to the  $(x, y)$  coordinate system. The linearized ( $\mathcal{O}(r, z)$  terms only) version of (B.9, B.10) is an axisymmetric extensional flow in  $(r, z)$  plane, whereas the last bracketed term in (B.14) represents planar extensional flow (in  $(x, y)$  plane). From the above definitions,  $k(t)/2$  can be seen to be an eigen-value of the deformation component,  $(\nabla u + \nabla u^T)/2$ , of the flow. In a general situation, there will be three distinct, real, eigen-values,  $k_i(t)$ , satisfying the condition,  $\sum_{i=1}^3 k_i(t) = \frac{1}{\rho} \frac{d\rho}{dt}$ , which is the unsteady continuity equation. For an incompressible flow-field, as assumed in this work,  $\sum_{i=1}^3 k_i(t) = 0$ , since  $\rho = \text{constant}$ .

## Appendix C Stokes' I<sup>st</sup> problem

The problem of an impulsively started solid boundary is known as Stokes' I<sup>st</sup> problem. The case in which the solid boundary is stationary, but the flow is started impulsively is exactly identical, and will be dealt here briefly. Figure C.1 shows the problem configuration. The momentum equation in x-direction is a diffusion equation given by

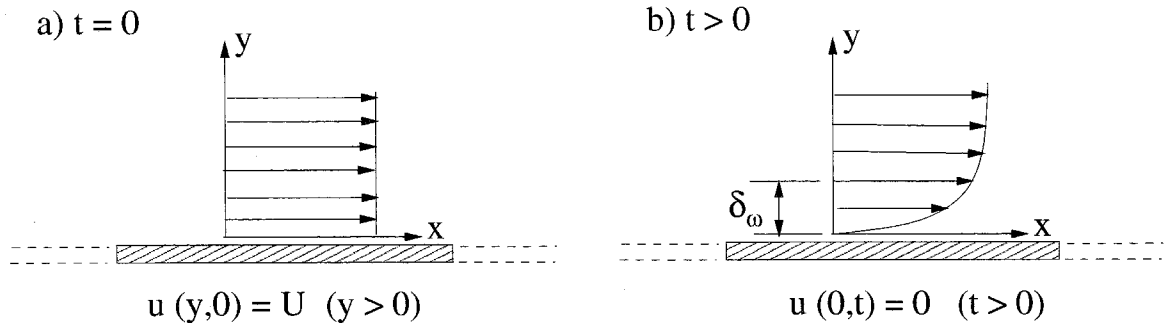


Figure C.1: Definition sketch for Stokes' first problem - impulsively started flow, past a stationary wall. a) Initial condition,  $t = 0$ . b)  $t > 0$ .

$$\frac{\partial u}{\partial t} = \nu \frac{\partial^2 u}{\partial y^2}, \quad (\text{C.1})$$

subject to boundary conditions,

$$u(y,0) = U \quad (y > 0), \quad u(0,t) = 0 \quad (t \geq 0). \quad (\text{C.2})$$

The solution to the above equation can be obtained by using similarity variables, and could be found in any standard textbook (e.g., Pozrikidis 1997, page 192). The solution is given by

$$u(y,t) = U \operatorname{erf} \eta, \quad (\text{C.3})$$

where

$$\operatorname{erf} \eta = \frac{2}{\sqrt{\pi}} \int_0^\eta e^{-x^2} dx, \quad \eta = \frac{y}{2\sqrt{\nu t}}. \quad (\text{C.4})$$

From the above solution, the vorticity at the wall,  $\omega(0, t)$ , is obtained as

$$\omega(0, t) = \left. \frac{\partial u}{\partial y} \right|_{y=0} = \frac{U}{\sqrt{\pi \nu t}}. \quad (\text{C.5})$$

The vorticity thickness, which is a measure of the width of the boundary layer, or the thickness of the region influenced by the wall due to fluid viscosity, is given by

$$\delta_\omega = \frac{u(0, t)}{\omega(0, t)} = \sqrt{\pi \nu t}. \quad (\text{C.6})$$

The tangential stress on the solid boundary, which is identical to fluid shear stress, is given by

$$\tau_w = \mu \left. \frac{\partial u}{\partial y} \right|_{y=0} = \frac{\mu U}{\sqrt{\pi \nu t}} = \rho U \sqrt{\frac{\nu}{\pi t}}. \quad (\text{C.7})$$

As seen from (C.6) the boundary layer,  $\delta_\omega$ , grows as  $t^{1/2}$ , whereas the wall stress,  $\tau_w$ , is initially infinite and decays as  $t^{-1/2}$ , as seen from (C.7). This is a consequence of the impulsive motion of the fluid, i.e., if the fluid attains a finite velocity in an infinitesimal time. The above solution is now modified to account for a finite rise time, or in general, for any arbitrary  $U(t)$ . Assume that the fluid motion at  $t$  is built up by tiny impulses  $dU(\tau)$ , of the far field, at some time  $\tau$ , then

$$du(t) = dU(\tau) \operatorname{erf} \frac{y}{2\sqrt{\nu(t-\tau)}}. \quad (\text{C.8})$$

The complete flow is given by the integral

$$u(t) = \int_0^t \frac{dU(\tau)}{d\tau} \operatorname{erf} \frac{y}{2\sqrt{\nu(t-\tau)}} d\tau, \quad (\text{C.9})$$

and the wall stress is given by

$$\tau_w = \rho \sqrt{\frac{\nu}{\pi}} \int_0^t \frac{dU(\tau)}{d\tau} \frac{1}{\sqrt{(t-\tau)}} d\tau. \quad (\text{C.10})$$

The wall stress is evaluated explicitly for a few velocity profiles,  $U(\tau)$ .

*Case I: Linear ramp.* The far-field fluid velocity increases linearly with time, i.e.,

$$U(\tau) = K\tau, \quad \tau \geq 0, \quad K > 0. \quad (\text{C.11})$$

Substituting (C.11) in (C.10), the wall stress is obtained as

$$\tau_w = 2\rho K \sqrt{\frac{\nu t}{\pi}} = 2\rho U \sqrt{\frac{\nu}{\pi t}}. \quad (\text{C.12})$$

Thus, as seen in (C.12), the wall stress,  $\tau_w$ , is finite, increases as  $t^{1/2}$ , and depends on  $K$ , the rate of increase of  $U$ .

*Case II: Shock-like velocity profile.* In this case, the far-field velocity reaches a maximum value,  $U_{max}$ , in a finite time,  $\tau_1$ , and then decays to zero in finite time,  $\tau_2$  (as shown in figure 4.10a). Thus,  $U(\tau)$  is defined as

$$U(\tau) = U_{max} \frac{\tau}{\tau_1}, \quad 0 \leq \tau \leq \tau_1, \quad (\text{C.13})$$

$$= U_{max} \left(1 - \frac{\tau - \tau_1}{\tau_2}\right), \quad \tau_1 \leq \tau \leq \tau_1 + \tau_2, \quad (\text{C.14})$$

$$= 0, \quad \tau \geq \tau_1 + \tau_2. \quad (\text{C.15})$$

Substituting the above defined  $U(\tau)$  in (C.10), the wall stress is obtained as

$$\tau_w = 2\rho \frac{U_{max}}{\tau_1} \sqrt{\frac{\nu t}{\pi}} = \tau_{w1}, \quad 0 \leq t \leq \tau_1, \quad (\text{C.16})$$

$$= \tau_{w1} \left\{ 1 - \left(1 + \frac{\tau_1}{\tau_2}\right) \sqrt{1 - \frac{\tau_1}{t}} \right\}, \quad \tau_1 \leq t \leq \tau_1 + \tau_2, \quad (\text{C.17})$$

$$= \tau_{w1} \left\{ 1 - \left(1 + \frac{\tau_1}{\tau_2}\right) \sqrt{1 - \frac{\tau_1}{t}} + \frac{\tau_1}{\tau_2} \sqrt{1 - \frac{\tau_1 + \tau_2}{t}} \right\}, \quad t \geq \tau_1 + \tau_2. \quad (\text{C.18})$$

Equation (C.16) is identical to (C.12), with  $K$  replaced by  $U_{max}/\tau_1$ , since both are linear ramps. In the limit as  $\tau_1/\tau_2 \rightarrow 0$  and  $\tau_1/t \rightarrow 0$ , this case becomes identical to the impulsively started flow. The expression for wall stress (C.17), in the above limit, becomes identical to (C.7).

## Appendix D Membrane force balance

The problem configuration is illustrated in figure D.1. A planar membrane is subject to tangential stress,  $\tau_w$ , and the objective is to calculate the meridian and the tangential tensions,  $T_1$  and  $T_2$ , respectively. Axisymmetric conditions are assumed, i.e.,

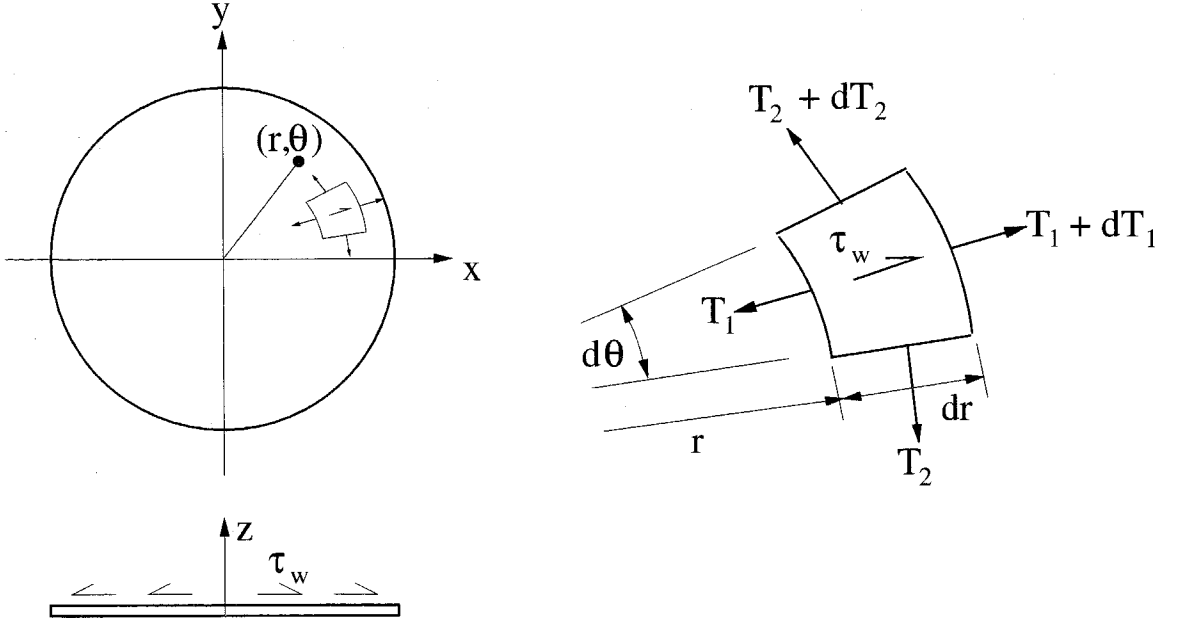


Figure D.1: Force balance for membrane.

$\partial(\ )/\partial\theta = 0$ . The radial force balance for an element shown in figure D.1 is given by

$$(T_1 + \frac{dT_1}{dr} dr)(r + dr) d\theta + \tau_w dr (r + \frac{dr}{2}) dr d\theta = T_1 r d\theta + T_2 dr d\theta. \quad (D.1)$$

Neglecting terms of  $\mathcal{O}(dr^2)$ , (D.1) can be written as

$$\frac{dT_1}{dr} + \frac{T_1 - T_2}{r} = -\tau_w(r). \quad (D.2)$$

For an axisymmetric problem, the radial (or meridonial) and the tangential directions are also the principal directions, hence no in-plane shear exists along these directions.

Further, radial symmetry, and material isotropy, in the radial and tangential directions, requires  $T_1(r) = T_2(r)$ . Thus (D.2) simplifies to

$$\frac{dT_1}{dr} = -\tau_w(r) , \quad (\text{D.3})$$

which, upon integrating, gives

$$T_{1r=r} - T_{1r=r_c} = \int_r^{r_c} \tau_w(r) dr . \quad (\text{D.4})$$

Thus if the edge of the membrane is free,  $T_{1r=r_c} = 0$ , and the wall stress,  $\tau_w(r)$ , always points radially outward over the entire membrane, then the maximum tension occurs at the membrane center ( $r = 0$ ), obtained from (D.4).

# Bibliography

- [1] R Aris. *Vectors, tensors, and the basic equations of fluid mechanics*. New York: Dover Publications Inc., 1989.
- [2] M R Bailey, D T Blackstock, R O Cleveland, and L A Crum. Comparison of electrohydraulic lithotripters with rigid and pressure-release ellipsoidal reflectors: I. acoustic fields. *Journal Acoust. Soc. Am.*, 104:(4) 2517–24, 1998.
- [3] M R Bailey, D T Blackstock, R O Cleveland, and L A Crum. Comparison of electrohydraulic lithotripters with rigid and pressure-release ellipsoidal reflectors: Ii. cavitation fields. *Journal Acoust. Soc. Am.*, 106:(2) 1149–60, 1999.
- [4] D Barthes-Biesel. Motion of a spherical microcapsule freely suspended in a linear shear flow. *J. Fluid Mech.*, 100:(4) 831–53, 1980.
- [5] P L Blackshear and G L Blackshear. Mechanical hemolysis. In R Skalak and S Chien, editors, *In: Handbook of Bioengineering*. New York: McGraw Hill Inc., 1987.
- [6] J R Blake and D C Gibson. Cavitation bubbles near boundaries. *Ann. Rev. Fluid Mech.*, 19:99–123, 1987.
- [7] E L Carstensen, P Kelly, C C Church, A A Brayman, S Z Child, C H Raeman, and L Schery. Lysis of erythrocytes by exposure to cw ultrasound. *Ultrasound Med. Biol.*, 19:(2) 147–65, 1993.
- [8] C Chaussy and G J Fuchs. Current state and future developments of non-invasive treatment of human urinary stones with eswl. *J. Endourol.*, 141:782–9, 1989.
- [9] S Chien, K L P Sung, R Skalak, S Usami, and A Tözeren. Theoretical and experimental studies on viscoelastic properties of erythrocyte membrane. *Biophys. J.*, 24:463–87, 1978.



- [10] M J Choi, A J Coleman, and J E Saunders. The influence of fluid properties and pulse amplitude on bubble dynamics in the field of a shock-wave lithotripter. *Phys. Med. Biol.*, 38:(11) 1561–73, 1993.
- [11] C C Church. A theoretical study of cavitation generated by an extracorporeal shockwave lithotripter. *J. Acous. Soc. Am.*, 86:(1) 215–27, 1989.
- [12] R O Cleveland, M R Bailey, N Fineberg, B Hartenbaum, M Lokhandwalla, J A McAteer, and B Sturtevant. Design and characterization of a research electrohydraulic lithotripter patterned after the dornier hm3. *Rev. Sci. Instr.*, 71:(6) 2514–25, 2000.
- [13] R O Cleveland, O A Sapozhnikov, R M Bailey, and L A Crum. A dual passive cavitation detector for localized detection of lithotripsy-induced cavitation in vitro. *Journal Acoust. Soc. Am.*, 107:(3) 1745–58, 2000.
- [14] A J Coleman, M J Choi, J E Saunders, and T G Leighton. Acoustic emission and sonoluminescence due to cavitation at the beam focus of an electrohydraulic shock wave lithotripter. *Ultrasound Med. Biol.*, 18:267–81, 1992.
- [15] A J Coleman and J E Saunders. A review of the physical properties and biological effects of the high amplitude acoustic fields used in extracorporeal lithotripsy. *Ultrasonics*, 31:75–89, 1993.
- [16] A J Coleman, J E Saunders, L A Crum, and M Dyson. Acoustic cavitation generated by an extracorporeal shockwave lithotripter. *Ultrasound Med. Biol.*, 13:69–76, 1987.
- [17] A J Coleman, J E Saunders, R C Preston, and D R Bacon. Pressure wave-forms generated by a dornier extracorporeal shockwave lithotripter. *Ultrasound Med. Biol.*, 13:651–7, 1987.
- [18] M Delius. Minimal static pressure minimizes the effect of extracorporeal shock waves on cells and reduces it on gallstones. *Ultrasound Med. Biol.*, 23:611–17, 1997.

- [19] A G Doukas, D J McAuliffe, S Lee, V Venugopalan, and T Flotte. Physical factors involved in stress-wave-induced cell injury: the effect of stress gradient. *Ultrasound Med. Biol.*, 21:961-7, 1995.
- [20] W Eisenmenger, M Köhler, R Pech, and C Wurster. Negative pressure amplitudes in water measured with fiber optic hydrophone. *Progress in Nat. Sci.*, 7:(4) 499-501, 1997.
- [21] J T Ellis, T M Wick, and A P Yoganathan. Prosthesis-induced hemolysis: Mechanisms and quantification of shear stress. *J. Heart Valve Dis.*, 7:(4) 376-86, 1998.
- [22] A P Evan and J A McAteer. Q-effects of shock wave lithotripsy. In F L Coe and M J Favus et al., editors, *Kidney Stones: Medical and Surgical Management*, pages 549-70. Philadelphia: Lippincott-Raven, 1996.
- [23] E A Evans and Y C Fung. Improved measurements of the erythrocyte geometry. *Microvasc. Res.*, 4:335-47, 1972.
- [24] E A Evans, R Waugh, and L Melnik. Elastic area compressibility modulus of red cell membrane. *Biophys. J.*, 16:585-95, 1976.
- [25] R J Forstrom. *A new measure of erythrocyte membrane strength: The jet fragility test*. Ph.D. thesis, University of Minnesota, Minneapolis, St. Paul., 1969.
- [26] Y C Fung. *Biomechanics: Mechanical properties of living tissues*. Springer-Verlag, 1993.
- [27] P E Hamrick and S F Cleary. Breakage of tobacco mosaic virus by acoustic transients: A hydrodynamical model. *J Acous. Soc. Am.*, 45:1-6, 1969.
- [28] C R Hill and G R terHaar. Review article - high intensity focused ultrasound-potential for cancer treatment. *Brit. J. Rad.*, 68:1296-1303, 1995.
- [29] R M Hochmuth, P R Worthy, and E A Evans. Red cell extensional recovery and the determination of membrane viscosity. *Biophys. J.*, 26:101-14, 1979.

- [30] D D Howard. *Mechanisms of injury associated with extracorporeal shock wave lithotripsy*. Ph.D. thesis, California Institute of Technology, Pasadena, 1996.
- [31] D D Howard and B Sturtevant. In vitro study of the mechanical effects of shock wave lithotripsy. *Ultrasound Med. Biol.*, 23:(7) 1107–22, 1997.
- [32] C Jakobiet, M Amend, W Johanns, R Schumacher, and L Greiner. Extracorporeal shockwave lithotripsy of extra- and intraheptic bile duct stones - 9 years experience. In C Chaussy, F Eisenberger, D Jocham, and D Wilbert, editors, *High energy shockwaves in medicine*. Stuttgart: Thieme, 1997.
- [33] J V Kaude, C M Williams, M R Millnder, K N Scott, and B Finlayson. Renal morphology and function immediately after extracorporeal shock-wave lithotripsy. *Am. J. Roentgenol*, 145:305–13, 1985.
- [34] T Kodama and K Takayama. Dynamic behavior of bubbles during extracorporeal shock-wave lithotripsy. *Ultrasound Med. Biol.*, 24:(5) 723–38, 1998.
- [35] L B Leverett, J D Hellums, C P Alfrey, and E C Lynch. Red blood cell damage by shear stress. *Biophys. J.*, 12:257–73, 1972.
- [36] X Z Li, D Barthes-Biesel, and A Helmy. Large deformations and burst of a capsule freely suspended in an elongational flow. *J. Fluid. Mech.*, 187:179–96, 1988.
- [37] D A Lifshitz, J C Williams Jr, B Sturtevant, B A Connors, A P Evans, and J A McAteer. Quantization of shock wave cavitation damage in-vitro. *Ultrasound Med. Biol.*, 23:461–71, 1997.
- [38] J E Lingeman. Extracorporeal shock wave lithotripsy - development, instrumentation, and current status. *Urol. Clinics of North America*, 24:185, 1997.
- [39] J D Litster. Stability of lipid bilayers and red blood cell membranes. *Physics letters*, 53A:193–4, 1975.

- [40] M Lokhandwalla and B Sturtevant. Fracture mechanics model of stone comminution in eswl and implications for tissue damage. *Phys. Med. Biol.*, 45:(7) 1923–40, 2000.
- [41] M Lokhandwalla and B Sturtevant. Mechanical haemolysis in shock wave lithotripsy (SWL): I. Analysis of cell deformation due to SWL flow-fields. *Phys. Med. Biol.*, 46:(2) 413–37, 2001.
- [42] M Lokhandwalla, B Sturtevant, J C Williams Jr., and J A McAteer. Mechanical haemolysis in shock wave lithotripsy (SWL): II. In vitro cell lysis due to shear. *Phys. Med. Biol.*, 46, 2001.
- [43] D J McAuliffe, S Lee, T J Flotte, and A G Doukas. Stress-wave-assisted transport through the plasma membrane in vitro. *Lasers in Surgery and Medicine*, 20:216–22, 1997.
- [44] M W Miller, D L Miller, and A A Brayman. A review of in vitro bioeffects of inertial ultrasonic cavitation from a mechanistic perspective. *Ultrasound Med. Biol.*, 22:(9) 1131–54, 1996.
- [45] M Muller. Comparison of dornier lithotripters: Measurement of shock wave fields and fragmentation effectiveness. *Biomedizinische Technik*, 35:250–62, 1990.
- [46] D Needham and R M Hochmuth. Electro-mechanical permeabilization of lipid vesicles - role of membrane tension and compressibility. *Biophys. J.*, 55:1001–9, 1989.
- [47] E Neumann and K Rosenheck. Permeability changes induced by electric impulses in vesicular membranes. *J Membrane Biol.*, 10:279–90, 1972.
- [48] H T O’Niel. Theory of focusing radiators. *Journal Acoust. Soc. Am.*, 21:516–26, 1949.
- [49] M Ortiz. Microcrack coalescence and macroscopic crack growth initiation in brittle solids. *Int. J. Solids Structures*, 24:231–50, 1988.

- [50] D G Pellinen, M S Di Capua, E Stephen, E Sampayan, H Gerbacht, and M Wang. Rogowski coil for measuring fast, high-level pulsed currents. *Rev. Sci. Instr.*, 51:1535–40, 1980.
- [51] E Ponder. *Hemolysis and related phenomena*. New York: Grunne & Stratton, 1948.
- [52] C Pozrikidis. *Introduction to theoretical and computational fluid dynamics*. New York: Oxford University Press, 1997.
- [53] S Ramanujan and C Pozrikidis. Deformation of liquid capsules enclosed by elastic membranes in simple shear flow: large deformations and the effect of fluid viscosities. *J. Fluid. Mech.*, 361:117–43, 1998.
- [54] R P Rand. Mechanical properties of the red cell membrane: II. viscoelastic breakdown of the membrane. *Biophys. J.*, 4:303–16, 1964.
- [55] R P Rand and A C Burton. Mechanical properties of the red cell membrane: I. membrane stiffness and intracellular pressure. *Biophys. J.*, 4:115–35, 1964.
- [56] J W Rayleigh. On the pressure developed in a liquid during the collapse of a spherical cavity. *Philos. Mag.*, 34:94–8, 1917.
- [57] J A Rooney. Hemolysis near an ultrasonically pulsating gas bubble. *Science*, 169:869–71, 1970.
- [58] J A Rooney. Shear as a mechanism for sonically induced biological effects. *J. Acous. Soc. Am.*, 52:(6) 1718–24, 1972.
- [59] W Saas, M Braunlich, H P Dreyer, E Matura, W Folberth, H G Priesmeyer, and J Siefert. The mechanisms of stone disintegration by shock waves. *Ultrasound Med. Biol.*, 17:239–43, 1991.
- [60] T Sauerbruch, M Delius, and G Paumgartner et al. Fragmentation of gall stones by extracorporeal shockwaves. *N. Eng. J. Med.*, 314:818, 1986.

- [61] R Schleberger, M Delius, G P Dahmen, R Diesch, W Schaden, R Thiele, and J Vogel. Orthopedic extracorporeal shockwave therapy (eswt) - method analysis and suggestion of a prospective study design - consensus report. In C Chaussy, F Eisenberger, D Jocham, and D Wilbert, editors, *High energy shockwaves in medicine*. Stuttgart: Thieme, 1997.
- [62] J W Segura, G M Preminger, D G Assimos, S P Drelter, R I Kahn, J E Lingeman, and J N Macaluso. Uretral stones clinical guidelines panel summary report on the management of ureteral calculi. *J. Urol.*, 158:1915–21, 1997.
- [63] J C Shillcock and D H Boal. Entropy driven instability and rupture of fluid membranes. *Biophys. J.*, 71:317–26, 1996.
- [64] M A Stonehill, J C Williams, M R Bailey, D Lounsbery, R O Cleveland, L A Crum, A P Evan, and J A McAteer. An acoustically matched high pressure chamber for control of cavitation in shockwave lithotripsy: Mechanism of shock wave damage in vitro. *Methods Cell Sci.*, 19:303–11, 1998.
- [65] B Sturtevant. Shock wave physics of lithotripters. In A D Smith et al., editor, *Smith's textbook of endourology*, pages 529–52. St. Louis: Quality Medical, 1996.
- [66] B Sturtevant and V A Kulkarny. The focusing of weak shock waves. *J. Fluid Mech.*, 73:651–71, 1976.
- [67] G R ter Haar, I Rivens, L Chen, and S Riddler. High intensity focused ultrasound for treatment of rat tumors. *Phys. Med. Biol.*, 36:1495–1501, 1991.
- [68] K Teshima, T Ohshima, S Tanaka, and T Nagai. Biomechanical effects of shock waves on *escherichia coli* and  $\lambda$ phage dna. *Shock Waves*, 4:293–7, 1995.
- [69] P A Thompson. *Compressible fluid dynamics*. New York: McGraw Hill, 1972.
- [70] C A Truesdell. *The kinematics of vorticity*. Bloomington, IN: Indiana University Press, 1954.

- [71] A Vogel and W Lauterborn. Acoustic transient generation by laser-produced cavitation bubbles near solid boundaries. *J. Acous. Soc. Am.*, 84:719–31, 1988.
- [72] K Vokurka. Comparison of rayleigh's, herring's, and gilmore's models of gas bubbles. *Acustica*, 59:214–9, 1986.
- [73] J C Weaver. Electroporation theory: Concepts and mechanisms. In J A Nickoloff et al., editor, *Methods in Molecular Biology, Vol 47: Electroporation Protocols for Microorganisms*. Totowa NJ: Humana Press Inc., 1995.
- [74] J C Williams, M A Stonehill, K Colmenares, A P Evan, S P Andreoli, R O Cleveland, M R Bailey, L A Crum, and J A McAteer. Effect of macroscopic air bubbles on cell lysis by shock wave lithotripsy in vitro. *Ultrasound Med. Biol.*, 25:(3) 473–9, 1999.
- [75] J C Williams, J F Woodward, M A Stonehill, A P Evan, and J A McAteer. Cell damage by lithotripter shock waves at high pressure to preclude cavitation. *Ultrasound Med. Biol.*, 25:1445–9, 1999.
- [76] J Zenk, W Benzel, W G Hosemann, and H Iro. Experimental research on electrohydraulic lithotripsy of sialolithiasis. *Eur. Arch. Otorhinolalaryngol*, 249:436, 1992.
- [77] P Zhong, I Cioanta, F H Cocks, and G M Preminger. Inertial cavitation and acoustic emission produced during electrohydraulic shock wave lithotripsy. *Journal Acoust. Soc. Am.*, 101:2940–50, 1997.
- [78] P Zhong, X F Xi, S L Zhu, F H Cocks, and G M Preminger. Recent developments in swl physics research. *Journal Endourol.*, 13:(9) 611–7, 1999.